(1/3)

_____ NSC93-2112-M009-036-

_____ 93 08 01 94 07 31

_____ ( )

_____

_____ M. Buttiker, P. Samuelsson, A. G. Malshukov, ,

, , , ,

_____
_____
_____

94 6 3

(1/3)

v

NSC 93　　　2112　　M　　009　　036

　2004　　08　　01　　　2005　　07　　31

M. Buttiker, P. Samuelsson, Mal'shukov,　　,

'　　　'　　　'　　'

(　　　　　　　　　　　) **v**

94　　　6　　　3

: (   )   (   )

Mach-Zehnder   **Hanbury Brown Twiss**
    (   )   (   )   **Rashba-type**
                                        (   )   **sideband**
      (   )   (   )   **Fano**

The quantum transport in mesoscopic structure: [I] Strain induced coupling of spin current to nanomechanical oscillations; [II] Visibility of current and shot noise in electrical Mach-Zehnder and Hanbury Brown Twiss interferometers; [III] Transport characteristics of the dc spin current generation involving a quantum dot; [IV] Effects of impurity on the dc spin current generation in a Rashba-type channel; [V] Dual-frequency modulation and sideband asymmetry characteristics in quantum transport through quantum dot; [VI] The conductance of double quantum point contacts under de-phase process; [VII] The analytic analysis of Fano resonance transport through a mesoscopic two-lead ring.

        :

                                                                                            (   )
                                      (   )   Mach-Zehnder   Hanbury
Brown Twiss   (   )
      (   )   Rashba-type   (   )
                                sideband   (   )
    (   )   Fano

    (   )

                    narrow gap

                                                                                      (   )   ac
                                III-V

            Rashba

                                                                                    ”   ”   ”   ”

      (   )   Mach-Zehnder   Hanbury Brown Twiss
                                                                                              (edge
states)   Aharonov-Bohm flux
                                              Dephasing

Mach-Zehnder   (   )   Hanbury
Brown Twiss

Hanbury Brown Twiss   dephasing
Mach-Zehnder   Mach-Zehnder

dephasing rate

（   ）   Rashba-type
(dc spin current)

（ resonance level ）   （ spin-up)
（ spin-down)   （ resonant
inelastic scattering ）   （ transmission
coefficient ）   （ asymmetry ）   main peak
inter-sideband   main peak
$n\hbar\Omega$ satellite peaks

main peak $(T_{RL}^{\uparrow} - T_{RL}^{\downarrow})$

（   ）   Rashba-type

dip

subband bottom

inter-subband

（   ）
reservoir   ;
sideband

sideband

（   ）

（   ）   Fano

Fano   Fano
Fano
Fano
Fano

Abstract:

We study the spin and charge pumping in mesoscopic structures: [I] Strain induced coupling of spin current to nanomechanical oscillations; [II] Visibility of current and shot noise in electrical Mach-Zehnder and Hanbury Brown Twiss interferometers; [III] Transport characteristics of the dc spin current generation involving a quantum dot; [IV] Effects of impurity on the dc spin current generation in a Rashba-type channel; [V] Dual-frequency modulation and sideband asymmetry characteristics in quantum transport through quantum dot; [VI] The conductance of double quantum point contacts under de-phase process; [VII] The analytic analysis of Fano resonance transport through a mesoscopic two-lead ring.

[I] Strain induced coupling of spin current to nanomechanical oscillations
We propose a setup which allows to couple the electron spin degree of freedom to the mechanical motions of a nanomechanical system not involving any of the ferromagnetic components. The proposed method employs the strain induced spin-orbit interaction of electron in narrow gap semiconductors. We have shown how this method can be used fro detection and manipulation of the spin flow through a suspended rod in a nanomechanical device.

[II] We investigate the visibility of the current and shot-noise correlations of electrical analogs of the optical Mach-Zehnder interferometer and the Hanbury Brown Twiss interferometer. The electrical analogs are discussed in conductors subject to high magnetic fields where electron motion is along edge states. The transport quantities are modulated with the help of an Aharonov-Bohm flux. We discuss the conductance (current) visibility and shot noise visibility as a function of temperature and applied voltage. Dephasing is introduced with the help of fictitious voltage probes. Comparison of these two interferometers is of interest since the Mach-Zehnder interferometer is an amplitude (single-particle) interferometer whereas the Hanbury Brown Twiss interferometer is an intensity (two-particle) interferometer. A direct comparison is only possible for the shot noise of the two interferometers. We find that the visibility of shot noise correlations of the Hanbury Brown Twiss interferometer as function of temperature, voltage or dephasing, is qualitatively similar to the visibility of the first harmonic of the shot noise correlation of the Mach-Zehnder interferometer. In contrast, the second harmonic of the shot noise visibility of the Mach-Zehnder interferometer decreases much more rapidly with increasing temperature, voltage or dephasing rate.

[III] Transport characteristics of the dc spin current generation involving a quantum dot:
We have investigated the mechanism of dc spin current (SC) generation by applying an ac finger-gate (FG) atop a Rashba-type quantum channel. We consider the structure consisting of a quantum dot (QD) located between two ac-FGs and resonance levels exist in the quantum dot formed out of two static-biased gates in such quantum channel. The asymmetric spin-dependent transmission coefficients of the electron is owe to the spin-dependent resonance inelastic

scattering (RIS) process while the electron transport through resonance levels of a quantum dot. The transmission coefficient of the spin-up electron is smaller than the spin-down one while the incident energy is around the resonant main peak. There are satellite peaks occurring around $n\hbar\Omega$ away from the resonant main peaks due to the modulation of the ac-FGs. Here, the transmission coefficient of the spin-up electron is larger than the spin-down one for the spin-resolved satellite peaks. The time-dependent, spin-resolved mechanism makes the difference $(T_{RL}^{\uparrow} - T_{RL}^{\downarrow})$ change its sign such that the polarized direction of the dc spin current (SC) would be changed its sign due to the incident energy crossing the center of the resonant main peaks in our system.

[IV] Effects of impurity on the dc spin current generation in a Rashba-type channel:

We have investigated the effects of a single impurity on the dc spin current (SC) generation in a Rashba-type channel. The dc SC could be generated via a single ac finger-gate (FG). Effects of impurity have strong dependence of transverse-location and strength for the transport of dc SC in the channel. The spin-resolved dip structures are broadened while the impurity is away from the edge inside of the ac-FG. The effect of impurity is decreased for the impurity in the edge of the channel. The impurity has small effect for the transport while the impurity is outside of the ac-FG. The spin-resolved inter-subband transition is observed while the incident energy near each subband threshold because the symmetry of transverse direction is broken by the impurity.

[V] Dual-frequency modulation and sideband asymmetry characteristics in quantum transport through quantum dot:

We study quantum transport of electrons through a quantum dot under dual-frequency modulation. Under such modulation condition, the spatial-invariance is destroyed by the two potentials of different oscillating frequencies. Hence, a net current will be formed by each time cycle. In addition, we discover that electrons exhibit remarkable asymmetric side-peak structures. In some conditions, electrons are more probable to make transition through resonance state by absorbing a photon than emitting a photon. This characteristic will reverse when the resonance state approaches subband bottom.

[VI] The conductance of double quantum point contacts under de-phase process

In many researches, the scale of system is much smaller then coherent length. So it neglect the de-phase process due to electron scattering. We use custom method to induce numerical de-phase process in 1-D case to solve 2-D problem through considering sub-band mixing. Observe de-coherent strength how to influence the conductance of double quantum point contacts (QPCs) in series.

[VII] Fano resonance transport through a mesoscopic two-lead ring

The low-energy and ballistic transport through a 1-dimensional two-lead ring at zero magnetic field is studied. Our study have focused on the case of the potential in the ring defines open but not closed cavities, and it is found that Fano resonance may appear at energies correspond to the standing wave states in the ring, but commensurate system parameters can shrink the widths of

the resonance at some energies to infinitesimally small. These findings suggest that the conventional picture of the Fano resonance as an effect due to the interference between the paths through resonant states and non-resonant continuum of states might not account for all the Fano-type lines seen in the transport measurements. We analytically obtain the approximation form to interpret the Fano Resonance peak structures. Moreover, the resonance may find application in the fabrication of electrical nano-devices since it is sensitive to the system parameters and hence tunable.

Motivations and goals

[I] Strain induced coupling of spin current to nanomechanical oscillations

an ability to control the spin transport in semiconductors is a key problem to be solved towards implementation of semiconductor spintronics into quantum information processing [1-3]. Many methods have been proposed to achieve control of the electron spin degree of freedom using magnetic materials, external magnetic fields and optical excitation [3]. Other promising ideas involve the intrinsic spin-orbit interaction (SOI) in narrow gap semiconductors to manipulate the spin by means of electron fields [4] and electric gates [5, 6]. Recently, some of these ideas have been experimentally confirmed [7,8].

In semiconductors the spin-orbit effect appears as an interaction of the electron spin with an effective magnetic field whose direction and magnitude depend on the electron momentum. A specific form of this dependence is determined by the crystal symmetry, as well as by the symmetry of the potential energy profile in heterostructures. In strained semiconductors new components of the effective magnetic field appear due to violation of the local crystal symmetry [9]. The effective of the strain induced SOI on spin transport was spectacularly demonstrated by Kato *et. al.* in their Faraday experiment [8]. An interesting property of the strain induced SOI is that the strain can be associated with mechanical motion of the solid, in particular, with oscillations in nanomechanical systems (NMS), in such a way making possible the spin-orbit coupling of the electron spin to nanomechanical oscillations. At the same time a big progress in fabricating various NMS [10] allows one to reach the required parameter range to observe subtle effects produced by such a coupling.

We will consider NMS in the form of a suspended beam with a doped semiconductor film epitaxially grown on its surface (see Fig. 1). An analysis of the SOI in this system shows that the flexural and torsion vibrational modes couple most effectively to the electron spin. As a simple example, we will focus the torsion modes. The strain associated with torsion produces the spin-orbit field which is linear with respect to the electron momentum and is directed perpendicular to it. This field varies in time and space according to respective variations of the torsion strain. Due to the linear dependence on the momentum, the SOI looks precisely as interaction with spin dependent electromagnetic vector potential. An immediate result of this analogy is that the time dependent torsion gives rise to a motive force on electrons. Such a force, however, acts in different directions on particles with oppositely oriented spins, including thus the spin current in the electron gas. The physics of this phenomenon is very similar to the spin current generation under time dependent Rashba SOI, where the time dependence of the SOI coupling parameter is provided by the gate voltage variation [6]. In the present work we will focus, however, on the inverse effect. Due to the SOI coupling, the spin current flowing through the beam is expected to create a mechanical torsion. The torque effect on NMS due to spin flow

has been previously predicted [11] for a different physical realization, where the torque has been created by spin flips at nonmagnetic-ferromagnetic interface. They also suggested an experimental set up to measure such a small torque. The torque due to SOI effect can be by 2 orders of magnitude stronger than the torque produced by the current flowing through the FM-NM interface. Hence, the SOI effect can be measured by the same method as was proposed [11]. Besides this method, other sensitive techniques for displacement measurements can be employed [12].
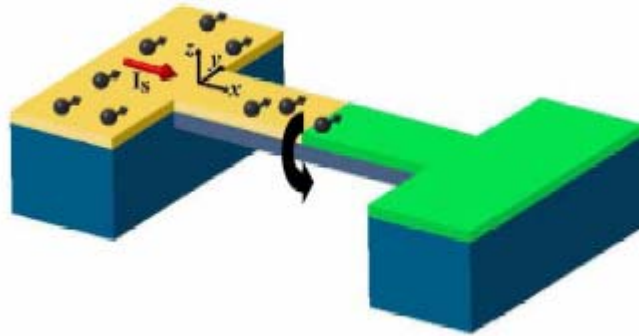

Fig. 1 : Schematic illustration of electromechanical spin current detector, containing a suspended semiconductor-mental (S-M) rectangular rod atop an insulating substrate (blue). A spin current is injected from the left semiconductor reservoir (yellow) and then diffuses toward the metallic film (green). While passing through the semiconductor film, the spin current induces torque shown by the black arrow.

[II] Visibility of current and shot noise in electrical Mach-Zehnder and Hanbury Brown Twiss interferometers:

With the advent of mesoscopic physics, it has become possible to experimentally investigate quantum phase coherent properties of electrons in solid state conductors in a controlled way. In particular, in ballistic mesoscopic samples at low temperatures, electrons can propagate up to several microns without loosing phase information. This opens up the possibility to investigate electrical analogs of various optical phenomena and experiments. An investigation of such analogs is of fundamental interest. On the one hand, it allows one to establish similarities between the properties of photons and conduction electrons, a consequence of the wave nature of the quantum particles. On the other hand, it also allows one to investigate the differences between the two types of particles arising from the different quantum statistical properties of fermions and bosons. For many-particle properties, such as light intensity correlations or correspondingly electrical current correlations, noise, the quantum statistical properties are important. [1,2] Both the wave-nature of the particles as well as their quantum statistics are displayed in a clearcut fashion in interferometer structures. In this work we are concerned with the electrical analogs of two well known optical interferometers, the single-particle Mach-Zehnder (MZ) interferometer and the two-particle Hanbury Brown Twiss (HBT) interferometer.

The MZ-interferometer is a subject of most textbooks in optics.[3] In the framework of quantum optics, considering individual photons rather than classical beams of light, the interference arises due to the superposition of the amplitudes for two different possible paths of a single photon. This leads to an interference term in the light intensity. The MZ-interferometer is

thus a prime example of a single particle interferometer.[4] Various electronic interferometers with ballistic transport of the electrons have been investigated experimentally over the last decades, as e.g. Aharonov-Bohm (AB) rings[5] and double-slit interferometers.[6] Detailed investigations of dephasing in ballistic interferometers was carried out in Refs. [7,8]. Only very recently was the first electronic MZ-interferometer realized by Ji et al.[9] in a mesoscopic conductor in the quantum Hall regime. A high visibility of the conductance oscillations was observed, however the visibility was not perfect. This led the authors to investigate in detail various sources for dephasing. As a part of this investigation, also shot noise was measured. Still, some aspects of the experiment are not yet fully understood. Theoretically, Seelig and one of the authors [10] investigated the effect of dephasing due to Nyquist noise on the conductance in a MZ-interferometer. The effect of dephasing on the closely related four-terminal resistance in ballistic interferometers [11] was investigated as well. Dephasing in ballistic strongly interacting systems is discussed by Le Hur. [12,13] Following the experimental work of Ji et al.,[9] Marquardt and Bruder investigated the effect of dephasing on the shot-noise in MZ-interferometers, considering dephasing models based on both classical [14,15] as well as quantum fluctuating fields.[16] Very recently, Forster, Pilgram and one of the authors [17] extended the dephasing model of Refs. [10,14] to the full statistical distribution of the transmitted charge.

The HBT-interferometer [18-20] was originally invented for stellar astronomy, to measure the angular diameter of stars. It is an intensity, or two-particle,[4] interferometer. The interference arises from the superposition of the amplitudes for two different two-particle processes. Importantly, there is no single particle interference in the HBT-interferometer. Consequently, in contrast to the MZ-interferometer there is no interference in the light intensity, the interference instead appears in the intensity-intensity correlations. Moreover, the intensity-intensity correlation also display the effect of quantum statistics. Photons originating from thermal sources tend to bunch, giving rise to positive intensity cross correlations. For the electronic analog of the HBT-interferometer, it was the corresponding anti-bunching of electrons that originally attracted interest. It was predicted [1] that the electrical current cross correlations in mesoscopic conductors would be manifestly negative, i.e. display anti-bunching, as a consequence of the fermionic statistics of the electrons. Negative current cross correlations were subsequently observed in two independent experiments.[21,22] Recently, anti-bunching for field emitted electrons in vacuum was also demonstrated.[23] The two-particle interference in the HBT-experiment has received much less attention. We emphasize that while the bunching of the photons was necessary for obtaining a finite, positive cross correlation signal, it was the two-particle effect that was of main importance to HBT since the angular diameter of the star was determined from the two-particle interference pattern. In electrical conductors, two-particle effects in AB-interferometers were investigated theoretically in Refs. [24-26]. Only very recently two of the authors and Sukhorukov [27] proposed a direct electronic analog of the optical HBT-interferometer which permits to demonstrate two-particle interference in an unambiguous way.

In this work we investigate and compare in detail the current and and zero-frequency noise in electronic MZ and HBT interferometers. We consider interferometers implemented in mesoscopic conductors in the integer Quantum Hall regime, where the transport takes place along

single edge states and Quantum Point Contacts (QPC's) serve as controllable beam splitters. The effect of finite temperature, applied bias and asymmetry, i.e. unequal length of the interferometer arms, is investigated. The strength of the interference contribution is quantified via the visibility of the phase oscillations. The dependence of the visibility on the beam splitter transparencies as well as on the temperature, voltage and asymmetry is discussed in detail. Of interest is the comparison of visibility of the shot-noise correlation of the MZ-interferometer and the HBT-intensity interferometer. Shot noise correlations in the MZ-interferometer exhibit two contributions, one with the fundamental period of h/e and a second harmonic with period h/2e. The shot noise correlations in the HBT-interferometer, even though they are due to two particle processes, are periodic with period h/e. Thus the Aharonov-Bohm period can not be used to identify the two particle processes which give rise to the HBT effect. It is therefore interesting to ask whether the HBT two-particle processes have any other signature, for instance in the temperature or voltage dependence of the visibility of the shot-noise correlation. We find that this is not the case. To the contrary, we find that the shot noise correlations in the HBT intensity interferometer behave qualitatively similar to the h/e shot noise correlation in the MZ-interferometer. In contrast the h/2e contribution in the shot noise of the MZ-interferometer decreases more rapidly with increasing temperature, voltage or dephasing rate than the h/e oscillation in the MZ- or HBT-interferometer.

We investigate dephasing of the electrons propagating along the edge states by connecting one of the interferometer arms to a fictitious, dephasing voltage probe. In all cases, the current and noise of the MZ-interferometer as well as the noise in the HBT-interferometer, the effect of the voltage probe is equivalent to the effect of a slowly fluctuating phase.

[III] Transport characteristics of the dc spin current generation involving a quantum dot:

Spintronics is important in both application and fundamental arenas [1,2,40]. The key issue of great interest is the generation of dc spin current (SC) without charge current. We proposed the SC generation via only one single ac-FG in a Rashba-type narrow channel [41]. A lot of methods have been proposed to generate and manipulate SC by utilizing optical excitation [42] , spin injection [43], and external magnetic field [44] in the QD system. More recently, another alternative method for generation and control of the SC is based on the Rashba-type spin-orbit interaction (SOI) in the narrow gap semiconductors [45].

The transport characteristics of metal-QD-metal structure have also been studied [46]. Utilizing the time-variation field to generate the SC has been studied in some mesoscopic systems in adiabatic [47] and non-adiabatic regimes [41,48]. Here, we consider a mesoscopic structure consisting of FG-QD-FG, where the FG is ac biased and QD is modeled by two delta potential in the quantum channel. The spin-dependent RIS mechanism makes the spin-dependent electron transit to its subband bottom such that the asymmetry spin-resolved transmission coefficients occur [41]. The spin-dependent RIS plays a crucial role while the incident energy is close to the resonance level or away $n\hbar\Omega$ from resonance level in the QD. We find that the difference of spin-resolved transmission coefficients would be changed the sign depended on the incident energy. The spin-down transmission coefficient is larger than spin-up one $T_{RL}^{\downarrow} > T_{RL}^{\uparrow}$ for incident energy close to the resonance main peak. However, the spin-up transmission becomes larger than

spin-down one $T_{RL}^{\uparrow} > T_{RL}^{\downarrow}$ for the incident energy close to the satellite peaks with respect to the resonance level.

Eventually, we obtain the dc SC without any charge current and opposite polarized direction for SC via varying the electron incident energy. Experimentally, we can tune the strength of two delta potentials to shift the energy of resonance main peak in order to change the switching point of the polarized direction of a SC. This tunable polarized direction of the SC is more valuable in the application of the spintronics device.

[IV] Effects of impurity on the dc spin current generation in a Rashba-type channel

We have proposed the dc SC generation via a ac-FG in Rashba-type quantum channel [41]. We are also interested in effects of the impurity for the transport of dc SC. The location and strength dependence of the impurity for the transport of dc SC has been studied. We find the effect of the impurity would be enhanced while the impurity is away from the channel-edge inside the ac-FG. The intersubband transition occurring near the subband bottom due to the translation invariance being broken. The impurity has smaller effect for the transport while the impurity is outside the ac-FG.

[V] Dual-frequency modulation and sideband asymmetry characteristics in quantum transport through quantum dot:

Quantum pumping effect has been an interesting topic [49-51]. In this work, we try to achieve quantum charge pumping in an alternative way by dual-frequency modulation instead of introducing a phase difference into the time-dependent potentials. Our goal is to find the optimal pumping modulation of the dual-frequency system, and also to get to understand the reasons electrons exhibit asymmetric sideband transmission characteristics.

[VI] The conductance of double quantum point contacts under de-phase process:

In experimental results, the phenomenon of double QPCs (quantum point contact) in series cannot be explained very well in classical theory. Because the conductance of one QPC will be quantized, however, in classical theoretical treatment, the total conductance of double QPCs in series still can observe the plateaus in curve. Here, we simply utilize an imaginary reservoir between the double QPCs to simulate the de-coherent effect related to the electron scattering process. This method can introduce a concept for the coherent length. We also can compare the de-well time and the lifetime via this method.

[VII] The analytic analysis of Fano resonance transport through a mesoscopic two-lead ring:

The conventional Fano resonance is an effect due to the interference between resonant and non-resonant processes. It was first proposed in atomic physics [52], and the effect was then observed in a wide variety of spectroscopy such as the atomic photoionization [53], optical absorption [54], Raman scattering [55], and neutron scattering [56]. As recent progress in the technology of fabrication of electrical nano-devices has achieved devices with the size of the order of the inelastic length scales of the conduction electrons, where within the electronic

transcript is ballistic, the Fano resonance is also seen in condensed matter systems. For instance, it is seen in the Scanning Tunneling Spectroscopy of a surface impurity atom [57,58], transport through a quantum dot (QD) [59-64] or carbon nanotube [65]. Moreover, it is proposed that the resonance can be used in the probe of phase coherence [66,67] and design of spin filters [68].

Results and discussion:

[I] Strain induced coupling of spin current to nanomechanical oscillations [70] (Appendix A).

[II] Visibility of current and shot noise in electrical Mach-Zehnder and Hanbury Brown Twiss interferometers (Appendix B).

[III] Transport characteristics of the dc spin current generation involving a quantum dot:

The system structure is shown in Fig. 1 and the QD is located between two ac-FGs. We use the scattering matrix method to deal with such problem. For simplicity, we suppose the symmetric structure such that the dc SC would be generated by ac-FG [1] without accompanying any charge current.
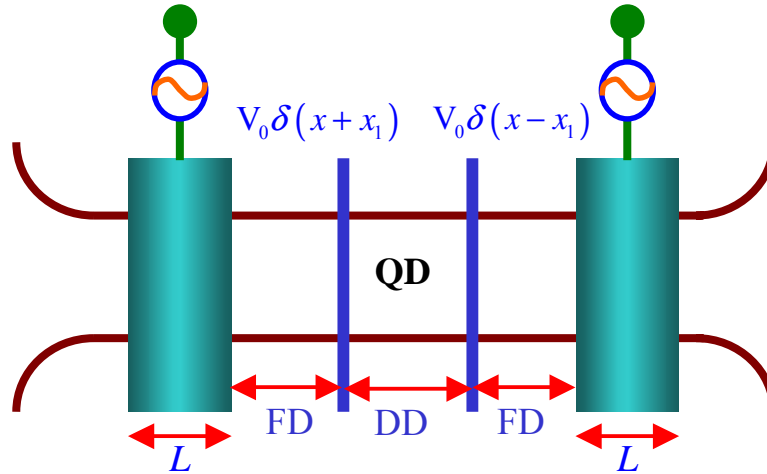
Fig. 1: Schematic illustration of dc spin current generation involving a quantum dot on the Rashba-type quantum channel.

Figure 2 presents the spin-resolved transmission coefficients T_{RL}^{σ} versus incident energy in the unit of μ/Ω for various amplitudes α_1 of the dynamic spin-orbit coupling constant. The notation T_{RL}^{σ} denotes that electron is incident from left-hand side terminal into the right-hand side terminal with spin state σ. We observe the spin-resolved transmission coefficient $T_{RL}^{\uparrow} < T_{RL}^{\downarrow}$ for the incident energy around the resonance main peaks $E_1 = 4.93\,\Omega$ and $E_2 = 20.13\,\Omega$. The other features are $T_{RL}^{\uparrow} > T_{RL}^{\downarrow}$ for satellite peaks which are away from each resonance main peak in $n\,\hbar\Omega$. As increasing α_1, the strength of inter-sideband transition become stronger such that the difference of the spin-resolved transmission coefficients is enhanced due to the RIS through the resonance levels in the QD.

Figure 3 shows the SC corresponding to the figure 2 and the charge current is zero for our symmetric structure. The most interesting phenomena is that polarized direction of the SC have opposite sign while the incident energy of an electron passes the two resonance main peaks. It is because the difference of the spin-resolved transmission coefficients has the opposite-sign value for the resonance main peaks and satellite peaks, respectively.
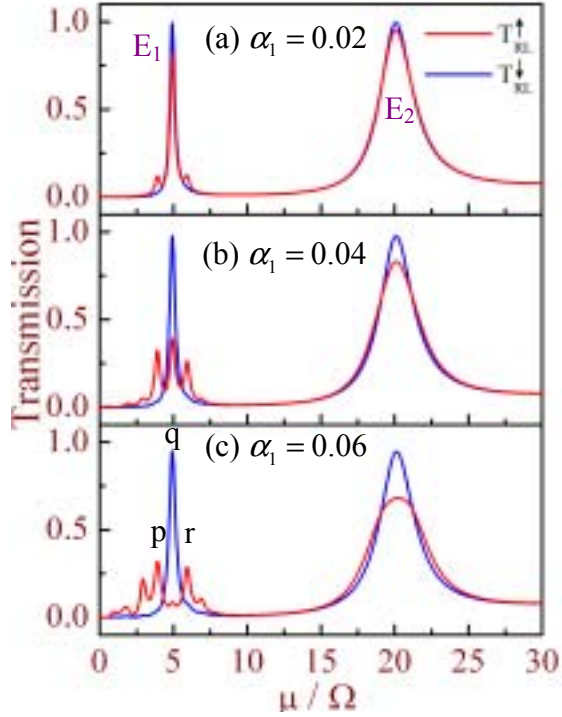

Fig. 2: The spin-resolved transmission coefficient is plotted as a function of incident energy μ/Ω for (a) $\alpha_1 = 0.02$, (b) $\alpha_1 = 0.04$, and (c) $\alpha_1 = 0.06$. Other parameters are spin-orbit coupling constant α_0 =0.13, external frequency Ω =0.001 (14GHz), delta-type gate strength V_0=0.4, the ac-FG length L=35 (140nm), FD=20 (80nm), and DD=40 (160nm). There are several spin-resolved satellite peaks occurring away from the first resonance main peak. The two resonance main peaks are related to the energy E_1=4.93Ω and E_1=20.13Ω, respectively.
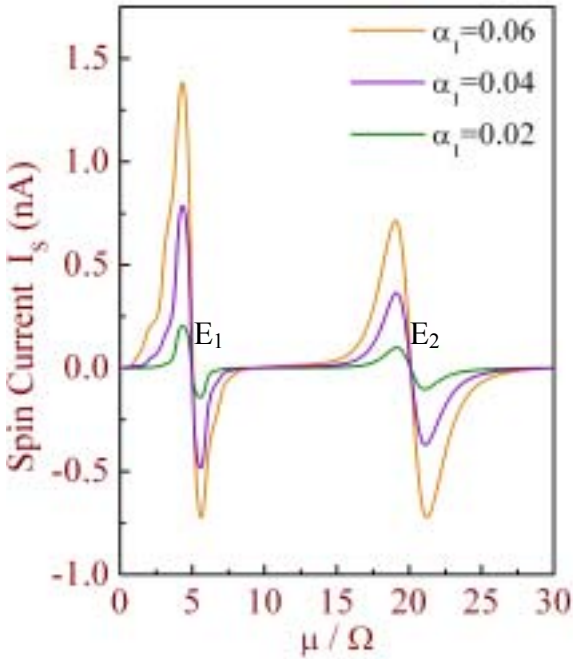

Fig 3: The spin current related to the Fig. 2 is plotted for $\alpha_1 = 0.02$ (green), 0.04 (purple), and 0.06 (brown). The polarized direction of the SC is changed the sign while the incident energy of an electron passes the resonance main peaks E_1 and E_2.

We also find that the absolute value of the SC magnitude is larger in left-hand side of E_1 (the first resonance main peak) than that in the right-hand side of E_1. It is because the larger difference of

spin-resolved transmission coefficients in the left-hand side of E_1 due to the asymmetric satellite peaks. The absolute value of the SC magnitude is almost equal for the left-hand side and right-hand side of E_1 because of the unobvious asymmetric satellite-peak structures. The tunable polarized direction of the SC is valuable to apply in the SC selector device based on time-modulated FG in the semiconductor device.
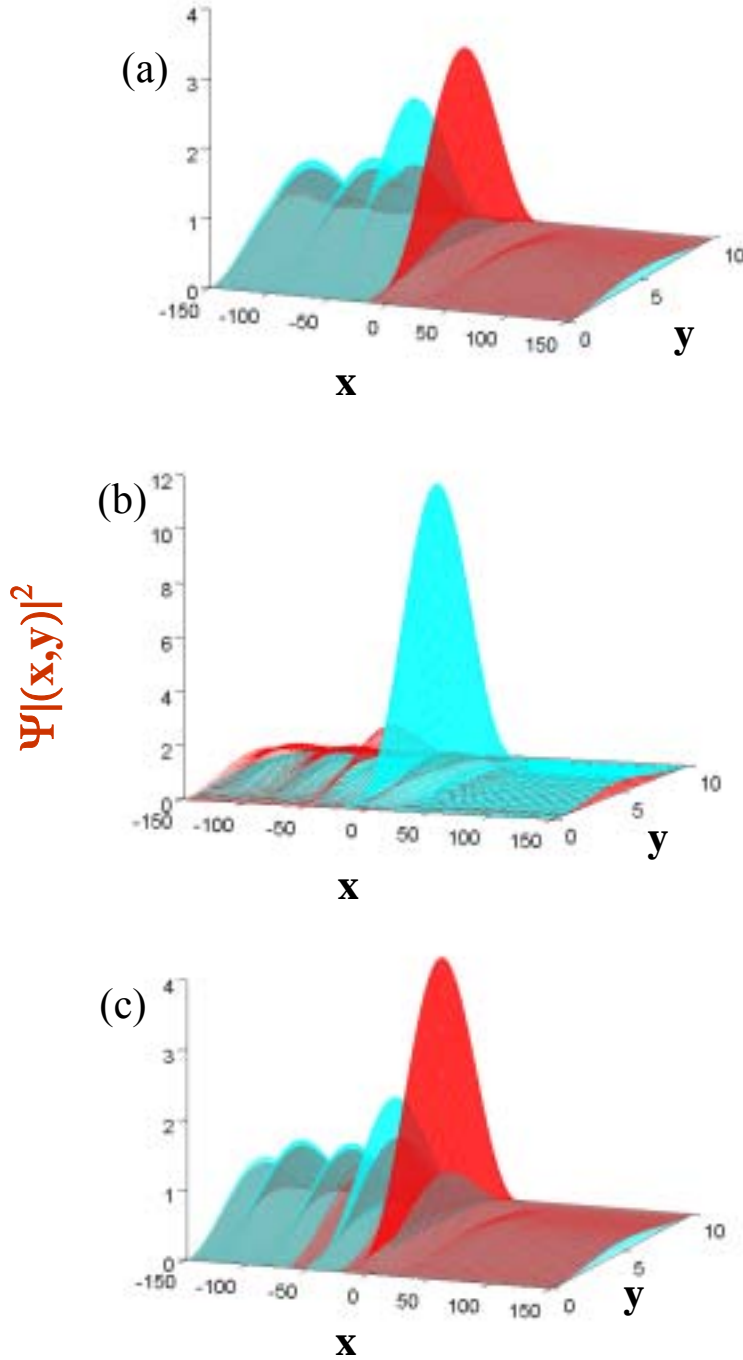

Fig. 4: The magnitude square of the spin-up (red) and spin-down (blue) wave functions are plotted as a function of spatial coordinate in the Rashba-type quantum channel. We choose the incident energy for three points (a) p, (b) q, and (c) r (see the Fig. 2(c)). The QD is located between x=-20 and x=20; the first ac-FG is located between x= -75 and x= -40; the second ac-FG is located between x=40 and x=75. The transverse direction is y direction.

We can observe that the magnitude square for spin-up wave function is smaller than spin-down wave function in Fig. 4 (b) in the transmission region (x>75) at the resonance main peak q corresponding to the relation $T_{RL}^{\uparrow} < T_{RL}^{\downarrow}$. For the satellite peaks p and r, the situation is reversed,

$T_{RL}^{\uparrow} > T_{RL}^{\downarrow}$, in the transmission region. The spin-dependent wave functions are localized within the QD for the resonance main peak and satellite peaks in standing-wave profile due to the resonance inelastic tunneling effect.

We use one-sideband approximation expressions of a single ac-FG to analyze the numerical results. The spin-resolved one-sideband transmission coefficients are expressed in the form of

$$\begin{cases} T_1^{\sigma} = \dfrac{\left(1-\cos\left((\sqrt{\mu}-\sqrt{\mu+\Omega})L\right)\right)}{2\sqrt{\mu(\mu+\Omega)}} \left| \left(\dfrac{\alpha_1}{2\Omega}k_{RL}^{\sigma}(\mu)\left[-\sqrt{\mu+\Omega}-\sqrt{\mu}\right]+\dfrac{\alpha_1}{4}\right) \right|^2 \\ \\ T_{-1}^{\sigma} = \dfrac{\left(1-\cos\left((\sqrt{\mu}-\sqrt{\mu-\Omega})L\right)\right)}{2\sqrt{\mu(\mu-\Omega)}} \left| \left(\dfrac{\alpha_1}{2\Omega}k_{RL}^{\sigma}(\mu)\left[-\sqrt{\mu-\Omega}-\sqrt{\mu}\right]+\dfrac{\alpha_1}{4}\right) \right|^2 \end{cases} \quad \text{.........(1).}$$

All the spin-dependent difference comes from the spin-resolved wave vector k_{RL}^{σ}. Figure 5 presents the one-sideband approximation for the analytical and numerical results. Figure 5 (b) and (c) reveal that the partial transmission coefficient $T_{\pm1}$ is larger for the spin-up electron than the spin-down one due to the RIS process. It shows that the one sideband-transition mechanism plays an important role for the difference of the spin-resolved transmission coefficients. While the incident energy is close to the resonance main peak, the spin-up electron is more easily to transit to the satellite peaks via absorbing or emitting $\hbar\Omega$ photon energy. For the energy around satellite peaks, the transmission rate is barely low due to far from the resonance level in the QD.

It turns out the spin-up electron has lower transmission coefficient ($T_{RL}^{\uparrow} < T_{RL}^{\downarrow}$) due to the larger probability to transit to the satellite peaks for the spin-up electron. In the other hand, the incident energy of the electron coincides with the nearest satellite peaks away from the main peak such that the spin-up electron has larger probability to transit to the resonance main peak passing through the QD and we get the opposite result of $T_{RL}^{\uparrow} > T_{RL}^{\downarrow}$.

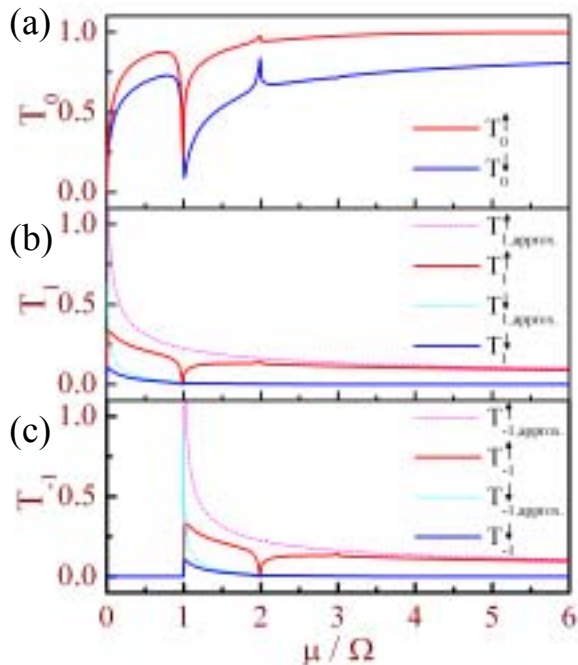Fig. 5: The spin-resolved partial transmission coefficients T_0 and $T_{\pm1}$ are plotted as a function of μ/Ω for a single ac-FG case. Other parameters are $\alpha_0 = 0.13$, $\alpha_1 = 0.02$, $\Omega = 0.001$, and the ac FG length L=35. The dip structures are organized the quasi-bound state features due to an electron emitting $n\hbar\Omega$ photon energy to transit to beneath of its subband bottom.
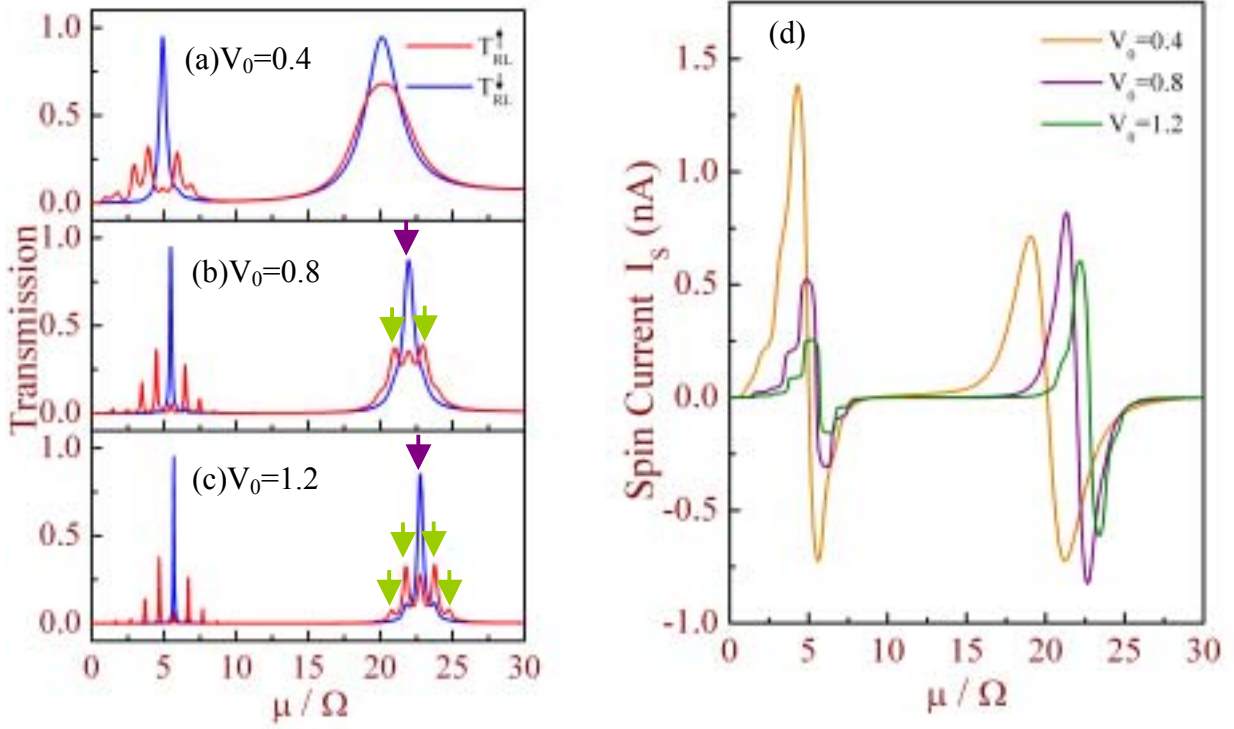
Fig. 6: The spin-resolved transmission coefficients are plotted as a function of μ/Ω with varying the delta potential strength V_0= (a) 0.4, (b) 0.8, and (c) 1.2. The SC is shown in (d) corresponding to the Fig. 6 (a)-(c). Other parameters are the same in the Fig. 2.

Next, we increase the strength V_0 of the two delta potentials and the resonance levels are lift to the higher energy. When the magnitude of V_0 is enhanced, the band width of each resonance level become more and more narrow in the QD. If we focus on the second resonance peak (purple arrow), the satellite peaks (green arrows) would be resolved by increasing the strength of V_0 in Fig. 6 (a)-(c). The Fig. 6 (d) shows the resonance main peaks is shifted toward the higher energy owe to the larger V_0. The SC becomes smaller near the first main peak because the band width for the main and satellite peaks is more narrow as increasing V_0. We can tune the energy for the switching points such that the spin-polarized direction of the SC would be changed its sign as its incident energy crossing switching points via varying V_0.

In summary, we have investigated the dc SC generation in sequent structure of ac-FG, QD, and ac-FG. The difference of the spin-resolved transmission coefficients is shown the opposite sign while the incident energy occurring around the main peaks $T_{RL}^{\uparrow} < T_{RL}^{\downarrow}$ and satellite peaks $T_{RL}^{\uparrow} > T_{RL}^{\downarrow}$, respectively. The switching point for the spin-polarized direction of SC can be tuned by varying V_0. We have proposed a possible setup to realize the device for SC selector based on

RIS mechanism involving a QD.

[IV] Effects of impurity on the dc spin current generation on a Rashba-type channel:

The finite-range impurity in the Rashba-type quantum channel is in the from $V_0 \delta(x - x_0)[\theta(y - y_1) - \theta(y - y_2)]$. The system configuration is show in Fig. 1 and the transverse direction is finite-range potential with longitudinal delta profile potential.
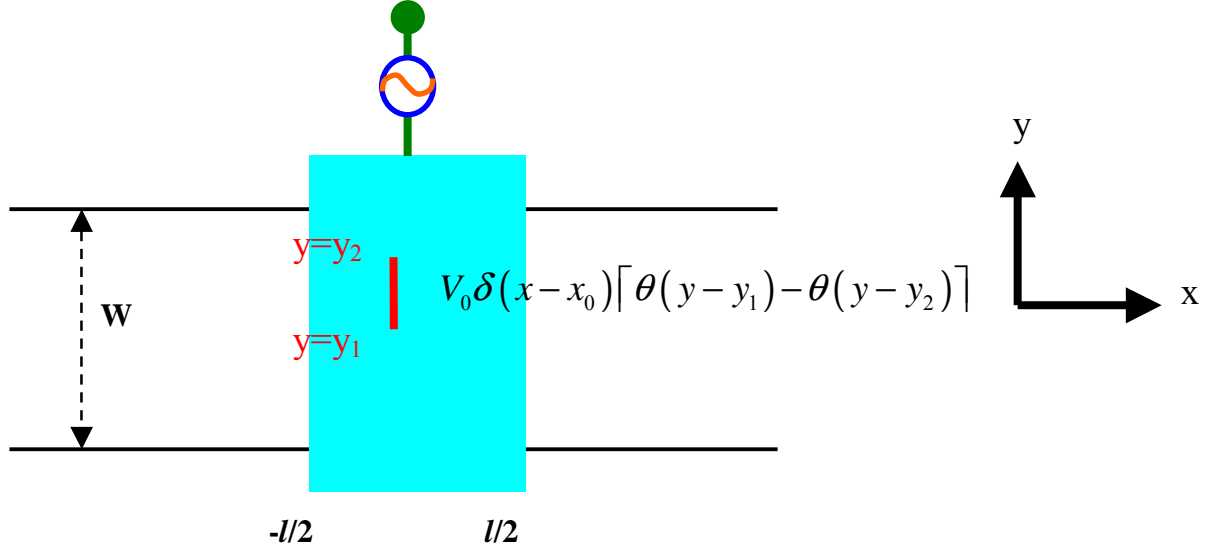

Fig. 1: The system configuration is shown and the finite-range impurity (red) can be located inside or outside of the ac-FG. The blue block is ac-FG, V_0 is the impurity strength, l is the FG length and W is the channel width.

The dc SC can be generated via a single ac-FG without any charge current [41]. The resonance inelastic scattering (RIS) play a important role to make the spin-resolved transmission coefficient asymmetry. The Fig. 2 presents the spin-resolved transmission coefficients and SC versus incident energy μ_n / Ω for no impurity case.
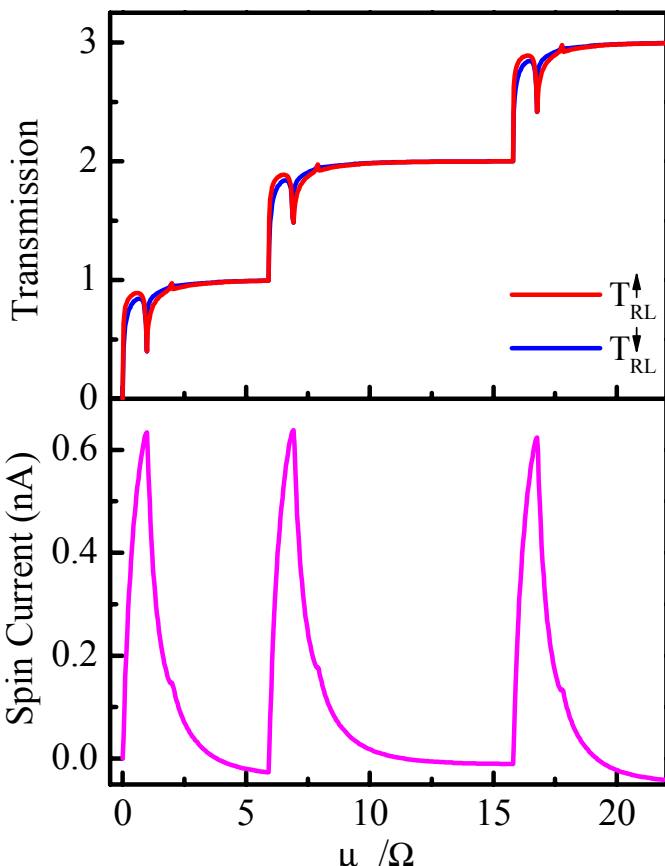

Fig. 2: The spin-resolved transmission coefficients and spin current versus μ_n / Ω is plotted for no impurity case. Other parameters are: static SOI coupling constant $\alpha_0 = 0.13$, the dynamic SOI amplitude $\alpha_1 = 0.05$, oscillating frequency $\Omega = 0.002$ (28GHz), channel width W=50, and the ac-FG length l=20. The spin-resolved dip structures is due to the RIS mechanism.

While the impurity is located in the channel edge inside of the ac-FG, the effect of the impurity is small for the transport of dc SC. Figure 3 presents the transmission and dc SC versus incident energy μ_n/Ω as increasing the impurity strength V_0. All of their SC are almost the same and it shows the weak effect of impurity for the transport of dc SC.
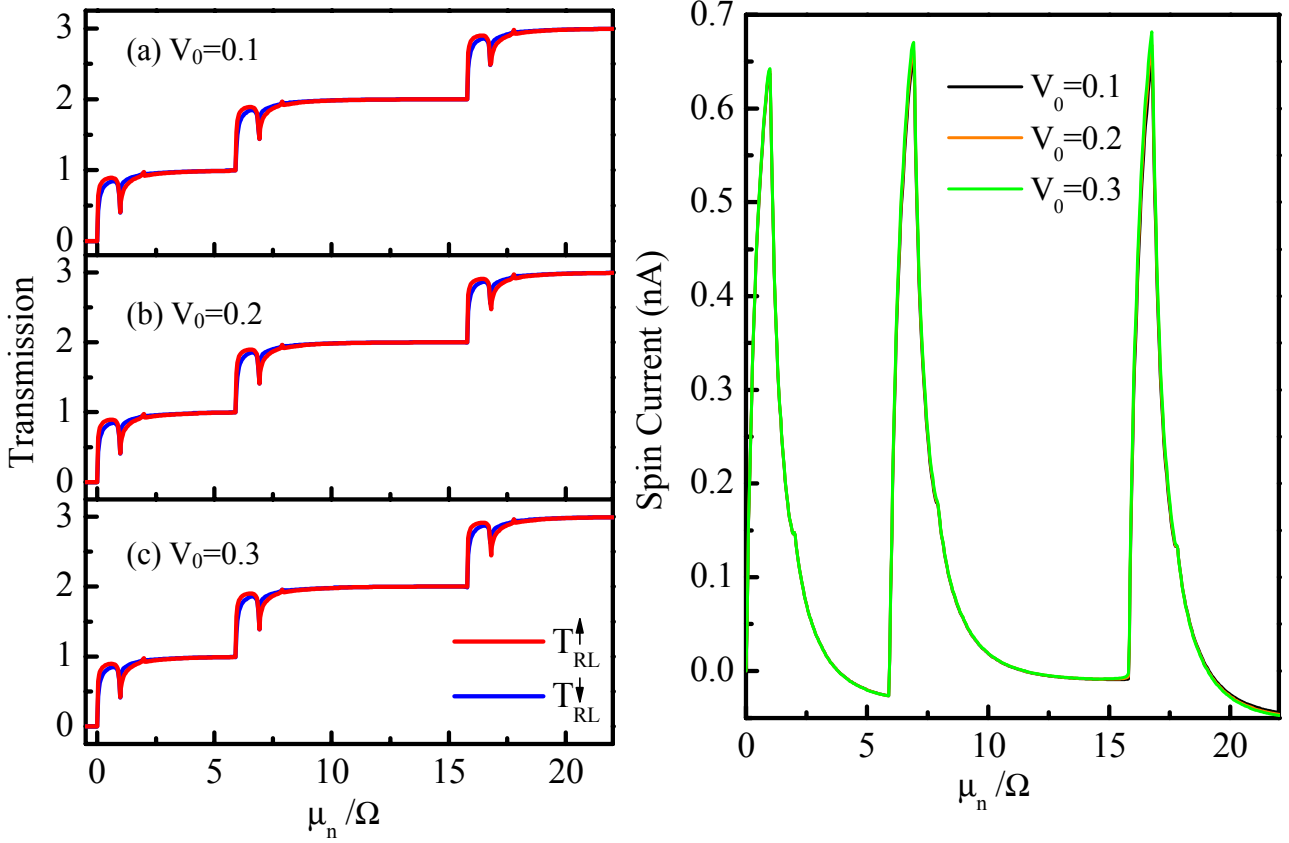

Fig.3: The spin-resolved transmission coefficients and SC is plotted as function of μ_n/Ω for varying the impurity strength V_0. The impurity is located in the channel edge for $x_0=0$, $y_1=0$, and $y_2=4$. Other parameters are the same as Fig.2.

While the impurity is away from the channel edge, the effect of the impurity is more obvious in Fig. 4. We also observe the structure of the intersubband transition near the arising of the second and third subband bottom due to breaking the translation invariance in transverse direction. As increasing the impurity strengths, the spin-resolved dip structures become more broaden due to the impurity scattering.

While the impurity is away from the channel edge outside of the ac-FG, the effect of impurity is smaller than inside of the ac-FG. The spin-resolved transmission coefficients and SC is shown in Fig. 5. The spin-resolved dip structures are not obvious broaden in this case providing the effect of the impurity is weaker outside of the ac-FG than inside of the ac-FG.

In summary, effects of impurity on transport of dc SC depend on the locations and strength of the impurity. The impurity affects the dc SC is not very strong such that the dc SC generation via a single FG is valuable in application of spintronics devices even in diluted-impurity case.
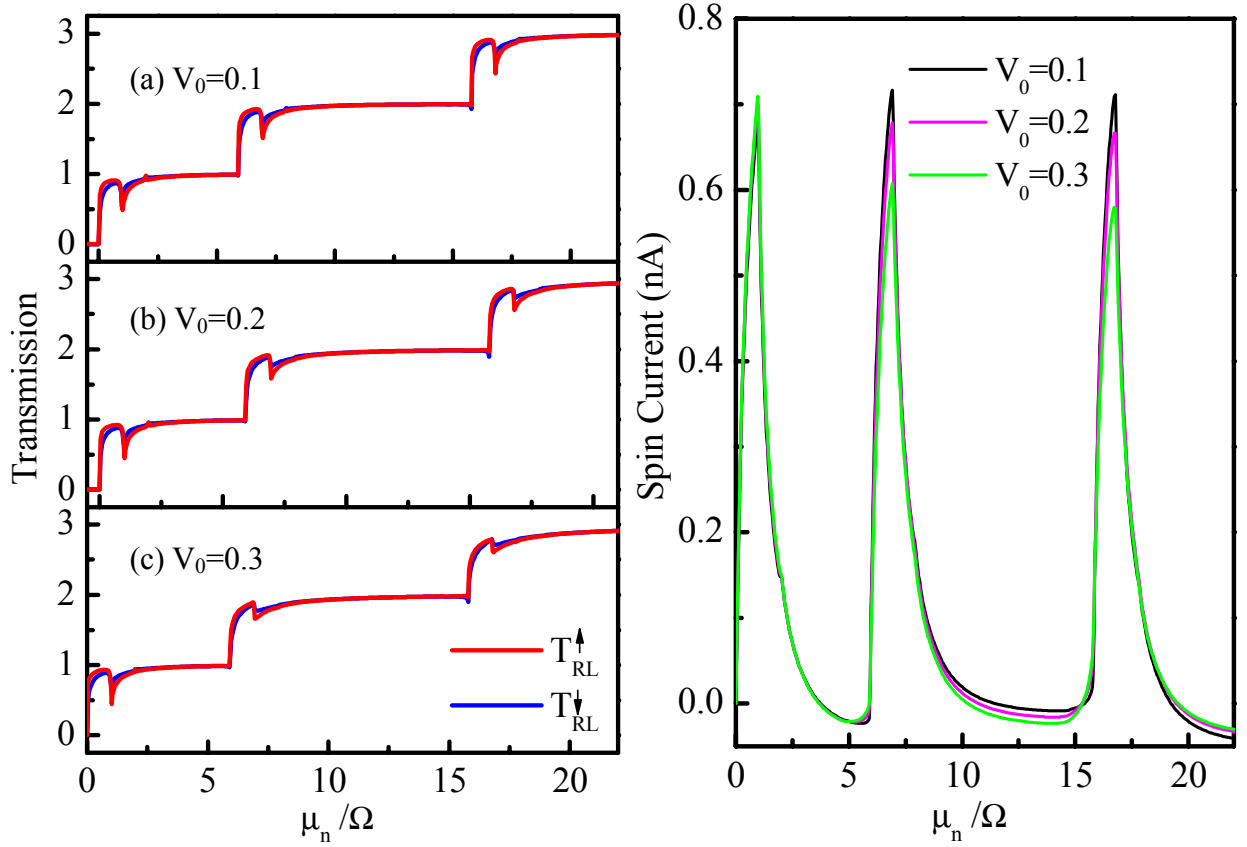
Fig.4: The spin-resolved transmission coefficients and SC is plotted as function of μ_n / Ω for varying the impurity strength V_0. The impurity is located in the channel edge for $x_0=0$, $y_1=8$, and $y_2=12$. Other parameters are the same as Fig.2.
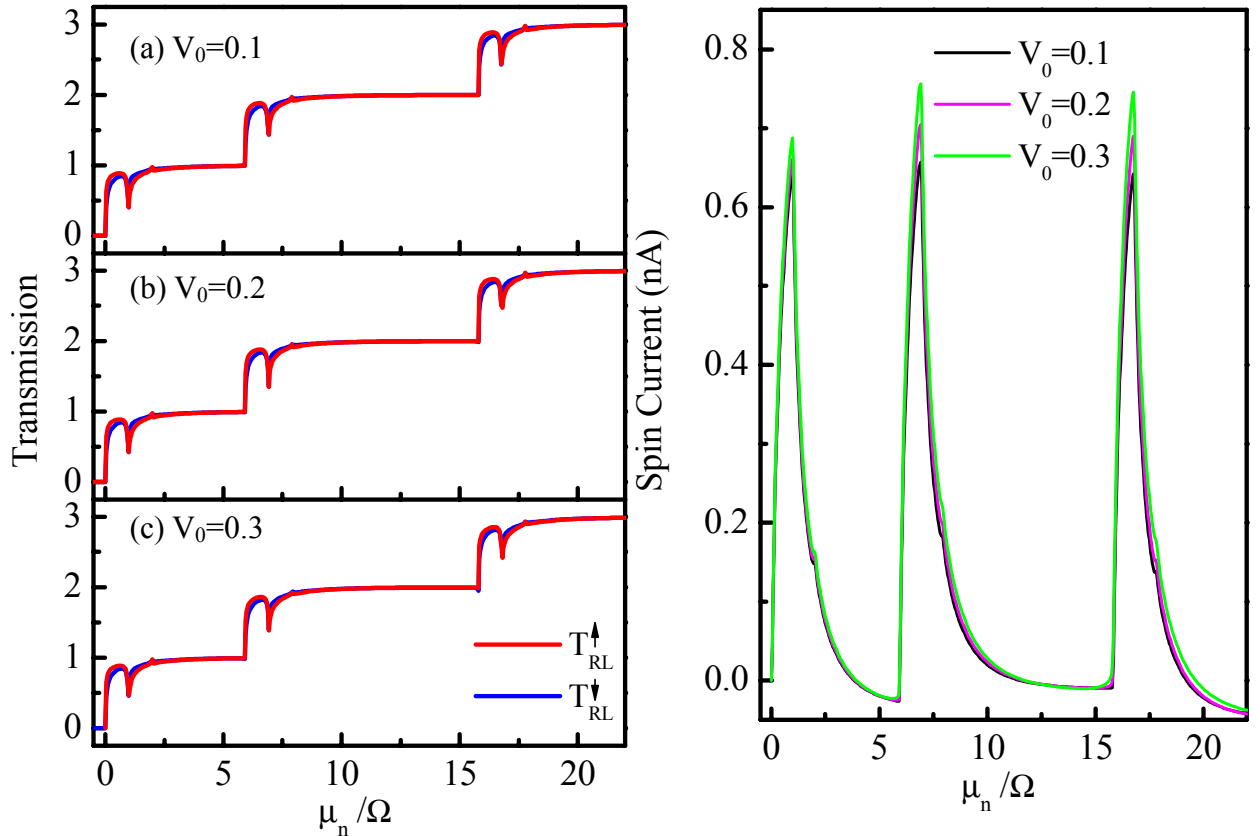

Fig.5: The spin-resolved transmission coefficients and SC is plotted as function of μ_n / Ω for varying the impurity strength V_0. The impurity is located in the channel edge for $x_0=-15$, $y_1=8$, and $y_2=12$. Other parameters are the same as Fig.2.

[VI] Dual-frequency modulation and sideband asymmetry characteristics in quantum transport through quantum dot:

a. Shifting of resonance levels

      In this subsection, we discuss the shifting of the resonance levels in an open quantum dot confined by V_{s1} on the left and V_{s2} on the right.
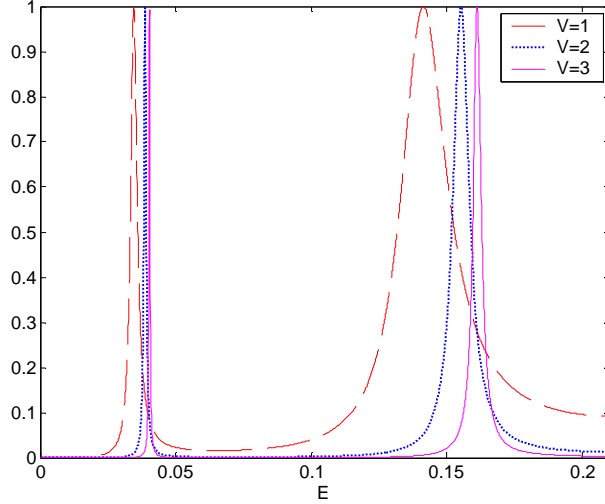

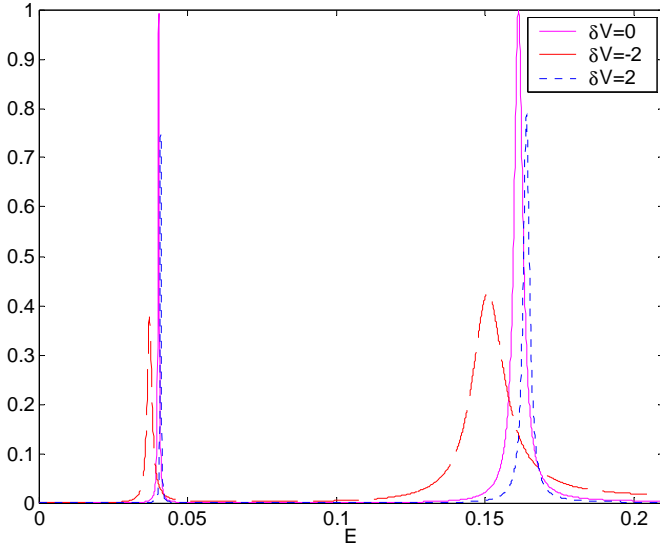Fig. 1: Total current transmission coefficient of a quantum dot with a=15, and $V_{s1}=V_{s2}=V$.

Fig. 2: Total current transmission coefficient of a quantum dot with a=15, $V_{s1}=3$, $V_{s2}=V+\delta V$.

      As shown in Fig. 1, we acquire sharper resonance states with stronger confinements to a quantum dot, but broader and lower ones with weaker static confinements. The transmission coefficient of each case achieves 1. In Fig. 2, when we add an additional part δV to one of the static barriers making the quantum dot asymmetric, the resonance levels also shift to higher energies or lower energies when δV is, respectively, positive or negative. Another interesting feature in Fig. 2 is that the transmission coefficient does not achieve 1 when the quantum dot is asymmetric.
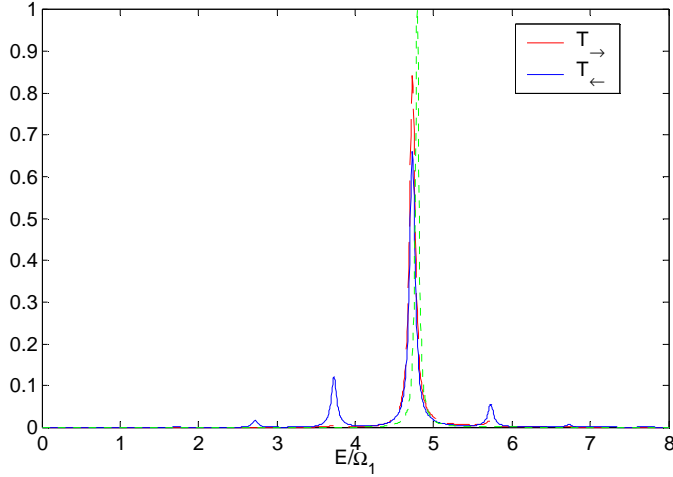
Fig. 3: Current transmission of a=15, $V_{s1}=V_{s2}=3$, $V_{d1}=0$, $V_{d2}=2$, and $\Omega_2=0.0084$. Dotted line represents the resonance state of the quantum dot without time dependent potential.
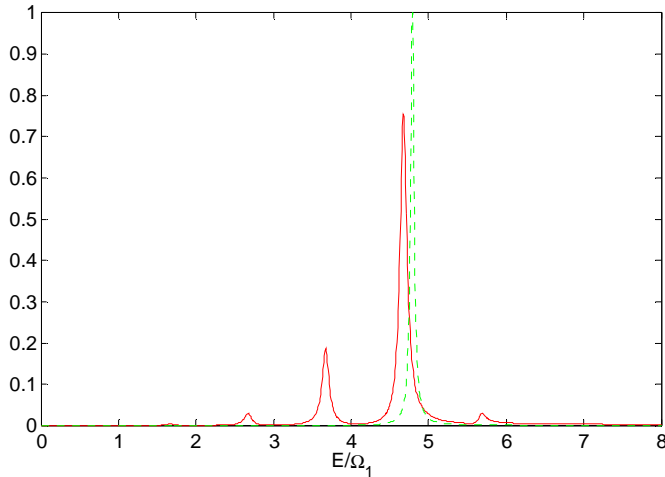

Fig. 4: Current transmission of a=15, a=15, $V_{s1}=V_{s2}=3$, $V_{d1}=V_{d2}=2$, and $\Omega_1=\Omega_2=0.0084$. T and T are identical. Dotted line represents the resonance state without time dependent potential.

We then apply time-dependent potential(s) to the confinement of a quantum dot. The magnitude of the confining barrier will change periodically. Therefore, resonance levels will also shift with time, but the overall effect (after time averaging) of the shift is towards lower-energy end. This can be referred back to Fig. 3.1.2. The degree of shifting towards lower energy is greater than that of shifting towards higher energy, making the overall effect shift to the left.

In Fig. 4, we applied two oscillating barriers to the quantum dot. The shift of resonance state is therefore further enhanced.

b. Sideband Characteristics

In this subsection, we discuss sideband characteristics under several different time-dependent modulations on the confinement of the open quantum dot.

Sideband Features of Single Oscillating Potential:

Only one time-dependent potential is applied to the confinements of the quantum dot. Either $V_{d1}cos\Omega_1t$ is applied on the left, or $V_{d2}cos\Omega_2t$ is applied on the right of the quantum dot.
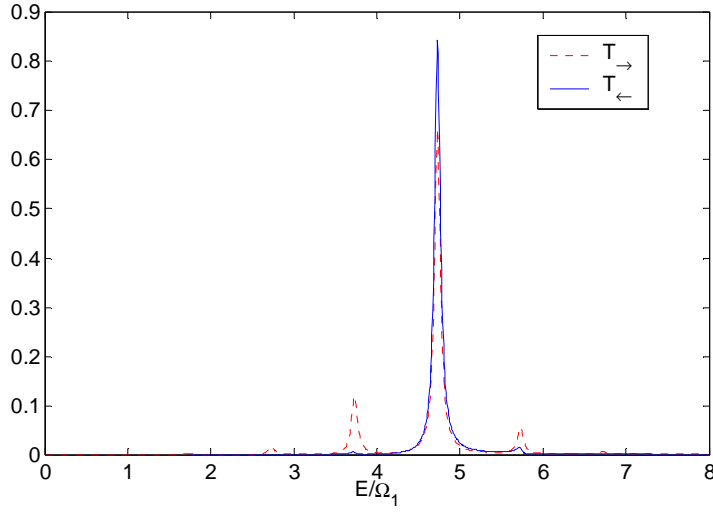
(I) $\Omega_2=\Omega_1$:

Fig. 5: Current transmission of a=15, a=15, $V_{s1}=V_{s2}=3$, $V_{d1}=2$, $V_{d2}=0$, and $\Omega_1=0.0084$.

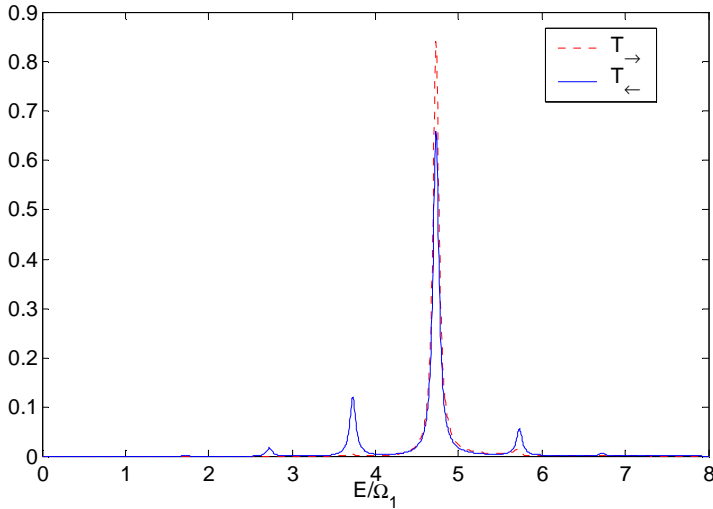Fig. 6: Current transmission of a=15, $V_{s1}=V_{s2}=3$, $V_{d1}=0$, $V_{d2}=2$, and $\Omega_2=0.0084$.

Fig. 5 and Fig. 6 are complementary to each other due to the same oscillating frequency, exhibiting the same sideband features. In Fig. 5, because only $V_{d1}cos\Omega_1 t$ is applied to the quantum dot (applied on the left of the quantum dot), sideband characteristics for electrons incident from the right is not as notable as those of electrons incident from the left.

(II) $\Omega_2=n\Omega_1$:

Within this case we set $\Omega_2=2\Omega_1$, and, again, either $V_{d1}cos\Omega_1 t$ is applied on the left, or $V_{d2}cos\Omega_2 t$ is applied on the right of the quantum dot.

In Fig. 7, 8, and Fig. 9, we can see that sideband structures for $T_{\rightarrow}$ are more significant, whereas sideband structures are more significant for $T_{\leftarrow}$ in Fig. 8, and Fig. 9.

When only $V_{d1}cos\Omega_1 t$ is applied, electrons incident from the right seem to be "screened" by V_{s2} before encountering the oscillating barrier. Hence, it's easier for electrons incident from the left to make transition by resonance levels when $V_{d1}cos\Omega_1 t$ is applied, therefore making the side-peak features more significant. The condition totally reverses when $V_{d2}cos\Omega_2 t$ is applied on

the right of the dot.
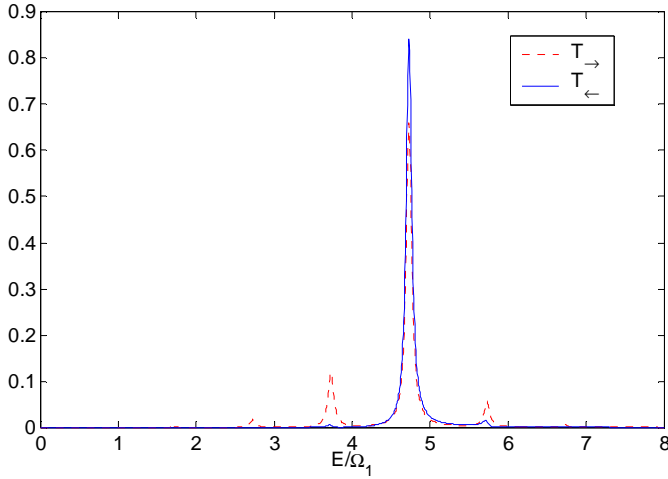
Fig. 7: Current transmission of $a=15$, $V_{s1}=V_{s2}=3$, $V_{d1}=2$, $V_{d2}=0$, and $\Omega_1=0.0084$.
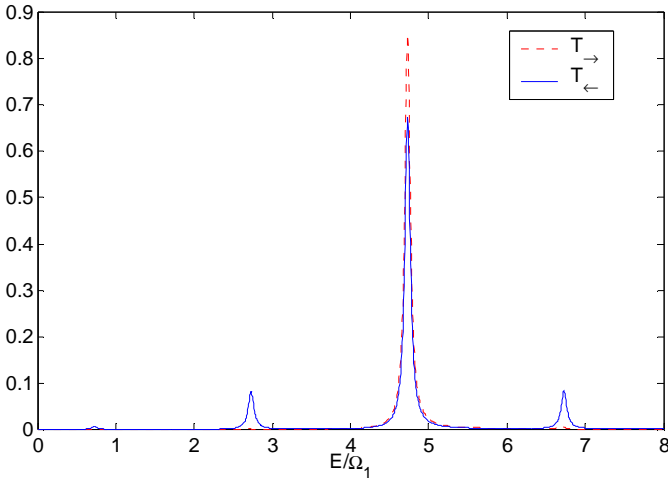
Fig. 8: Current transmission of $a=15$, $V_{s1}=V_{s2}=3$, $V_{d1}=0$, $V_{d2}=2$, and $\Omega_2=2\Omega_1=0.0168$.
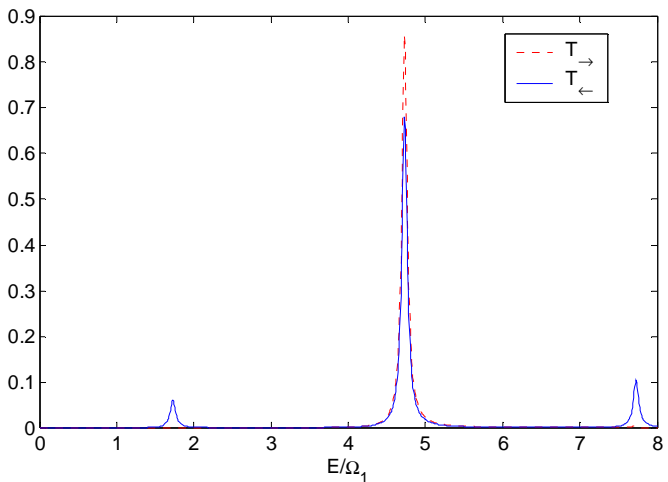
Fig. 9: Current transmission of $a=15$, $V_{s1}=V_{s2}=3$, $V_{d1}=0$, $V_{d2}=2$, and $\Omega_2=3\Omega_1=0.0252$.

c. Double Oscillating Potentials

(I) $\Omega_2=\Omega_1$:

In Fig. 10, only T is shown because T and T are exactly the same under such symmetric condition. The special feature is that side-peak structures are more notable at the left of the

resonance state implying electrons are more possible to absorb n-Ω_1 energy from the system.
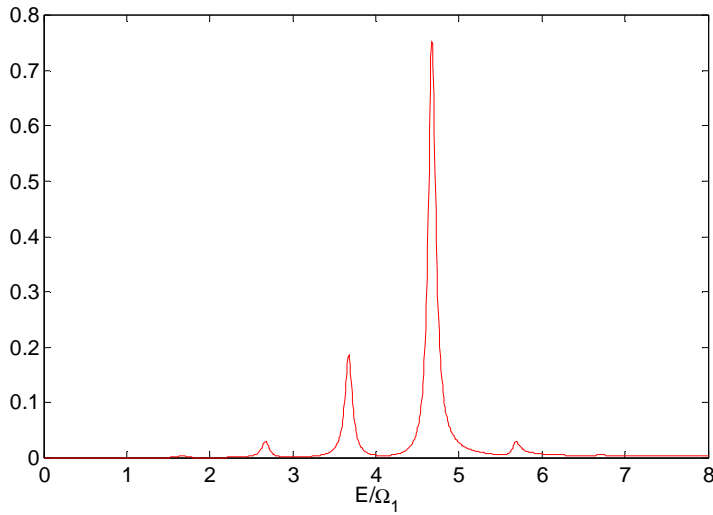
Fig. 10: Current transmission of $a=15$, $V_{s1}=V_{s2}=3$, $V_{d1}=V_{d2}=2$, and $\Omega_2=\Omega_1=0.0084$.

d. Sideband Features When Resonance States Approach Subband Bottom

From Fig. 3.2.9 and Fig. 3.2.10 we find that the relative strength of the two sidepeaks beside the resonance state will reverse when approaching subband bottom.
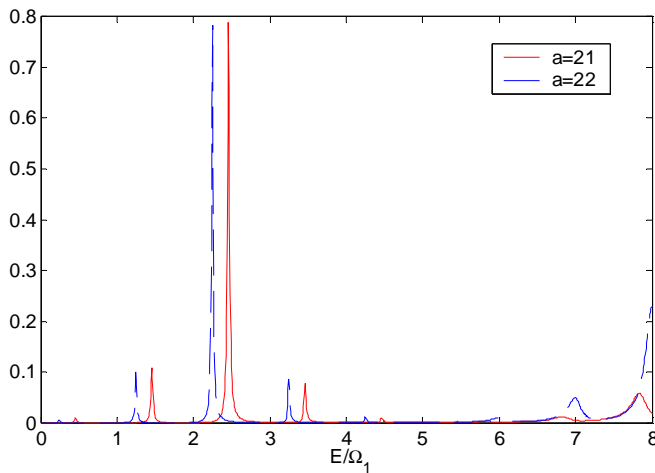
Fig. 11: Current transmission of $V_{s1}=V_{s2}=3$, $V_{d1}=V_{d2}=2$, $\Omega_1=\Omega_2=0.0084$ under $a=21$, and $a=22$.
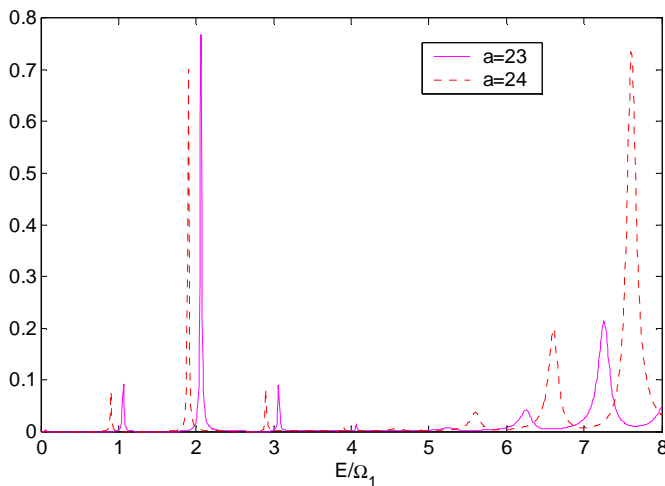
Fig. 12: Current transmission of $V_{s1}=V_{s2}=3$, $V_{d1}=V_{d2}=2$, $\Omega_1=\Omega_2=0.0084$ under $a=23$, and $a=24$.

[VI] The conductance of double quantum point contacts under de-phase process:

The double QPCs with de-coherent scattering process [69] have been studied and the structure is shown in the Fig. 1.
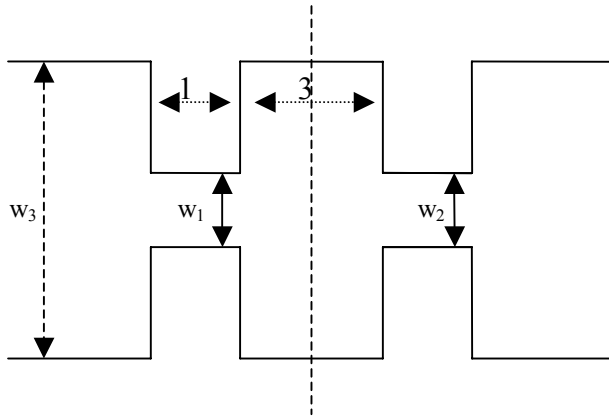
Fig. 1: Our model is a double constriction with a cavity region. The narrow constriction can be regarded as a quantum point contact [70]. The dimensionless unit of length is $1/k_f$.
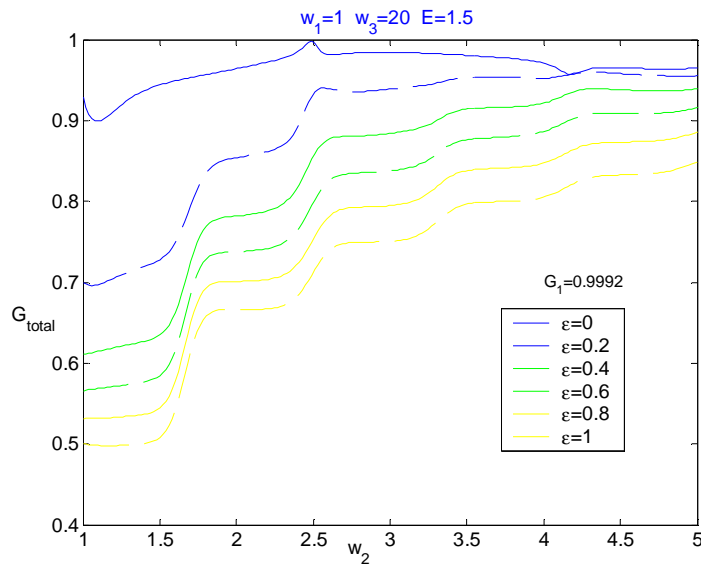
Fig. 2: In classical picture, a QPC can be regarded as a resistance related to its width. This figure shows calculated total conductance as a function of the width of QPC2 for various de-coherent strength. The width of QPC1 is fixed.

The de-coherent strength parameter is and E is the incident energy. It represents how the de-coherent strength influents the total conductance. =0 occurs when double QPCs in series when coherent length is infinite. If de-coherent strength is raising up, the total conductance approaches the classical theoretical results and the de-coherent process increases the resistance so the total conductance is lowering down.
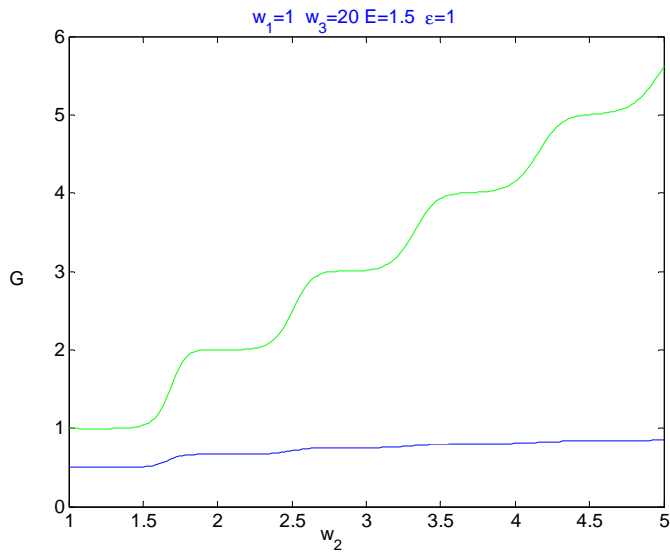
Fig. 3: It is shown the double QPC are fully de-coherent. So the total conductance is the conductance for two QPC in series. Green line is the conductance of QPC2 and be quantized conductance as an individual QPC [71].
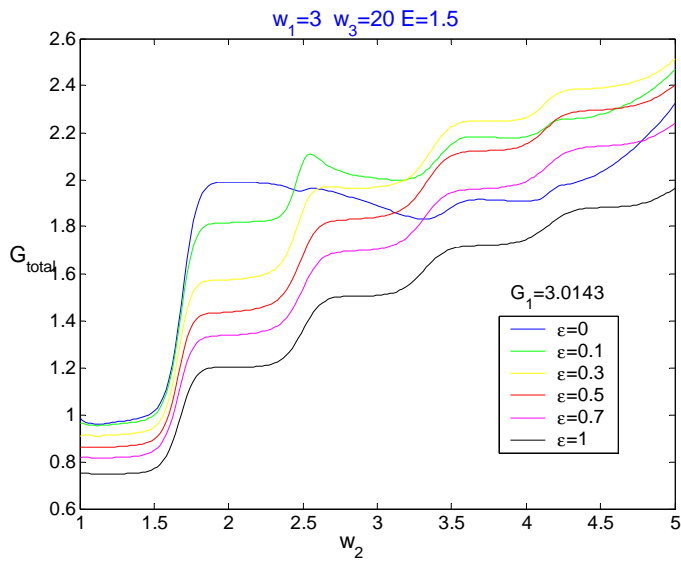
Fig. 4: For the specific case, the total conductance is increased when de-coherent strength is turned on. The reason is the resonance occurs in such specific case.
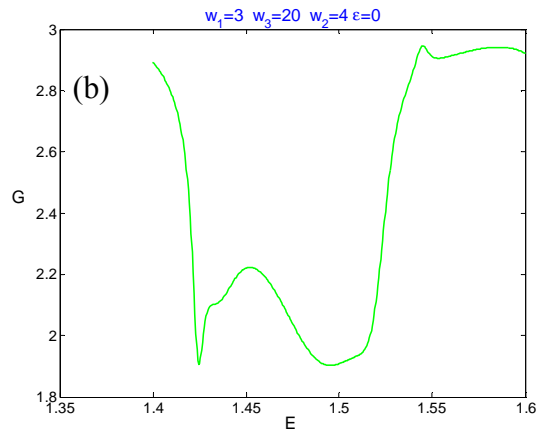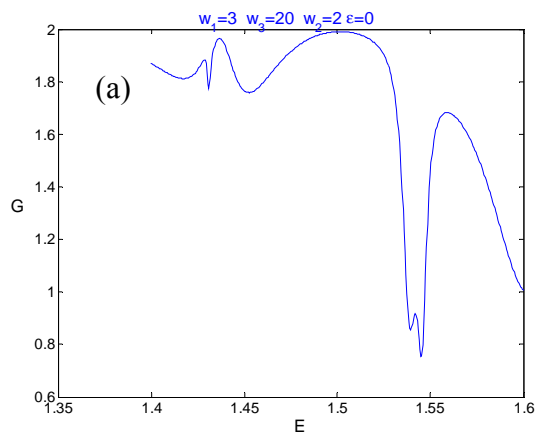
Fig. 5: The theoretical conductance for double QPC in series is plotted as a function of incident energy.

We can obtain the dip structure when we check the relation between total conductance and incident energy in Fig. 4. At the same incident energy of Fig. 3, the Fig. 5 (a) is the normal case and we can find dip structure in Fig. 5 (b). It supports our above theoretical assumption.

[VII] The analytic analysis of Fano resonance transport through a mesoscopic two-lead ring:
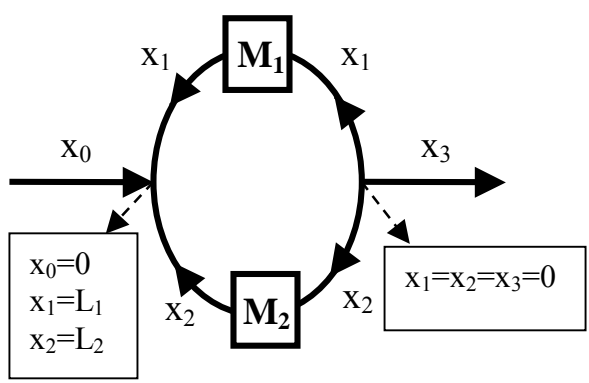
Fig. 1: The generic system we consider has two leads. The boxes on the ring labeled $M_{1,2}$ represent the scatters. A coordinate system x_i is defined for the line segment labeled by i (i=1, 2 and 3). While the arrows denote the increasing direction of the coordinates, the right Y-junction is defined at $x_1 = x_2 = x_3 = 0$, and the left Y-junction is at $x_0=0$, $x_1=L_1$, and $x_2=L_2$.

Unequal armlengths:

We investigate the case of different armlengths in the ring but clean transport channel. This is described by $M_1=M_2=1$ and the transmission amplitude A_3 is reduced to

$$A_3 = \frac{i\left(\sin kL_1 + \sin kL_2\right)}{1-\exp\left(-ik\left(L_1+L_2\right)\right)-\frac{1}{4}\left[\cos\left(k\left(L_1+L_2\right)\right)-\cos\left(k\left(L_1-L_2\right)\right)\right]} \quad ....(1)$$

The observation of the detuned zeroes in the numerator and denominator directly implies that the above numerical results can be casted into the usual Fano resonance expression, and the relation between the resonant dip's width and detuning from perfectly constructive 2PI be investigated more closely. To be self-contained, first we give a very brief review of the Fano resonance discussed in Fano's original paper. In a tunneling process, if there simultaneously involves a non-resonant tunneling, which is almost energy independent and can be simply described by a complex-valued tunneling amplitude t_0, and a resonant tunneling at incident energy $\varepsilon=0$ which can be approximately described by a complex-valued tunneling amplitude $t_r = za/(\varepsilon + ia)$, where z is a complex-valued number describing the relative strength of the non-resonant and resonant tunneling, and a is a real-valued number characterising the width of the resonant tunneling. The total tunneling amplitude would be $t_{tot} = t_0 + t_r = (\varepsilon + qa)/(\varepsilon + ia)$, and the total tunneling robability $T=\left|t_{tot}\right|^2$ would be

$$T=\left|t_0\right|^2 \frac{\left|\varepsilon+qa\right|^2}{\varepsilon^2+a^2} \quad \ldots\ldots\ldots\ldots(2)$$

where $q \equiv z/t_0 + i$, is the Fano parameter. We will briefly describe the behavior of the above tunneling probability. In the case of $a \neq 0$, when $q \neq 0$, T gives a dip/peak when the numerator/denominator in Eq.2 is close to zero. When $q = 0$, T has only a dip at $\varepsilon = 0$. The case of $\mathrm{Im}\, q = 0$ is discussed comprehensively in Fano's original paper. In the case of $a \to 0$, the numerator and denominator in Eq.2 can become exact zeroes but, they are all first order zeroes at $\varepsilon=0$ and hence they cancel each other and gives a finite transmission amplitude. This is actually just the case of commensurate armlength ratio L_2/L_1 we have discussed. Since we have analytically found that all the dips can only appear at $k = k_m$, where $k_m(L_1 + L_2) = 2m\pi$ and m is an integer defines k_m, we expand the tunneling amplitude A_3 near a dip by letting $\delta = (k - k_m)(L_1 + L_2)$. Since we also know that the dips appear when $k_m(L_1 - L_2) \neq 2n\pi$, where n is an integer, we define a detuning from a perfectly constructive 2PI δ by $k_m(L_1 - L_2) = 2n\pi + \delta$, where Δ is from $-\pi$ to $+\pi$ (note that given an m \$m\$, n \$n\$ is determined). Then we expand A_3 at the vicinity of a dip when both the dimensionless δ and Δ are small. We have expanded Eq.1 for the case of $\max(|\delta|) : |\Delta|$ and $|\Delta| = \pi$. We expand the numerator to the third order and the denominator to the second order, and we obtain an approximate transmission amplitude

$$A_3 \; ; \; (-1)^{m+n}\left[1 - \frac{1}{8}\Delta^2 - \frac{1}{4}\frac{L_1-L_2}{L_1+L_2}\Delta\delta - \frac{1}{6}\frac{L_1^3+L_2^3}{(L_1+L_2)^3}\delta^2\right] \times$$
$$\frac{\delta}{\delta + i\left[\frac{1}{8}\Delta^2 + \frac{1}{4}\frac{L_1-L_2}{L_1+L_2}\Delta\delta - \frac{1}{8}\left[5 - \left(\frac{L_1-L_2}{L_1+L_2}\right)^2\right]\delta^2\right]} . \quad \ldots\ldots\ldots\ldots(3)$$

The fractional part can be viewed as a $q = 0$ Fano resonance with a δ-dependent width, and the part other than the fractional part can be viewed as an envelope function. It is seen that within this range of δ the line shape is not in the conventional Fano form. But if we further restrict ourselves to the range of δ is an order of magnitude smaller than Δ, i.e., $\max(|\delta|) : \Delta^2$, the expression in Eq. 3 can be further simplified to

$$A_3 \; ; \; (-1)^{m+n}(1 - \frac{\Delta^2}{8})\frac{\delta}{\delta + i\frac{\Delta^2}{8}}, \quad \ldots\ldots\ldots\ldots\ldots(4)$$

which is exactly in the form of the conventional $q = 0$ Fano resonance, which has only a dip. Note that the parameter δ is a dimensionless wavevector but not energy. When the detuning Δ approaches zero, the width of the dip (: Δ^2) approaches zero and the dip becomes infinitely sharp and vanishes. There are a few noteworthy points here. If one adopts the conventional understanding of the Fano resonance lines with the usual notions of quasibound states and their lifetimes, the ``lifetimes" of the ``quasibound states" our case might seem can be drastically tuned by a slight tuning of the armlength ratio! Moreover, the two arms of the ring are all the same besides their lengths, and the SWR at $k(L_1 + L_2) = 2m\pi$ also occurs in the entire ring, therefore there is no obvious distinction between the ``resonant" and ``non-resonant" tunneling paths in

here.

On the other hand, we also have investigated the transmission amplitude A_3 for the case of $L_1 = L_2 = L$, in the complex wave number $\overset{o}{k}$ plane. This is a common way to investigate the quasibound states in the tunneling paths, the states in the ring in our case. In this special case of $L_1 = L_2 = L$, we can readily find poles at $\overset{o}{k}L = n\pi - i\mathrm{Ln}3$, where n is an integer. Though the $\mathrm{Re}\,\overset{o}{k}$ does correspond to a standing wave in an isolated ring with circumference $2L$, the $\mathrm{Im}\,\overset{o}{k}$ is large and comparable to the spacing in the $\mathrm{Re}\,\overset{o}{k}$. This indicates that these ``quasibound'' states are vaguely defined and this is in congruent with the fact that the ring is open. It is also inappropriate to view any of these states signified by the poles as a quasibound state in Fano's original formalism, which always gives a peak-dip pair profile at near the quasibound state energy. In spite of this, the transmission dips can be created and sharp. As we will see in the later subsections, these standing wave states are also related to the formation of the peak-dip pairs in thetransmission spectrum when impurity potential is included.

It is thus seen that the conventional Fano resonance scheme with straightforward notions like non-resonant and resonant tunneling paths, lifetime of the quasibound states, might be hard to provide a consistent understanding basis of the above results of equal armlengths and slightly unequal armlengths. This reveals the logic that though when there are resonant and non-resonant paths in a tunneling process there will be a Fano resonance line, the reversed statement, when there is a Fano lineshape then there are resonant and non-resonant tunneling paths in the tunneling process, may {\it not} be always true. In other words,though the mathematical form of the resulting tunneling probability can be unanimously in the Fano form as in Eq. 2, the physical contents could be quite different.

Single impurity

This subsection considers the case of a point impurity is embedded into the ring. The impurity is described by a Dirac-δ function potential and this model should be applicable for local potentials with extensions small compared with the wavelengths of the itinerant electrons and armlengths of the ring. The impurity is embedded into arm 1 by adding the potential $V_1\delta(x_1 - X_1)$, where V_1 is the strength of the impurity and X_1 is the location of the impurity in coordinate x_1 on arm 1, and the corresponding transfer matrix is

$$M_1 = \begin{bmatrix} 1 - \dfrac{imV_1}{\hbar^2 k} & -e^{-i2kX_1}\dfrac{imV_1}{\hbar^2 k} \\ e^{i2kX_1}\dfrac{imV_1}{\hbar^2 k} & 1 + \dfrac{imV_1}{\hbar^2 k} \end{bmatrix} \quad\ldots\ldots\ldots\ldots(5)$$

Henceforth we will use the dimensionless parameter $v_1 \equiv mL_1V_1/(2\pi\hbar^2)$ to characterize the

impurity strength. It is noted that the transfer matrix has the symmetry $M_1^{11} = (M_1^{22})^*$ and

$M_1^{12} = (M_1^{21})^*$. Arm 2 is clean and hence $M_2 = 1$.

Figure 2 shows how the asymmetric Fano-type resonance arises as the strength of the impurity on arm 1 grows. We have chosen $L_1 = L_2$ and $X_1 / L_1 = 0.3$ in Fig. 2. Such a peak-dip line shape resonance is in contrast with the mere dip resonance in the without impurity case, but both of them are seen to develop from zero widths. However small the width of the Fano resonance, it is seen that the peaks always reach one and the dips always reach zero. Mathematically the dips are also due to the lift of zeroes in the denominator D. It is noted that the dips are not necessarily at the eigenenergies of an isolated ring with a point

Fig. 2: The transmission probability T is shown versus the dimensionless wave number $kL_1/(2\pi)$ for $L_1=L_2$ and a point impurity at $X_1/L_1=0.3$ with strength $v_1=0.2$, 0.8, and 10 (cutoff limit) [From (a) to (c)]. Each of the panels has a height of 1. The Fano resonance lines are seen to collapse at the limit $v_1=0$ by shrinking their widths. The square roots of the magnitude of the numerator C and denominator D of the transmission amplitude, $\sqrt{|C|}$ (red) and $\sqrt{|D|}$ (blue), are also plotted [in (d)] for $v_1=0.8$ to illustrate how the Fano resonance arises.

impurity. When the impurity strength becomes considerable, the dips depend very much on the location of the impurity since both the impurity and Y-junctions have a substantial effect on the standing waves in the ring. At the strong impurity limit, the zero transmission dips are wide and located at kX_1 and $k(L_1 - X_1) = \text{integer} \times \pi$, and that agrees with the result of a 1D wire with stubs. The arm is essentially cutoff when the impurity is strong, and our case is equivalent to a 1D wire with two stubs of lengths X_1 and $L_1 - X_1$ attached. There will be zero transmission when the length of any one stub is such that an integral number of half-wavelengths can just be fitted in.

Similar to the collapse of resonant dips, collapse of Fano peak-dip pairs is also seen to occur. In Fig. 3 we have shown the transmission probability for the case of the impurity is located near a commensurate location in the ring. We have chosen $L_1 = L_2$ and $X_1/L_1 : 1/3$, and the Fano resonance lines at $kL_1/(2\pi) = 1.5$, 3 and 4.5 are seen to collapse at $X_1/L_1 : 1/3$. The expressions for C and D in this case are complicated and a detailed analytic analysis is difficult. Nevertheless it can be readily verified that at a k that simultaneously satisfies $kL_1 = n_1\pi$,

$kL_2 = n_2\pi$, $kX_1 = n_1'\pi$, where n_1, n_2 and n_1' are integers, and $n_1 + n_2$ is even [i.e., $k(L_1 + L_2) = \text{integer} \times 2\pi$], both C and D vanish but the transmission amplitude

$A_3 = C/D = (-1)^{n_1}\left[1 + imV_1/(\hbar^2 k)\right]^{-1}$ is nonzero. At such a mathematically ``accidental'' nonzero transmission, it is expected that a slight detuning of X_1 can generate a transmission zero as in those cases discussed before. Nevertheless, the nearby perfect transmission peak seems to have no intuitive explanation. Note that the above mentioned conditions for k also imply that $k(L_1 - L_2) = \text{integer} \times 2\pi$.
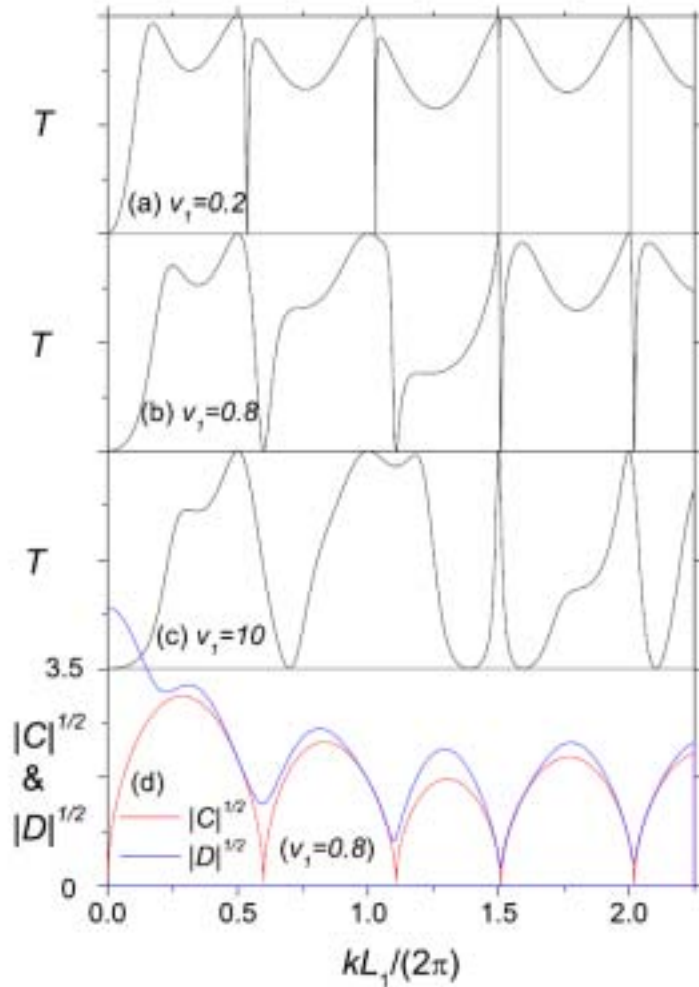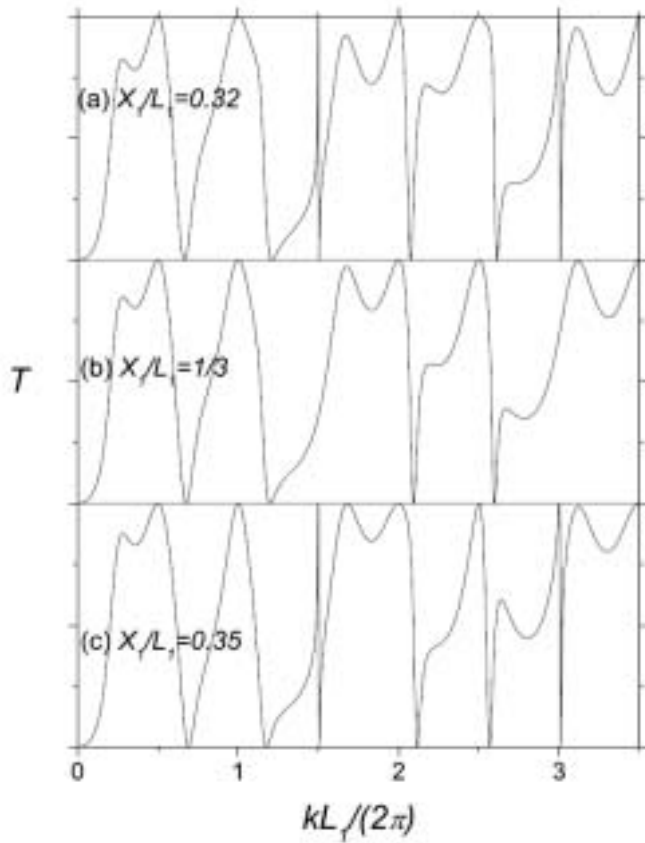

Fig. 3: The transmission probability T is shown versus the dimensionless wave number $kL_1/(2\pi)$ for $L_1=L_2$ and a point impurity with strength $v_1=2$ at $X_1/L_1=0.32$, 1/3, and 0.35 [from (a) to (c)]. All the panels have heights of 1. the Fano resonance lines at $kL_1/(2\pi)\sim1.5$ and 3 are seen to collapse at the limit $X_1/L_1=1/3$.

We can also get an approximate transmission amplitude at the vicinity of a sharp peak-dip pair when the detuning of the impurity from an commensurate location is small, and investigate more closely the relation of the resonant width to the detuning. Since we know that under some commensurate conditions, i.e., rational L_2/L_1 and X_1/L_1, the peak-dip pair collapses at some $k = k_0$, where k_0 is defined by $k_0L_1 = n_1\pi$, $k_0L_2 = n_2\pi$, where $n_1 + n_2$ is even, and $kX_1 = n_1'\pi$, we can make an expansion for the case of a small detuning of the impurity from the

commensurate location by letting $kX_1 = n_1'\pi + \Delta$ under the condition $k_0L_1 = n_1\pi$,

$k_0 L_2 = n_2 \pi$,where $n_1 + n_2$ is even. Defining a dimensionless wavevector $\delta = k(L_1 + L_2) - (n_1 + n_2)\pi$, and consider the regime $\max(|\delta|)$: Δ^2 and $|\Delta| = \pi$, also assuming that $\nu_i \equiv v_1/[(n_1 + n_2)\pi]$ is of the order of 1, we can expand the numerator C and denominator D to the lowest nonvanishing order and obtain the approximate transmission amplitude

$$A_3 = \frac{(-1)^{n_1}}{1 + i\nu_i} \frac{\delta - 2\nu_i \Delta^2}{\left[\delta - \dfrac{2\nu_i \Delta^2}{1 + \nu_i^2}\right] + i\dfrac{2\nu_i \Delta^2}{1 + \nu_i^2}} \quad \ldots\ldots\ldots\ldots(6)$$

The zero of the numerator is seen to occur at $\delta = 2\nu_i \Delta^2$, while the zero of the real part of the denominator is seen to occur at $\delta = 2\nu_i \Delta^2 /(1 + \nu_i^2)$. The two zeroes can only be equal when $\nu_i = 0$ or $\Delta = 0$ and such a situation of detuned zeroes corresponds to the case of a nonzero Fano parameter q, which results in a peak-dip pair. Since $(1 + \nu_i^2) > 1$, when $\nu_i > 0$ (the impurity potential is repulsive), the peak appears preceding the dip, if $\nu_i < 0$ (the impurity potential is attractive), the order of appearance of the peak and dip is swapped. On the other hand, the overall width of the resonant line depends neither on the sign of the impurity potential (ν_i) nor the detuning (Δ).

Appendix A:

Strain induced coupling of spin current to nanomechanical oscillations

A. G. Mal'shukov,[1] C. S. Tang,[2, *] C. S. Chu,[3] and K. A. Chao[4]

[1]*Institute of Spectroscopy, Russian Academy of Science, 142190, Troitsk, Moscow oblast, Russia*
[2]*Physics Division, National Center for Theoretical Sciences, P.O. Box 2-131, Hsinchu 30013, Taiwan*
[3]*Department of Electrophysics, National Chiao Tung University, Hsinchu 30010, Taiwan*
[4]*Solid State Theory Division, Department of Physics, Lund University, S-22362 Lund, Sweden*

We propose a setup which allows to couple the electron spin degree of freedom to the mechanical motions of a nanomechanical system not involving any of the ferromagnetic components. The proposed method employs the strain induced spin-orbit interaction of electrons in narrow gap semiconductors. We have shown how this method can be used for detection and manipulation of the spin flow through a suspended rod in a nanomechanical device.

An ability to control the spin transport in semiconductors is a key problem to be solved towards implementation of semiconductor spintronics into quantum information processing [1, 2, 3]. Many methods have been proposed to achieve control of the electron spin degree of freedom using magnetic materials, external magnetic fields and optical excitation (for a review see Ref. [3]). Other promising ideas involve the intrinsic spin-orbit interaction (SOI) in narrow gap semiconductors to manipulate the spin by means of electric fields [4] and electric gates [5, 6]. Recently, some of these ideas have been experimentally confirmed [7, 8].

In semiconductors the spin-orbit effect appears as an interaction of the electron spin with an effective magnetic field whose direction and magnitude depend on the electron momentum. A specific form of this dependence is determined by the crystal symmetry, as well as by the symmetry of the potential energy profile in heterostructures. In strained semiconductors new components of the effective magnetic field appear due to violation of the local crystal symmetry [9]. The effect of the strain induced SOI on spin transport was spectacularly demonstrated by Kato et. al. in their Faraday rotation experiment [8]. An interesting property of the strain induced SOI is that the strain can be associated with mechanical motion of the solid, in particular, with oscillations in nanomechanical systems (NMS), in such a way making possible the spin-orbit coupling of the electron spin to nanomechanical oscillations. At the same time a big progress in fabricating various NMS [10] allows one to reach the required parameter range to observe subtle effects produced by such a coupling.

In this Letter we will consider NMS in the form of a suspended beam with a doped semiconductor film epitaxially grown on its surface (see Fig. 1). An analysis of the SOI in this system shows that the flexural and torsion vibrational modes couple most efficiently to the electron spin. As a simple example, we will focus on the torsion mode. The strain associated with torsion produces the spin-orbit field which is linear with respect to the electron momentum and is directed perpendicular to it. This field varies in time and space according to respective variations of the torsion strain. Due to the linear dependence on the momentum, the SOI looks precisely as interaction with the spin dependent electromagnetic vector potential. An immediate result of this analogy is that the time dependent torsion gives rise to a motive force on electrons. Such a force, however, acts in different directions on particles with oppositely oriented spins, inducing thus the spin current in the electron gas. The physics of this phenomenon is very similar to the spin current generation under time dependent Rashba SOI, where the time dependence of the SOI coupling parameter is provided by the gate voltage variations [6]. In the present work we will focus, however, on the inverse effect. Due to the SOI coupling, the spin current flowing through the beam is expected to create a mechanical torsion. The torque effect on NMS due to spin flow has been previously predicted by Mohanty et. al. [11] for a different physical realization, where the torque has been created by spin flips at the nonmagnetic-ferromagnetic interface. They also suggested an experimental set up to measure such a small torque. As it will be shown below, the torque due to the SOI effect can be by 2 orders of magnitude stronger than the torque produced by the current flowing through the FM-NM interface. Hence, the SOI effect can be measured by the same method as was proposed in Ref. [11]. Besides this method, other sensitive techniques for displacement measurements can be employed [12].

The system under consideration is a rectangular beam of the total length L_t, width b, and thickness c. The semiconductor film with the thickness $c/2$ occupies the length L of the beam. The rest part contains a metal film. It can also include some additional elements for detection of the torque, for example in Ref. [11]. Here we will consider an example when the spin current is created by diffusion of the spin polarization from the left contact in Fig.1. Therefore, there is no electric current flow through NMS. The spin polarization diffuses towards the metal film which, due to its relatively high conduction, can play an important role as a reservoir for the spin polarization relaxation. We start from the strain-induced SOI [9]

$$
\begin{aligned}
H_{SO1} &= \alpha \left[\sigma_x \left(u_{zx} k_z - u_{xy} k_y \right) + \sigma_y \left(u_{xy} k_x - u_{yz} k_z \right) \right. \\
&\quad + \sigma_z \left(u_{yz} k_y - u_{zx} k_x \right) \Big] \\
&\quad + \beta \left[\sigma_x k_x \left(u_{yy} - u_{zz} \right) + \sigma_y k_y \left(u_{zz} - u_{xx} \right) \right. \\
&\quad \left. + \sigma_z k_z \left(u_{xx} - u_{yy} \right) \right],
\end{aligned}
\tag{1}
$$

where u_{ij} are elements of the strain tensor, σ_i are Pauli matrices and k_i denote components of the electron wave vector. In the narrow gap semiconductors the parameter β is usually much smaller than α [9]. Therefore, the term proportional to β will be omitted below. Besides the strain induced H_{SO1}, the total SOI Hamiltonian also includes the strain independent interaction H_{SO2}. Because of submicron cross-section dimensions of the doped semiconductor film, H_{SO2} will be determined by the bulk Dresselhaus term [14].

$$
H_{SO2} = \gamma \sum_{ijn} \epsilon^{ijn} k_i (k_j^2 - k_n^2)
\tag{2}
$$

This interaction, in the range of doping concentrations 10^{17} and higher, provides the main mechanism for spin relaxation in bulk materials [9].

Since $L_b \gg b, c$, the major contribution to the strain comes from flexural and torsion motions of the rod [13]. Within the isotropic elastic model the flexural motions are represented by the diagonal elements u_{xx} and u_{yy} [13] which do not enter into the first square brackets of Eq. (1). On the other hand, due to the crystal anisotropy effects, the u_{xy} components are not zero for such sort of motion and could contribute to Eq. (1). We, however, will consider the simplest example of torsion motions of the rod within the isotropic elastic model. In this case the strain can be represented as [13]

$$
u_{yx} = \tau(x) \frac{\partial \chi}{\partial z}; \quad u_{zx} = -\tau(x) \frac{\partial \chi}{\partial y}; \quad u_{yz} = 0, \tag{3}
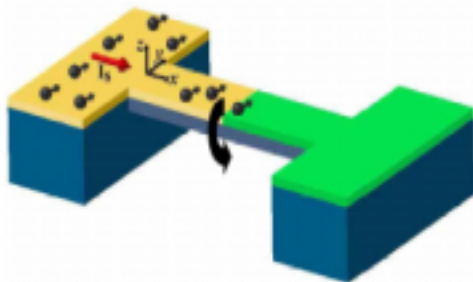$$

FIG. 1: Schematic illustration of electromechanical spin current detector, containing a suspended semiconductor-metal (S-M) rectangular rod atop an insulating substrate (blue). A spin current is injected from the left semiconductor reservoir (yellow) and then diffuses toward the metallic film (green). While passing through the semiconductor film, the spin current induces torque shown by the black arrow.

where $\tau(x) = \partial\theta/\partial x$ stands for the rate of torsion determined by the torsion angle θ. The function χ depends only on x, y and is uniquely determined by the rod cross section geometry.

The next step is to derive from the one-particle interaction Eq. (1) a Hamiltonian which describes a coupling of the spin current to the strain. The electron system carrying the spin current can be described by a density matrix $\hat{\rho}$. In the framework of the perturbation theory the leading correction to the electron energy due to the SOI induced strain can be obtained by averaging H_{SO1} with $\hat{\rho}$. In the semiclassical approximation such a procedure can be represented as averaging over the classical phase space with the Boltzmann distribution function $\hat{F}_{\mathbf{k}}(\mathbf{r})$. This function is a 2×2 matrix in the spinor space. One can also define the spin distribution function $P_{\mathbf{k}}^i(\mathbf{r}) = (1/2) Tr[\hat{F}_{\mathbf{k}}(\mathbf{r})\sigma^i]$. It is normalized in such a way that the local spin polarization $P^i(\mathbf{r}) = \sum_{\mathbf{k}} \mathbf{P}_{\mathbf{k}}(\mathbf{r})$ We notice, that due to electron confinement in y and z directions, the averages of H_{SO1} containing k_y and k_z turn to zero. Assuming that electron distribution is uniform within the cross section of the semiconductor film one thus obtains, from Eqs. (1) and (3), the SOI energy E_{SO} in the form

$$
\begin{aligned}
E_{SO} &= \alpha \int_0^L dx \frac{\partial\theta}{\partial x} \\
&\quad \times \sum_{\mathbf{k}} k_x \int dy dz \left(P_{\mathbf{k}}^y(x) \frac{\partial\chi}{\partial z} + P_{\mathbf{k}}^z(x) \frac{\partial\chi}{\partial y} \right).
\end{aligned}
\tag{4}
$$

This expression can be further simplified taking into account that χ turns to zero on a free surface [13]. Hence, in the example under consideration $\chi = 0$ on the top and side surfaces of the doped semiconductor film. Consequently, the second term in Eq. (4) vanishes after integration over y. Now Eq. (4) can be expressed in terms of the spin current $J^y(x)$ which is the flux in x-direction of y-polarized spins.

$$
J^y(x) = S \sum_{\mathbf{k}} v_x P_{\mathbf{k}}^y(x), \tag{5}
$$

where $S = bc/2$ is the semiconductor film cross section and v_x is the electron velocity in x-direction [15]. Finally, Eq. (4) can be transformed to

$$
E_{SO} = \gamma \int_0^L dx J^y(x) \frac{\partial\theta}{\partial x}. \tag{6}
$$

where the coupling constant γ is given by

$$
\gamma = \gamma_0 \int_{-\frac{b}{2}}^{\frac{b}{2}} \chi(y, z = 0) \, dy, \tag{7}
$$

where $\gamma_0 = 2m^*\alpha/\hbar S$.

From the last equation, it is seen that the spin-polarized flow imposes a distributed torque on the rod. In

order to study this effect in detail we will neglect, for simplicity, the difference between elastic constants of semiconductor and metal parts of NMS. As such, the equation of motion for the torsion angle can be then written as

$$I\frac{\partial^2\theta}{\partial t^2} - K\frac{\partial^2\theta}{\partial x^2} - \gamma\frac{\partial J^y}{\partial x}\eta(L-x) = 0, \qquad (8)$$

where $\eta(x)$ denotes the Heaviside function, K stands for the torsion rigidity, and I is the moment of inertia. It is easy to figure out that the torque imposed by the SOI on NMS can be expressed as

$$T = \frac{\gamma}{L}\int_0^L dx J^y(x), \qquad (9)$$

and, for the rod clamped on both ends, the torsion angle at $x = L$

$$\theta = \frac{L(L_t - L)}{L_t}\frac{T}{K}, \qquad (10)$$

where L_t is the total length of the rod.

In order to evaluate the torque let us adopt the following simple model, which is also convenient for an experimental realization. Namely, we assume that the spin current is due to spin diffusion from the left contact. The spin polarization $P^y(0)$ can be created there by various methods ranging from absorption of circularly polarized light to injection from a ferromagnet [3]. One more possibility is the electric spin orientation [8]. For the steady state the diffusion equation reads

$$D_i\frac{d^2P^y}{dx^2} - \frac{P^y}{\tau_i} = 0, \qquad (11)$$

where D_i and τ_i are diffusion coefficients and spin relaxation times, with the subscript i indicating the physical quantities in semiconductor $(0 < x < L)$ (i=S) or metal $(x > L)$ (i=M) regions. At the semiconductor-metal interface the diffusion current and magnetization $P^y/N_i(0)$ must be continuous, where $N_i(0)$ is the semiconductor or metal density of states at the Fermi energy [16]. We will assume that the length of the metal part of the rod is larger than the spin diffusion length $l_M = \sqrt{D_M\tau_M}$. Therefore, the spin current passes through the semiconductor film and further decays within the metal film. Obviously, in the considered example there is no charge current through the system. Solving the diffusion equation for $l_S \gg L$ and $(\sigma_M L)/(\sigma_S l_M) \gg 1$, where σ_M and σ_S are the 3D conductivities of metal and semiconductor, respectively, we obtain

$$\overline{J^y} \equiv \frac{1}{L}\int_0^L dx J^y(x) = \frac{D_S P^y(0)S}{L}. \qquad (12)$$

Since the ratio σ_M/σ_S is very big, Eq. (12) is valid in a broad range of not very small L.

For a numerical evaluation of the spin-orbit torsion effect we take $b = 400$ nm and $c = 200$ nm. For a GaAs film the SOI coupling constant $\alpha/\hbar = 4 \times 10^5$ m/sec [17]. From Eq. (7) and Ref. [13], it is easily to obtain the spin-current–torsion coupling parameter $\gamma = \gamma_0 k_2 b^3$, where k_2 is a numerical factor depending on the ratio c/b. At $b/c = 2$ the factor $k_2 = 0.03$. For such numerical parameters we find $\gamma = 2.4 \times 10^{-32}$ J sec. It is interesting to compare the torsion effect from SOI interaction with that produced by spin flips at the FM-SC interface [11]. In the latter case $T = \hbar I_s$, where I_s is the spin current. Comparing this expression with Eq. (9), it is seen that at the same spin currents the SOI effect is much stronger, by the factor $\gamma/\hbar \simeq 2.2 \times 10^2$. At $e\overline{J^y} = 10^{-8}$Å the torque $T = 1.5 \times 10^{-21}$ N m, which is within the sensitivity of the torque measurement set up suggested by Mohanty et. al [11]. Moreover, the measurement sensitivity can be enhanced [18]. In fact, the latter method applies to a time dependent torque in resonance with a NMS oscillation. For such a measurement the spin current could be modulated in time by a narrow gate between the left contact and the rod, or by varying the spin polarization in the left reservoir, for example, if it is created by absorption of circularly polarized light with modulated intensity. On this stage it is instructive to evaluate the spin polarization $P^y(0)$ which can produce a measurable effect on NMS. From Eq. (12), taking $L = 2\,\mu$m, the typical low temperature diffusion constant 300 cm^2/sec and $n = 10^{17}$ cm^{-3}, one obtains $e\overline{J^y} = 10^4(P^y(0)/n)$ nA. Hence, a measurable 10 nA spin current in NMS can be created by diffusion of spin polarization from an adjacent reservoir containing only 0.1% of spin-polarized carriers.

The static torsion angle at $x = L$ can be found from Eq. (10). On the other hand, the maximum torsion effect is obtained for the time dependent spin current in resonance with the NMS fundamental oscillation. In this case θ in Eq. (10) must be multiplied by $Q/2$, where Q is the resonance quality factor, which can be quite large in NMS. To observe this torsion angle it must be much larger than the mean amplitude of its thermal fluctuations $\sqrt{\overline{\delta\theta^2}}$. For a doubly clamped rod

$$\overline{\delta\theta^2} = \frac{k_B T L_t}{\pi^2 K}\sum_{n\geq 1}\frac{1}{n^2}\sin^2(\frac{\pi nL}{L_t}). \qquad (13)$$

For a rectangular cross section with $b/c = 2$, the torsion rigidity $K = 0.057\mu b^3 c$ [13], where $\mu \simeq 3.3 \times 10^{10}$ N/m^2 in GaAs material. Taking $L_t = 5\,\mu$m and all other parameters the same as in the previous paragraph, $Q = 10^4$ and $T = 100$ mK we obtain the ratio $\delta\theta/\theta \simeq 4 \times 10^{-2}$ at $e\overline{J^y} = 10$ nA.

We have considered a simple example of the spin-orbit torque effect produced by spin flux in a diffusive 3D semiconductor film. It would be interesting to study other systems, for example, a superlattice of remotely doped high mobility quantum wells in the ballistic regime (L is

less than the elastic mean free path). In such a system energy dissipation within the semiconductor film is reduced and, apparently, larger spin currents are allowable.

In summary, we propose a nanomechanical system where due to the strain induced spin-orbit interaction the electron spin degree of freedom can couple to NMS mechanical motions. We have shown that this coupling is strong enough to induce the measurable torsion in NMS when the spin polarization flows through the suspended nanobeam. Besides a potential for other possible applications, such NMS can be employed as a sensitive detector of spin currents and spin polarizations. The basic structure can be further modified to create devices for eventual use in spintronics, and spin information processing.

———————

* Electronic address: cstang@phys.cts.nthu.edu.tw

[1] *Semiconductor Spintronics and Quantum Computation*, edited by D.D. Awschalom, N. Samarth, and D. Loss (Springer-Verlag, Berlin, 2002).

[2] S. A. Wolf, *et. al.*, Science **294**, 1488 (2001).

[3] I.Žutić, J.Fabian, and S. Das Sarma, Rev. Mod. Phys. **76**, 323 (2004).

[4] J. Sinova, *et. al.*, Phys. Rev. Lett. **92**, 126603 (2004); S. Murakami, N. Nagaosa and S. Zhang, Science **301**, 1348 (2003); V. M. Edelstein, Solid State Commun., **73**, 233 (1990); A. Voskoboynikov, *et. al.*, Phys. Rev. B, **59**, 12514 (1999); L. S. Levitov and E. I. Rashba Phys. Rev. B **67**, 115324 (2003).

[5] S. Datta and B. Das, Appl. Phys. Lett. **56**, 665 (1990); P. Sharma and P. W. Brouwer, Phys. Rev. Lett. **91**, 16 6801 (2003); M. Governale, F. Taddei, and R. Fazio, Phys. Rev. B **68**, 15 5324 (2003).

[6] A. G. Mal'shukov, *et. al.*, Phys. Rev. B **68**, 23 3307 (2003); C. S. Tang, A. G. Mal'shukov, and K. A. Chao, cond-mat/0412181.

[7] J. Wunderlich, B. Kästner, J. Sinova, and T. Jungwirth, cond-mat/0410295.

[8] Y.K. Kato, *et. al.*, cond-mat/0502627.

[9] G. E. Pikus and A. N. Titkov, in *Optical Orientation*, edited by F. Meier and B. P. Zakharchenya (North-Holland, Amsterdam, 1984).

[10] M. L. Roukes, Phys. World **14**, 25 (2001); H. G. Craighead, Science **290**, 1532 (2000); A. N. Cleland, *Foundations of Nanomechanics* (Springer, Berlin, 2003).

[11] P. Mohanty, G. Zolfagharhani, S. Kettemann, P. Fulde, Phys. Rev. B **70**, 195301 (2004).

[12] R. G. Knobel, A. N. Cleland, Nature **424** 291 (2003).

[13] L. Landau and E. Lifshitz, Course of Theoretical Physics (Pergamon Press, New York, 1986), 3rd ed., Vol. 7.

[14] G. Dresselhaus, Phys. Rev. **100**, 580 (1955).

[15] We neglected the small correction to the spin current associated with Dresselhaus's term $\frac{\partial H_{SO}}{\partial k}$ in the velocity operator.

[16] M. Johnson and R. H. Silsbee, Phys. Rev. B **35**, 4959 (1987); **37**, 5312 (1988).

[17] M. I. D'yakonov, V. A. Marushchak, V. I. Perel', and A. N. Titkov, Sov. Phys. JETP **63**, 655 (1986), [Zh. Eksp. Teor. Fiz. **90**, 1123 (1986)].

[18] P. Mohanty, private communication.

Appendix B:

Visibility of current and shot noise in electrical Mach-Zehnder and Hanbury Brown Twiss interferometers

V.S.-W. Chung[1,2], P. Samuelsson[3], and M. Büttiker[1]

[1]*Département de Physique Théorique, Université de Genève, Genève 4, CH-1211 Switzerland*
[2]*Department of Electronics, National Chiao-Tung University, Hsinchu 30010, Taiwan*
[3]*Division of Solid State Theory, Lund University, Sölvegatan 14 A, S-223 62 Lund, Sweden*
(Dated: May 20, 2005)

We investigate the visibility of the current and shot-noise correlations of electrical analogs of the optical Mach-Zehnder interferometer and the Hanbury Brown Twiss interferometer. The electrical analogs are discussed in conductors subject to high magnetic fields where electron motion is along edge states. The transport quantities are modulated with the help of an Aharonov-Bohm flux. We discuss the conductance (current) visibility and shot noise visibility as a function of temperature and applied voltage. Dephasing is introduced with the help of fictitious voltage probes. Comparison of these two interferometers is of interest since the Mach-Zehnder interferometer is an amplitude (single-particle) interferometer whereas the Hanbury Brown Twiss interferometer is an intensity (two-particle) interferometer. A direct comparison is only possible for the shot noise of the two interferometers. We find that the visibility of shot noise correlations of the Hanbury Brown Twiss interferometer as function of temperature, voltage or dephasing, is qualitatively similar to the visibility of the first harmonic of the shot noise correlation of the Mach-Zehnder interferometer. In contrast, the second harmonic of the shot noise visibility of the Mach-Zehnder interferometer decreases much more rapidly with increasing temperature, voltage or dephasing rate.

I. INTRODUCTION

With the advent of mesoscopic physics, it has become possible to experimentally investigate quantum phase coherent properties of electrons in solid state conductors in a controlled way. In particular, in ballistic mesoscopic samples at low temperatures, electrons can propagate up to several microns without loosing phase information. This opens up the possibility to investigate electrical analogs of various optical phenomena and experiments. An investigation of such analogs is of fundamental interest. On the one hand, it allows one to establish similarities between the properties of photons and conduction electrons, a consequence of the wave nature of the quantum particles. On the other hand, it also allows one to investigate the differences between the two types of particles arising from the different quantum statistical properties of fermions and bosons. For many-particle properties, such as light intensity correlations or correspondingly electrical current correlations, noise, the quantum statistical properties are important.[1,2] Both the wave-nature of the particles as well as their quantum statistics are displayed in a clearcut fashion in interferometer structures. In this work we are concerned with the electrical analogs of two well known optical interferometers, the single-particle Mach-Zehnder (MZ) interferometer and the two-particle Hanbury Brown Twiss (HBT) interferometer.

The MZ-interferometer is a subject of most textbooks in optics.[3] In the framework of quantum optics, considering individual photons rather than classical beams of light, the interference arises due to the superposition of the amplitudes for two different possible paths of a single photon. This leads to an interference term in the light intensity. The MZ-interferometer is thus a prime example of a single particle interferometer.[4] Various electronic interferometers with ballistic transport of the electrons have been investigated experimentally over the last decades, as e.g. Aharonov-Bohm (AB) rings[5] and double-slit interferometers.[6] Detailed investigations of dephasing in ballistic interferometers was carried out in Refs. [7,8]. Only very recently was the first electronic MZ-interferometer realized by Ji et al.[9] in a mesoscopic conductor in the quantum Hall regime. A high visibility of the conductance oscillations was observed, however the visibility was not perfect. This led the authors to investigate in detail various sources for dephasing. As a part of this investigation, also shot noise was measured. Still, some aspects of the experiment are not yet fully understood. Theoretically, Seelig and one of the authors[10] investigated the effect of dephasing due to Nyquist noise on the conductance in a MZ-interferometer. The effect of dephasing on the closely related four-terminal resistance in ballistic interferometers[11] was investigated as well. Dephasing in ballistic strongly interacting systems is discussed by Le Hur.[12,13] Following the experimental work of Ji et al.,[9] Marquardt and Bruder investigated the effect of dephasing on the shot-noise in MZ-interferometers, considering dephasing models based on both classical[14,15] as well as quantum fluctuating fields.[16] Very recently, Förster, Pilgram and one of the authors[17] extended the dephasing model of Refs. [10,14] to the full statistical distribution of the transmitted charge.

The HBT-interferometer[18,19,20] was originally invented for stellar astronomy, to measure the angular diameter of stars. It is an intensity, or two-particle,[4] interferome-

ter. The interference arises from the superposition of the amplitudes for two different two-particle processes. Importantly, there is no single particle interference in the HBT-interferometer. Consequently, in contrast to the MZ-interferometer there is no interference in the light intensity, the interference instead appears in the intensity-intensity correlations. Moreover, the intensity-intensity correlation also display the effect of quantum statistics. Photons originating from thermal sources tend to bunch, giving rise to positive intensity cross correlations. For the electronic analog of the HBT-interferometer, it was the corresponding anti-bunching of electrons that originally attracted interest. It was predicted[1] that the electrical current cross correlations in mesoscopic conductors would be manifestly negative, i.e. display anti-bunching, as a consequence of the fermionic statistics of the electrons. Negative current cross correlations were subsequently observed in two independent experiments.[21,22] Recently, anti-bunching for field emitted electrons in vacuum was also demonstrated.[23] The two-particle interference in the HBT-experiment has received much less attention. We emphasize that while the bunching of the photons was necessary for obtaining a finite, positive cross correlation signal, it was the two-particle effect that was of main importance to HBT since the angular diameter of the star was determined from the two-particle interference pattern. In electrical conductors, two-particle effects in AB-interferometers were investigated theoretically in Refs. [24,25,26]. Only very recently two of the authors and Sukhorukov[27] proposed a direct electronic analog of the optical HBT-interferometer which permits to demonstrate two-particle interference in an unambiguous way.

In this work we investigate and compare in detail the current and and zero-frequency noise in electronic MZ and HBT interferometers. We consider interferometers implemented in mesoscopic conductors in the integer Quantum Hall regime, where the transport takes place along single edge states and Quantum Point Contacts (QPC's) serve as controllable beam splitters. The effect of finite temperature, applied bias and asymmetry, i.e. unequal length of the interferometer arms, is investigated. The strength of the interference contribution is quantified via the visibility of the phase oscillations. The dependence of the visibility on the beam splitter transparencies as well as on the temperature, voltage and asymmetry is discussed in detail. Of interest is the comparison of visibility of the shot-noise correlation of the MZ-interferometer and the HBT-intensity interferometer. Shot noise correlations in the MZ-interferometer exhibit two contributions, one with the fundamental period of h/e and a second harmonic with period $h/2e$. The shot noise correlations in the HBT-interferometer, even though they are due to two particle processes, are periodic with period h/e. Thus the Aharonov-Bohm period can not be used to identify the two particle processes which give rise to the HBT effect. It is therefore interesting to ask whether the HBT two-particle processes

have any other signature, for instance in the temperature or voltage dependence of the visibility of the shot-noise correlation. We find that this is not the case. To the contrary, we find that the the shot noise correlations in the HBT intensity interferometer behave qualitatively similar to the h/e shot noise correlation in the MZ-interferometer. In contrast the $h/2e$ contribution in the shot noise of the MZ-interferometer decreases more rapidly with increasing temperature, voltage or dephasing rate than the h/e oscillation in the MZ- or HBT-interferometer.

We investigate dephasing of the electrons propagating along the edge states by connecting one of the interferometer arms to a fictitious, dephasing voltage probe. In all cases, the current and noise of the MZ-interferometer as well as the noise in the HBT-interferometer, the effect of the voltage probe is equivalent to the effect of a slowly fluctuating phase.

II. MODEL AND THEORY

A. Optical analogs in the Quantum Hall regime

In the paper we consider implementations of the MZ and HBT interferometers in mesoscopic conductors in strong magnetic fields, in the integer Quantum Hall regime.[28] The typical system is a two-dimensional electron gas in a semiconductor heterostructure, with the lateral confinement of the electron gas controllable via electrostatic gating. The transport between reservoirs[29] connected to the conductor takes place along edge states.[30] The edge states, quantum analogs of classical skipping orbits, are chiral, the transport along an edge state is unidirectional. Scattering between edge states is suppressed everywhere in the conductor except at electrostatically controllable constrictions, QPC's.[31,32] For a magnetic field that does not break the spin degeneracy of the edge states, each edge state supplies two conduction modes, one per spin.

These properties make conductors in the integer quantum Hall regime ideal for realizing analogs of optical experiments. First, the edge states correspond to single mode waveguides for the light. The unidirectional motion along the edge states allows for "beams" of electrons to be realized. Second, the QPC's work as electronic beam splitters with controllable transparency. Moreover, due to chirality the beamsplitters are reflectionless, a property essential for the MZ and HBT interferometers but difficult to achieve for beam splitters in conductors in weak (or zero) magnetic fields.[22,33] These properties of conductors in the quantum Hall regime have been demonstrated experimentally in a number of works, see e.g. [9,21,34].

Theoretically, several works have been concerned with the conductance and noise properties of beam splitters and interferometers in Quantum Hall systems, for a recent reviews see e.g. Refs. [2,35]. Recently, it was pro-

posed to use these appealing properties of edge states in the context of orbital[36] quasi-particle entanglement in static[27,37,38] and dynamic[39,40] systems as well as for quantum state transfer.[41]

It is interesting to note that the edge state description also hold for conductors at even higher magnetic fields, in the fractional Quantum Hall regime. As examples, the fractional charge has been determined in shot-noise experiments[42,43] and the quantum statistical properties of the fractionally charged quasi-particles have been investigated theoretically in beam-splitter[44] and HBT[45] geometries. Various interferometer structures have also been considered.[46,47,48] Very recently, a MZ-interferometer in the fractional Quantum Hall regime was proposed.[49] In this work we however consider only the integer Quantum Hall effect, where the quasi-particles are noninteracting and the electrical analogs to optical experiments can be directly realized.

B. Scattering approach to current and noise

This discussion leads us to consider single mode, multi-terminal conductors with noninteracting electrons. The principle aim of this work is a comparison of the MZ and HBT-interferometers. In reality in both interferometers interactions (screening) play a role both for the voltage and temperature dependence. A non-interacting scattering approach is not gauge invariant but requires a treatment of screening.[50] However, these effects are expected to be similar in the two interferometers and will not affect the main conclusions of this work. Therefore, below we treat non-interacting qausi-particle interferometers. The conductors are connected to several electronic reservoirs, biased at a voltage eV or grounded. The current[51] and the noise[1,52] are calculated within the scattering approach for multi-terminal conductors. We first introduce the creation and annihilation operators for in-going, $\hat{a}_\alpha^\dagger(E)$ and $\hat{a}_\alpha(E)$, and outgoing, $\hat{b}_\alpha^\dagger(E)$ and $\hat{b}_\alpha(E)$, particles, at energy E in terminal α. For simplicity we suppress spin notation. Considering a conductor with N terminals, the in- and out-going annihilation operators are related via the $N \times N$ scattering matrix, as

$$\hat{b}_\alpha(E) = \sum_{\beta=1}^N s_{\alpha\beta}(E)\hat{a}_\beta(E) \quad (1)$$

where $s_{\alpha\beta}(E)$ is the amplitude to scatter from terminal β to terminal α. The current operator in the lead α has the form[51]

$$\hat{I}_\alpha(t) = \frac{e}{h}\sum_{\beta\gamma}\int dE\,dE'\exp(i[E-E']t/\hbar) \\ \times A_{\beta\gamma}^\alpha(E,E')\hat{a}_\beta^\dagger(E)\hat{a}_\gamma(E'), \quad (2)$$

with the notation

$$A_{\beta\gamma}^\alpha(E,E') = \delta_{\alpha\beta}\delta_{\alpha\gamma} - s_{\alpha\beta}^*(E)s_{\alpha\gamma}(E'). \quad (3)$$

The average current is given by[51]

$$\langle I_\alpha \rangle = \int dE\,j_\alpha(E), \quad (4)$$

where the spectral current density is

$$j_\alpha(E) = \frac{1}{e}\sum_\beta G_{\alpha\beta}(E)f_\beta(E). \quad (5)$$

Here $f_\beta(E) = 1/(1 + \exp[(E-eV_\beta)/k_BT])$ is the Fermi Dirac distribution of terminal β, with V_β the corresponding applied voltage. The spectral conductance $G_{\alpha\beta}(E)$ is given by

$$G_{\alpha\beta}(E) = \frac{e^2}{h}A_{\beta\beta}^\alpha(E,E). \quad (6)$$

The zero frequency correlator between current fluctuations in terminals α and β is defined as

$$S_{\alpha\beta} = \int dt\langle\Delta\hat{I}_\alpha(0)\Delta\hat{I}_\beta(t) + \Delta\hat{I}_\beta(t)\Delta\hat{I}_\alpha(0)\rangle, \quad (7)$$

where $\Delta\hat{I}_\alpha(t) = \hat{I}_\alpha(t) - \langle\hat{I}_\alpha(t)\rangle$. The current correlator is given by[1,52]

$$S_{\alpha\beta} = \int dE\,S_{\alpha\beta}(E) \quad (8)$$

where

$$S_{\alpha\beta}(E) = \frac{2e^2}{h}\sum_{\gamma\delta}A_{\gamma\delta}^\alpha(E,E)A_{\delta\gamma}^\beta(E,E) \\ \times f_\gamma(E)[1-f_\delta(E)] \quad (9)$$

is the spectral current correlator.

C. Dephasing voltage probe model

There are several physical mechanisms that might lead to dephasing of the electrons propagating along the edge states (see e.g. the discussion in Ref. [9]). In this work we are not interested in any particular mechanism for dephasing but consider instead a phenomenological model, a dephasing voltage probe. The idea of using a voltage probe to induce dephasing was introduced in Refs. [53,54]. A voltage probe connected to a mesoscopic sample was considered, leading to a suppression of coherent transport due to inelastic scattering. The probe model, originally considered for the average current, was extended to treat the effect of inelastic scattering on shot noise by Büttiker and Beenakker[55] by considering a conservation of current fluctuations at the probe as well. Later De Jong and Beenakker[56] extended the voltage probe concept and introduced a (fictitious) voltage probe which breaks phase but does not dissipate energy. Scattering in the voltage probe is (quasi-)elastic.

This is achieved with the help of a distribution function in the voltage probe which conserves not only total current like a real voltage probe, but conserves current in every small energy interval. Such a probe provides a model of pure dephasing. The different probe models have been used as qualitative models in a number of works, see Refs. [2,57] for a review. For an application to quantum Hall systems, see Ref. [58].

In this work we consider the dephasing voltage probe model, which conserves the current at each energy. The model is based on the assumption that the current is conserved on a time scale τ_C, much shorter than the time of the measurement but much longer than the time between injection of individual electrons, here of the order of $\hbar/eV$. One could however consider a more general voltage probe model that takes into account a more complicated dynamics of the probe. A detailed discussion of such a general model in the light of recent work[14,15,59,60] is however deferred to a later work. Here we only note that below we find that the voltage probe in both the MZ and HBT-interferometers only gives rise to a suppression of the phase dependent terms in conductance and noise, just as one would naively expect to be the effect of pure dephasing.

The condition of zero current into the fictitious probe γ at each energy is fulfilled by considering a time dependent distribution function of the probe

$$f_\gamma(E,t) = \bar{f}_\gamma(E) + \delta f_\gamma(E,t), \qquad (10)$$

where $\delta f_\gamma(E,t)$ fluctuates to conserve current on the timescale τ_C. As a consequence, the spectral current density at each energy in lead α fluctuates in time as

$$j_\alpha(E,t) = j_\alpha(E) + \Delta j_\alpha(E,t), \qquad (11)$$

where the fluctuations $\Delta j_\alpha(E,t) = \delta j_\alpha(E,t) + (1/e)G_{\alpha\gamma}(E)\delta f_\gamma(E,t)$ consist of two parts, the intrinsic fluctuations $\delta j_\alpha(E,t)$ and the additional fluctuations due to $\delta f_\gamma(E,t)$. The requirement of zero average current into the probe, $j_\gamma(E) = 0$, leads to the averaged distribution function at the probe reservoir γ

$$\bar{f}_\gamma(E) = -\sum_{\alpha \neq \gamma} \frac{G_{\gamma\alpha}(E)}{G_{\gamma\gamma}(E)} f_\alpha(E). \qquad (12)$$

The average spectral current density $j_\alpha^{dp}(E)$ is then found from Eq. (5).

The fluctuating part of the distribution function, $\delta f_\gamma(E,t)$, is obtained from the requirement of zero current fluctuations into the probe, $\Delta j_\gamma(E,t) = \delta j_\gamma(E,t) + (1/e)G_{\gamma\gamma}(E)\delta f_\gamma(E,t) = 0$. The total current density fluctuation is then given by

$$\Delta j_\alpha(E,t) = \delta j_\alpha(E,t) - \frac{G_{\alpha\gamma}(E)}{G_{\gamma\gamma}(E)}\delta j_\gamma(E,t). \qquad (13)$$

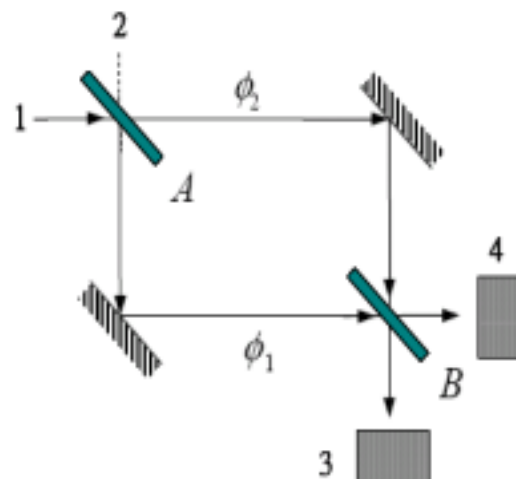As a result, in the presence of dephasing the total spectral

FIG. 1: An optical Mach-Zehnder interferometer. A beam of light incident from 1 is split in two partial beams at the semi-transparent beam splitter A. The two partial beams acquire geometrical phases ϕ_1 and ϕ_2 respectively and are rejoined at the second beam splitter B. The light intensity is measured in detectors 3 and 4

current correlation $S_{\alpha\beta}^{dp}(E)$ is

$$\begin{aligned}
S_{\alpha\beta}^{dp}(E) &= S_{\alpha\beta}(E) - \frac{G_{\alpha\gamma}(E)}{G_{\gamma\gamma}(E)}S_{\beta\gamma}(E) - \frac{G_{\beta\gamma}(E)}{G_{\gamma\gamma}(E)}S_{\alpha\gamma}(E) \\
&\quad + \frac{G_{\alpha\gamma}(E)G_{\beta\gamma}(E)}{G_{\gamma\gamma}^2(E)}S_{\gamma\gamma}(E),
\end{aligned} \qquad (14)$$

where $S_{\alpha\beta}(E)$ is the correlation function between the intrinsic current fluctuations, δj_α and δj_β, of contact α and β, given by Eq. (9), and $G_{\alpha\beta}(E)$ is the conductance, given by Eq. (6).

III. MACH-ZEHNDER INTERFEROMETERS

A schematic of the MZ-interferometer is shown in Fig. 1. An incident beam of light from source 1 is divided in two parts at the semitransparent beam splitter A. The two partial beams are reflected at mirrors and later joined at the second beam splitter B. Beams of light going out from B are detected in 3 and 4. The amplitude of the light in an outgoing beam is the sum of the amplitudes for the two partial beams, $A = A_1\exp(i\phi_1) + A_2\exp(i\phi_2)$. This gives an intensity $|A|^2 = |A_1|^2 + |A_2|^2 + 2\mathrm{Re}\{A_1 A_2^*\exp(i[\phi_1 - \phi_2])\}$. The interference term $2\mathrm{Re}\{A_1 A_2^*\exp(i[\phi_1 - \phi_2])\}$ thus contains the difference between the geometrical phases, $\phi_1 - \phi_2$. Importantly, the four terminal geometry together with the reflectionless beam splitters lead to that the incident beam traverses the interferometer only once. This is a defining property of the MZ-interferometer.
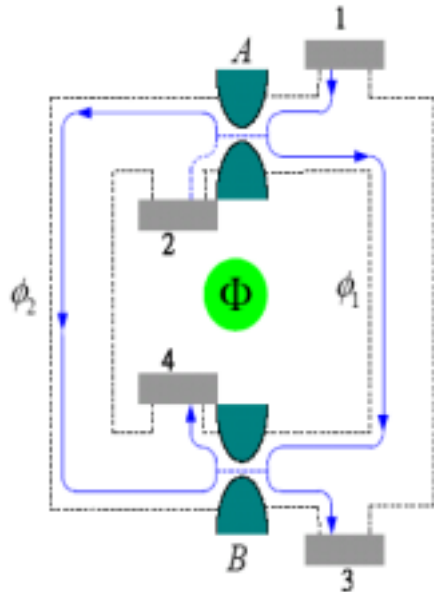
FIG. 2: The electronic analog of the MZ-interferometer, implemented by Ji et al.[9] in a conductor in the Quantum Hall regime. The electronic reservoir 1 is biased at eV and reservoirs 2 to 4 are kept at ground. The edge states (solid lines) have a direction of transport indicated by arrows. The QPC's A and B play the role of the beam splitters in Fig. 1. Geometrical phases ϕ_1 and ϕ_2 and the AB-flux Φ are shown.

We then turn to the electric analog of the MZ-interferometer, shown in Fig. 2. As pointed out above, several results for the current and noise are available in the literature.[10,11,14,15,16,17] Here we analyze the most general situation possible, with finite voltage, temperature and interferometer arm asymmetry as well as different beam splitters A and B with arbitrary transparency. When we consider limiting cases for e.g. small temperature, bias or asymmetry, known results are recovered. This detailed analysis of the MZ-interferometer is of importance when comparing to the HBT-interferometer below.

We first discuss a fully coherent interferometer, the effect of dephasing is investigated below. An electric potential eV is applied at terminal 1, all other terminals are kept at zero potential. The injected electrons propagate along single edge states. Scattering between the edge states can take place only at the two QPC's, acting as beam splitters with controllable transparency. The beam splitters $j = A, B$ are characterized by the scattering matrices

$$\begin{pmatrix} i\sqrt{R_j} & \sqrt{T_j} \\ \sqrt{T_j} & i\sqrt{R_j} \end{pmatrix}, \qquad (15)$$

where T_j and $R_j = 1 - T_j$ are the transmission and reflection probabilities, respectively. We note that any additional phases of the beam splitters just give rise to a

constant phase shift of the oscillations in the interference terms and are therefore not considered.

Propagating along the edge states, the electrons pick up geometrical phases ϕ_1 and ϕ_2 as well as phases ψ_1 and ψ_2 due to the AB-flux Φ through the center of the interferometer. For example, the amplitude for scattering from terminal 1 to 4 is given by

$$s_{41} = i\sqrt{T_B R_A}\, e^{i(\phi_1 + \psi_1)} + i\sqrt{T_A R_B}\, e^{i(\phi_2 - \psi_2)} \qquad (16)$$

For the geometrical phases, to be specific we consider the case when the potential landscape $eU(x, y)$ of the conductor in Fig. 2 is varying smoothly on the scale of the magnetic length $l_B = (\hbar/e|B|)^{1/2}$, with $B\hat{z}$ the applied magnetic field perpendicular to the plane in Fig. 2 (the effect of selfconsistency of the potential[61] is neglected). This allows for a semiclassical treatment.[62] In a high magnetic field the edge states at Fermi energy E_F follow equipotential lines determined by $eU(x, y) = E_F - \hbar\omega_c(n + 1/2)$ where $\omega_c = eB/m$ is the cyclotron frequency and m the effective electron mass. We are concerned here with the case where there is only one edge state and thus $n = 0$. Suppose the x-axis is a line intersecting quantum point contacts A and B in Fig. 2. Excluding self-intersections we can express the edge state in terms of functions $y_1(x)$ and $y_2(x)$ for the left and right path of the interferometer. Working in the symmetric gauge, the geometric phases can be written[62] $\phi_i = -l_B^{-2}\int_{x_A}^{x_B} dx\, y_i(x)$, where x_A and x_B are the locations of the QPC's. Importantly, $\phi_1 - \phi_2$ corresponds to the total area A enclosed by these two paths divided by the magnetic length squared, or $\phi_1 - \phi_2 = 2\pi BA/\Phi_0$ where BA is the total flux through the enclosed area and $\Phi_0 = h/e$ the elementary flux quantum. Note that the Aharonov-Bohm flux Φ adds an additional phase ψ_1 and ψ_2, with $\psi_1 + \psi_2 = 2\pi\Phi/\Phi_0$, to each of the paths.

For the discussion of the temperature and voltage dependence of the current and the noise, we also need to know the energy dependence of the phases. First, instead of parameterizing the edge state through x we introduce the parameter s which measures directly the path length, i.e. $x(s)$, $y(s)$. In addition at s we introduce local coordinates $s_{\parallel}$ along and $s_{\perp}$ perpendicular to the equipotential line. In these coordinates, an edge state that follows the equipotential line at a small energy E away from E_F acquires the additional phase $\Delta\phi = -l_B^{-2}\int ds\Delta s_{\perp}$ with $e(dU/ds_{\perp})\Delta s_{\perp} = E$. The potential gradient $dU/ds_{\perp}$ determines the local electric field $F(s) = -dU/ds_{\perp}$ at s. But $eF(s)l_B = \hbar v_D(s)$ where $v_D(s) = F(s)/B$ is the drift velocity of the guiding center of the cyclotron orbit at point s of the edge state. Thus a small increase in energy leads to a phase increment given by $\Delta\phi_i = \int ds[1/\hbar v_D(s_i)]E$. A rough estimate using a drift velocity which is constant along the edge gives $\Delta\phi_i \approx (L_i/\hbar v_D)E$ with L_i the length of the edge state i. For the phase-difference of the two interfering paths we have

$$\phi_1(E) - \phi_2(E) = \Delta\phi(E_F) + E/E_c \qquad (17)$$

with $\Delta\phi(E_F) = \phi_1(E_F) - \phi_2(E_F)$ the equilibrium phase difference. Formally, higher order terms in energy can be neglected for characteristic energies $k_B T$ and eV much smaller than $(dU/ds_\perp)^2/[d^2U/ds_\perp^2]$. The asymmetry of the two edges thus gives rise to an energy scale $E_c = \{\int ds[1/\hbar v_D(s_1)] - \int ds[1/\hbar v_D(s_2)]\}^{-1}$ which is due to the mismatch of the edge state path lengths, i.e. $E_c \approx \hbar v_D/(\Delta L)$ with $\Delta L = L_1 - L_2$. In principle, for a completely symmetric interferometer one has $E_c \to \infty$.

Given the scattering amplitudes $s_{\alpha\beta}$, the spectral current density is found from Eqs. (3), (5) and (6). For e.g. terminal 4, one gets

$$j_4(E) = (e/h)[f(E) - f_0(E)]\,[T_A R_B + T_B R_A$$
$$+ 2\sqrt{T_A T_B R_A R_B}\cos(E/E_c + \Theta)\Big], \quad (18)$$

where we introduce the total, energy independent phase $\Theta = \Delta\phi(E_F) + 2\pi\Phi/\Phi_0$. Here $f_0(E)$ is the distribution functions of the grounded terminals 2,3 and 4 and $f(E) = f_0(E - eV)$ the distribution function of terminal 1. The current is then given from Eq. (4), as

$$I_4 = \frac{e}{h}\left[(T_A R_B + T_B R_A)\,eV + \sqrt{T_A T_B R_A R_B}\right.$$
$$\times\; 4\pi k_B T \operatorname{csch}\left(\frac{k_B T\pi}{E_c}\right)\sin\left(\frac{eV}{2E_c}\right)\cos\left(\frac{eV}{2E_c} + \Theta\right)\right]. \quad (19)$$

Current conservation gives $I_3 = (e^2/h)V - I_4$. The current consists of two physically distinct parts. The first term in Eq. (19) is the phase independent, incoherent part, the current in the absence of interference, while the second, phase dependent term is the interference contribution. We note that a bias eV of the order of the asymmetry energy E_c leads to the phase shifts of the oscillation. The strength of the interference can conveniently be quantified via the visibility as

$$\nu_I = \frac{I_{max} - I_{min}}{I_{max} + I_{min}} = \frac{\mathrm{amp}[I]}{\langle I \rangle}, \quad (20)$$

which gives for the current in the MZ-interferometer

$$\nu_{I,MZ} = \frac{\sqrt{T_A T_B R_A R_B}}{T_A R_B + T_B R_A}$$
$$\times\; \frac{4\pi k_B T}{eV}\operatorname{csch}\left(\frac{k_B T\pi}{E_c}\right)\left|\sin\left(\frac{eV}{2E_c}\right)\right|. \quad (21)$$

The visibility is a product of a term containing the QPC scattering probabilities and a function depending on the energy scales $k_B T$, eV and E_c. The scattering probability term is maximum for identical QPC's, $T_A = T_B$. The energy scale dependence is shown in Fig. 3 where the visibility for identical point contacts is plotted as a function of the normalized temperature, $k_B T/E_c$. We note several interesting features from Fig. 3 and Eq. (21). (i) the visibility shows decaying oscillations as a function of voltage $\nu_{I,MZ} \propto |\sin(eV/2E_c)|/eV$ for arbitrary temperature. (ii) A symmetric MZ-interferometer, $E_c \gg k_B T$,
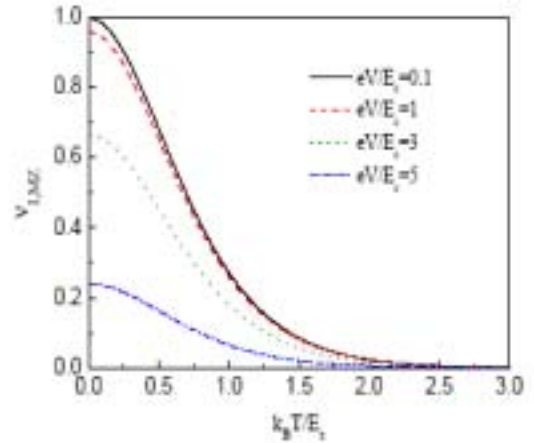

FIG. 3: Current visibility of the Mach-Zehnder interferometer $\nu_{I,MZ}$ versus normalized temperature $k_B T/E_c$ for $T_A = T_B$.

eV, has unity visibility (for $T_A = T_B$), i.e. shows perfect interference. (iii) The visibility decays monotonically with increasing temperature. For large temperatures, $k_B T \gg E_c$, the visibility decays exponentially with the temperature as $\nu_{I,MZ} \propto k_B T \exp(-\pi k_B T/E_c)$.

It is interesting to compare the calculated visibility to the experimentally measured one in Ref. [9]. As already shown in Ref [9], the measured scattering probability dependence of $\nu_{I,MZ}$ is well reproduced by Eq. (21). For the energy scale dependence, no information about the drift velocity v_D or the asymmetry ΔL needed to determine E_c is provided in Ref. [9]. However, to obtain the order of magnitude of E_c, considering as a rough estimate a typical drift velocity[63] $v_D \sim 10^4$ m/s at a magnetic field $B \sim 1T$ and an asymmetry $\Delta L \sim 0.1\mu m$ gives an E_c corresponding to an applied bias $\sim 10\mu V$ or a temperature $\sim 100 mK$. These values are typically of the same order of magnitude as the ones considered in the experiment. As a first approximation, one would thus expect asymmetry effects to be of importance. The observed temperature dependence, a strong decrease of the visibility for increased temperature, is also qualitatively described by Eq. (21) with an $E_c/k_B \sim 50$ mK. This is however not the case with the voltage dependence. Ji et al find a differential visibility, i.e. the visibility of $dI(V)/dV$, which decays strongly with applied voltage, while Eq. (19) predicts a constant, voltage independent differential visibility. There are several possible explanations to why the voltage dependence in contrast to the temperature dependence is not reproduced by the theory. Ji et al themselves point out two voltage dependent dephasing mechanism: low frequency noise of $1/f$ type due to moving impurities, induced by a higher current and fast fluctuations of the potential landscape (and hence of the phase via the enclosed area) caused by screening of the additional charges injected at higher current. Screening might also, for the nonlinear current-voltage characteristics predicted by Eq. (19), lead to a voltage

dependent renormalization of the transmission probabilities, introducing a voltage dependence in the differential visibility.[50,64] We also note that in the model of Ref. [16], inducing dephasing by coupling the MZ-interferometer to a quantum bath, gives a dephasing rate that increases with increasing voltage. Clearly, further investigations are needed to clarify the origin of the dephasing in the experiment in Ref. [9].

Turning to the noise, we focus on the cross correlator between currents flowing in terminals 3 and 4 (the auto-correlator can be obtained analogously). This allows for a straightforward comparison to the result of the HBT-interferometer, for which the cross correlator was investigated in Ref. [27]. From Eqs. (8) and (9) and the expressions for the scattering amplitudes, we arrive at the noise spectral density

$$
S_{34}(E) = \frac{-2e^2}{h}\left[f(E) - f_0(E)\right]^2
$$
$$
\times \left\{ c_0 + c_\Theta \cos\left(\frac{E}{E_c} + \Theta\right) + c_{2\Theta}\cos\left(2\left[\frac{E}{E_c} + \Theta\right]\right) \right\},
$$
(22)

with coefficients

$$
\begin{aligned}
c_0 &= T_A R_A + T_B R_B - 6 T_A R_A T_B R_B, \\
c_\Theta &= 2\left(T_A - R_A\right)\left(T_B - R_B\right)\sqrt{T_A T_B R_A R_B}, \\
c_{2\Theta} &= 2 T_A T_B R_A R_B.
\end{aligned}
$$
(23)

Performing the energy integrals in Eq. (8) we find for the cross correlator

$$
S_{34} = -\frac{2e^2}{h}\left\{ c_0 \bar{S}_0 + c_\Theta \bar{S}_\Theta \cos\left(\frac{eV}{2E_c} + \Theta\right) \right.
$$
$$
\left. + c_{2\Theta}\bar{S}_{2\Theta}\cos\left[2\left(\frac{eV}{2E_c} + \Theta\right)\right] \right\}
$$
(24)

where we introduce the functions

$$
\bar{S}_0 = eV \coth\frac{eV}{2k_B T} - 2k_B T,
$$
(25)

$$
\bar{S}_\Theta = 2\pi k_B T \operatorname{csch}\left(\frac{\pi k_B T}{E_c}\right)\left[\coth\left(\frac{eV}{2k_B T}\right)\right.
$$
$$
\left. \times \sin\left(\frac{eV}{2E_c}\right) - \frac{k_B T}{E_c}\cos\left(\frac{eV}{2E_c}\right)\right].
$$
(26)

and

$$
\bar{S}_{2\Theta} = 2\pi k_B T \operatorname{csch}\left(\frac{2\pi k_B T}{E_c}\right)\left[\coth\left(\frac{eV}{2k_B T}\right)\right.
$$
$$
\left. \times \sin\left(\frac{eV}{E_c}\right) - \frac{2k_B T}{E_c}\cos\left(\frac{eV}{E_c}\right)\right].
$$
(27)

containing the dependence on the energy scales eV, $k_B T$ and E_c.

Just as the current in Eq. (19), the noise consists of a phase independent, incoherent part and a phase dependent, interference part. However, in contrast to the

current, the phase dependent part of the noise contains two terms with different periods in Θ, corresponding to oscillations periodic in h/e and $h/2e$. These terms result from two-particle scattering processes which enclose the AB-flux one and two times respectively. Similarly to the current, the phase of the oscillations are shifted for a bias eV of the order of the asymmetry energy E_c.

It is important to note that in the MZ (in contrast to the HBT) interferometer, two particle and higher order scattering processes are just products of single particle scattering processes. The full distribution of current fluctuations[17] is thus a function of single particle scattering probabilities only. In particular, the noise spectral density $S_{34}(E)$ in Eq. (22) is proportional to $-|s_{41}|^2|s_{31}|^2$, i.e. partition noise[1] with phase dependent scattering probabilities. As a consequence, the phase independent, incoherent part of the noise can not be understood as partition noise from incoherent single particle processes, i.e. $\langle|s_{41}|^2\rangle_{inc}\langle|s_{31}|^2\rangle_{inc} \neq \langle|s_{41}|^2|s_{31}|^2\rangle_{inc}$. This is formally clear since the term proportional to $\cos^2\Theta = [1 + \cos(2\Theta)]/2$, from two coherent scattering processes, obviously contribute to the phase independent part of the noise. As a consequence, as shown by Marquardt and Bruder,[14,15] a model[2] with a filled stream of classical particles injected from reservoir 1 correctly reproduces the incoherent part of the current but fails to reproduce the incoherent part of the noise. In contrast, as found in Ref. [15] and further discussed below, the completely dephasing voltage probe model correctly reproduces the incoherent part of both the current and the noise.

To quantify the strength of the oscillations we introduce two separate quantities, $\nu_{N,MZ}^\Theta$ and $\nu_{N,MZ}^{2\Theta}$, here simply called visibilities, which in close analogy to the current visibility in Eq. (21) are defined as the ratio of the amplitudes of the noise oscillations and the average noise. They become

$$
\nu_{N,MZ}^\Theta = \frac{|c_\Theta \bar{S}_\Theta|}{c_0 \bar{S}_0}
$$
(28)

and

$$
\nu_{N,MZ}^{2\Theta} = \frac{|c_{2\Theta}\bar{S}_{2\Theta}|}{c_0 \bar{S}_0}.
$$
(29)

Similarly to the current, both visibilities are products of a term containing the scattering probabilities and a function of the energy scales eV, $k_B T$ and E_c. We first focus on the scattering probability dependent term by considering the visibility in the limit of a symmetric interferometer, $E_c \gg eV, k_B T$, where the energy-scale dependent terms are unity. This gives

$$
\nu_{N,MZ}^\Theta = \frac{2|(T_A - R_A)(T_B - R_B)|\sqrt{T_A T_B R_A R_B}}{T_A R_A + T_B R_B - 6 T_A R_A T_B R_B}
$$
(30)

and

$$
\nu_{N,MZ}^{2\Theta} = \frac{2 T_A T_B R_A R_B}{T_A R_A + T_B R_B - 6 T_A R_A T_B R_B}.
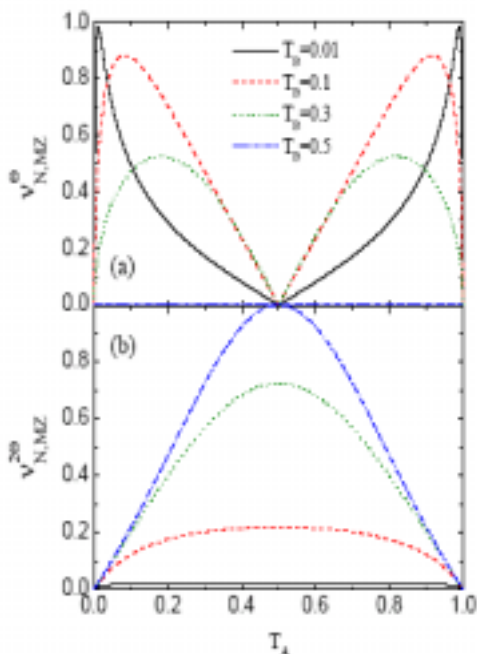$$
(31)

FIG. 4: Noise visibility $\nu_{N,MZ}^{\Theta}$ [figure (a)] of the h/e and $\nu_{N,MZ}^{2\Theta}$ [figure (b)] of the $h/2e$ oscillations in the shot noise of the Mach-Zehnder interferometer versus transmission T_A of beam splitter A for $E_c \gg k_B T, eV$ for various transmission probabilities T_B of beam splitter B.

The two visibilities are plotted in Fig. 4. Both visibilities are symmetric under the substitutions $T_A \leftrightarrow R_A$ and $T_B \leftrightarrow R_B$. The visibility $\nu_{N,MZ}^{\Theta}$ is zero for $T_A = R_A = 1/2$, i.e. for a symmetric setting of any of the QPC's. The visibility increases for increasing QPC asymmetry, reaching a maximum for $0 < T_A < 0.5$ and $0 < T_B < 0.5$ (unity only in the limit $T_A, T_B \ll 1$) and then decreases again toward zero at $T_A = 0$ or $T_B = 0$. Interestingly, the visibility $\nu_{N,MZ}^{2\Theta}$ shows an opposite behavior. It is maximum, equal to unity, at $T_A = T_B = 1/2$ and then decreases monotonically for increasing QPC asymmetry, reaching zero at $T_A = 0$ or $T_B = 0$. This different dependence on the scattering probabilities makes it possible to investigate the two oscillations independently by modulating the QPC transparencies.

Turning to the energy scale behavior, we consider for simplicity $\nu_{N,MZ}^{\Theta}$ in the limit $T_A, T_B \ll 1$ and $\nu_{N,MZ}^{2\Theta}$ in the limit $T_A = T_B = 1/2$ where respective scattering probability terms are unity. For a symmetric interferometer, i. e. $E_c \gg eV, k_B T$, both visibilities are unity. Considering the situation when the temperature is comparable to the asymmetry energy scale E_c but the voltage is small $eV \ll k_B T, E_c$, we get the visibilities

$$\nu_{N,MZ}^{\Theta} = \frac{\pi k_B T}{E_c} \mathrm{csch} \left(\frac{\pi k_B T}{E_c} \right) \left[1 + \left(\frac{k_B T}{Ec} \right)^2 \right] \quad (32)$$

FIG. 5: Noise visibilities $\nu_{N,MZ}^{\Theta}$ (for $T_A, T_B \ll 1$) of the h/e and $\nu_{N,MZ}^{2\Theta}$ of the $h/2e$ oscillations in the shot noise correlation of a Mach-Zehnder interferometer for $T_A = T_B = 1/2$ versus $k_B T/E_c$ for $eV \ll k_B T, E_c$ (red curve) and versus eV/E_c for $k_B T \ll E_c, eV$ (blue curve).

and

$$\nu_{N,MZ}^{2\Theta} = \frac{2\pi k_B T}{E_c} \mathrm{csch} \left(\frac{2\pi k_B T}{E_c} \right) \left[1 + 4 \left(\frac{k_B T}{Ec} \right)^2 \right]. \quad (33)$$
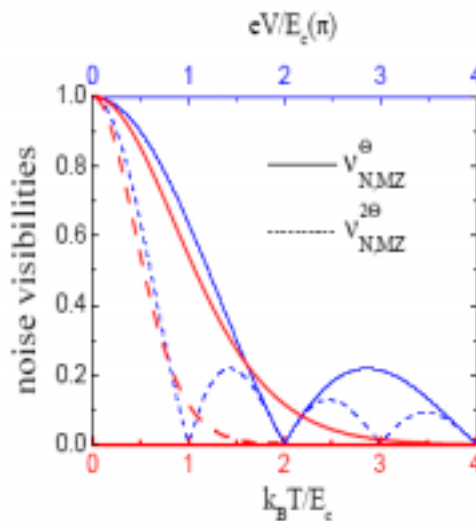
The temperature dependence of the visibilities are shown in Fig. 5. Both visibilities decrease monotonically with increasing temperature. For large temperature $k_B T \gg E_c$, the visibilities decay exponentially as $\nu_{N,MZ}^{\Theta} \propto (k_B T)^3 \exp(-\pi k_B T/E_c)$ and $\nu_{N,MZ}^{2\Theta} \propto (k_B T)^3 \exp(-2\pi k_B T/E_c)$. The visibility $\nu_{N,MZ}^{2\Theta}$ is thus considerably more sensitivity to thermal smearing than $\nu_{N,MZ}^{\Theta}$. In the opposite limit, for a small temperature but a voltage comparable to E_c, i.e. $k_B T \ll E_c, eV$, we instead get the visibilities

$$\nu_{N,MZ}^{\Theta} = \frac{2E_c}{eV} \left| \sin \left(\frac{eV}{2E_c} \right) \right| \quad (34)$$

and

$$\nu_{N,MZ}^{2\Theta} = \frac{E_c}{eV} \left| \sin \left(\frac{eV}{E_c} \right) \right| \quad (35)$$

The visibilities as a function of voltage are plotted in Fig. 5. Both visibilities show an oscillating behavior, decaying as a power law $\propto 1/eV$ with increasing voltage. The period of oscillations, in eV, is $2\pi E_c$ for $\nu_{N,MZ}^{\Theta}$ but πE_c for $\nu_{N,MZ}^{2\Theta}$, half the value for $\nu_{N,MZ}^{\Theta}$. The different voltage dependence gives an additional possibility to investigate the two visibilities independently.

In the experiment of Ji et al.[9] the noise was measured in the high voltage regime, with the interference terms in both the current and noise completely suppressed. The dependence of the incoherent noise on the transparencies T_A and T_B was investigated (T_A was kept at $1/2$ and T_B was varied). A good agreement was found with the first, incoherent term in Eq. (24). Taken the open questions on the effect of decoherence on the average current, a detailed experimental investigation on the phase dependent, interference part of the noise would be of great interest.

A. Effect of dephasing

Next we consider the effect of dephasing on the current and noise. As discussed above, dephasing is introduced by connecting one of the two arms of the interferometer to a fictitious, dephasing voltage probe. The interferometer with the probe, denoted terminal 5, is shown in Fig. 6. The dephasing probe is connected to the edge via a contact described by a scattering matrix

$$\begin{pmatrix} \sqrt{1-\varepsilon} & i\sqrt{\varepsilon} \\ i\sqrt{\varepsilon} & \sqrt{1-\varepsilon} \end{pmatrix}, \qquad (36)$$

where the dephasing parameter ε varies between 0 (no dephasing, fully coherent transport) and 1 (complete dephasing, fully incoherent transport). The presence of the dephasing probe modifies the amplitudes for scattering between the terminal 1, 2, 3 and 4. As an example, the scattering amplitude s_{41}, given in Eq. (16) in the absence of dephasing, now becomes

$$\begin{aligned} s_{41}(\varepsilon) = {} & i\sqrt{T_B R_A}\, e^{i(\phi_1+\psi_1)} \\ & + i\sqrt{1-\varepsilon}\sqrt{T_A R_B}\, e^{i(\phi_2-\psi_2)}. \end{aligned} \qquad (37)$$

In addition, amplitudes for scattering into and out from the probe terminal 5 have to be considered. The current is obtained from Eqs. (4), (5) and (12). For the current in terminal 4, we find

$$\begin{aligned} I_4^{dp} = {} & \frac{e}{h}\Big[(T_A R_B + T_B R_A)\, eV + \\ & \times \sqrt{1-\varepsilon}\sqrt{T_A T_B R_A R_B}\, 4\pi k_B T \operatorname{csch}\left(\frac{k_B T \pi}{E_c}\right) \\ & \times \sin\left(\frac{eV}{2E_c}\right)\cos\left(\frac{eV}{2E_c}+\Theta\right)\Big]. \end{aligned} \qquad (38)$$

Comparison with the result in the absence of dephasing in Eq. (19) shows that the effect of the dephasing is to suppress the phase-dependent oscillations by multiplying the phase-dependent interference term with a factor $\sqrt{1-\varepsilon}$. For complete dephasing $\varepsilon = 1$, the phase dependent term is completely suppressed. The effect of dephasing can thus be simply incorporated in the visibility as

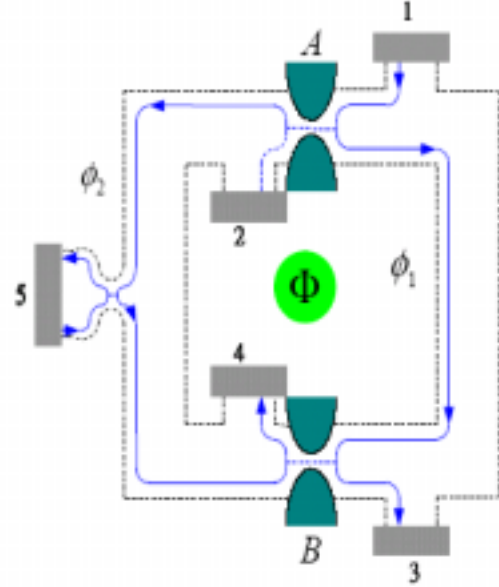$$\nu_{I,MZ}^{dp} = \sqrt{1-\varepsilon}\,\nu_{I,MZ}, \qquad (39)$$

FIG. 6: The electrical MZ-interferometer, Fig. 2, with a dephasing voltage probe, 5, attached along one edge.

where $\nu_{I,MZ}$ is the visibility of the current oscillations in the absence of dephasing, given by Eq. (21). As is clear from the discussion above, to account for the experimental observations in Ref. [9], one would have to consider a voltage dependent dephasing parameter ε.

Turning to the noise, we obtain the cross correlator between currents in lead 3 and 4 in the presence of dephasing from Eqs. (8) and (14), giving

$$\begin{aligned} S_{34}^{dp} = {} & -\frac{2e^2}{h}\bigg\{ c_0 \bar{S}_0 + c_\Theta \bar{S}_\Theta \sqrt{1-\varepsilon}\cos\left(\frac{eV}{2E_c}+\Theta\right) \\ & + c_{2\Theta}\bar{S}_{2\Theta}(1-\varepsilon)\cos\left[2\left(\frac{eV}{2E_c}+\Theta\right)\right]\bigg\}. \end{aligned} \qquad (40)$$

Here the terms c_0, c_Θ, $c_{2\Theta}$, $\bar{S}_0$, $\bar{S}_\Theta$ and $\bar{S}_{2\Theta}$ are defined above in Eqs. (23) and (25) to (27). Similarly to the current, the effect of the dephasing is only to suppress the amplitude of the phase-dependent oscillations. That is what one would naively expect to be the consequence of pure dephasing. The two phase-dependent terms are however affected differently, the $\cos\Theta$ term is suppressed by a factor $\sqrt{1-\varepsilon}$ while the $\cos 2\Theta$ term is suppressed by $(1-\varepsilon)$. The $\cos 2\Theta$ oscillations are thus more strongly suppressed. The visibilities of the two oscillations in the presence of dephasing can simply be written

$$\nu_{N,MZ}^{\Theta,dp} = \sqrt{1-\varepsilon}\,\nu_{N,MZ}^{\Theta} \qquad (41)$$

and

$$\nu_{N,MZ}^{2\Theta,dp} = (1-\varepsilon)\nu_{N,MZ}^{2\Theta}, \qquad (42)$$

where $\nu_{N,MZ}^{\Theta}$ and $\nu_{N,MZ}^{2\Theta}$ are the visibilities for the noise oscillations in the absence of dephasing, given by Eqs. (28) and (29), respectively.

Importantly, both oscillating terms are fully suppressed for complete dephasing, $\varepsilon = 1$. Complete dephasing within the voltage probe model thus gives a noise expression that only consists of the phase independent, incoherent term in Eq. (22). We note already here that the same result is found below for the HBT-interferometer. Since quantum interference by definition is excluded from the model, i.e. all scattering phases are neglected, the completely dephasing voltage probe thus constitutes a classical model that correctly reproduces the incoherent part of the noise. As pointed out above, a more detailed discussion of the physics of the voltage probe and a comparison with Refs. [14,15,59] is deferred to a later work.

It is interesting to note that the effect of dephasing introduced with the voltage probe, both for the current and noise, is for arbitrary dephasing strength identical to a phase averaging. The result in Eqs. (41) and (42) can be obtained by averaging the fully coherent expressions in Eqs. (28) and (29) with respect to a Lorentzian distribution $\rho(\Theta)$ of slow fluctuations of the phase Θ around the average value Θ_0, as

$$\int d\Theta \rho(\Theta) \cos(n\Theta) = (1-\varepsilon)^{n/2} \cos(n\Theta_0). \quad (43)$$

with the Lorentzian distribution

$$\rho(\Theta) = \frac{a/\pi}{(\Theta - \Theta_0)^2 + a^2}, \quad a = -(1/2)\ln(1-\varepsilon) \quad (44)$$

We note that, as pointed out in Ref. [15], a Gaussian distribution of the phase fluctuations gives a different result, not consistent with the dephasing voltage probe approach for arbitrary dephasing stregth.

We emphasize that the results above are independent on to which edge the probe is connected. Moreover, we also point out that the effect of the voltage probes, for arbitrary ε, is multiplicative, i.e. attaching n voltage probes at arbitrary places along the arms can be described by renormalizing $1 - \varepsilon \rightarrow (1-\varepsilon)^n$. Writing $(1-\varepsilon)^n = \exp(n\ln[1-\varepsilon]) = \exp(-L/L_\phi)$, with $L_\phi = -d/\ln[1-\epsilon]$ and $L = nd$ with d the distance between two probes, we can quite naturally incorporate the effect of a uniform distribution of probes into a dephasing length L_ϕ. The suppression of the visibilities of the h/e and $h/2e$ oscialltions due to dephasing in Eqs. (41) and (42) are then modified as $(1-\varepsilon)^{1/2} \rightarrow \exp(-L/2L_\phi)$ and $(1-\varepsilon) \rightarrow \exp(-L/L_\phi)$

IV. HANBURY BROWN TWISS INTERFEROMETERS

The HBT-interferometer is less well known than the MZ-interferometer and deserves some additional comments.[65] The HBT-interferometer was invented as a tool to measure the angular diameter of stars. The first measurement[18] was carried out on a radio star in 1954. Compared to existing schemes based on Michelson interferometers, the HBT-interferometer proved to be less sensitive to atmospheric scintillations, which allowed for a more accurate determination of the angular diameter. After having demonstrated a table-top version of the interferometer in the visual range,[19] the angular diameter of the visual star Sirius was determined.[20]

The experimental results, both the two-particle interference and the positive intensity cross correlations, were successfully explained within a semi-classical framework. Soon after the experiments, it was however shown by Purcell[66] that the positive cross correlations could be explained in terms of bunching of individual photons, emerging from the star, a thermal source of light. This bunching was also demonstrated explicitly in subsequent photo counting experiments.[67,68] The HBT experiment thus laid the foundations for quantum statistical methods in quantum optics.[69] The HBT approach has also been of importance in experimental particle physics.[70] It is interesting to note that positive intensity cross correlations between beams of light emerging from a thermal source, according to some contemporary[71,72] *"would call for a major revision of some fundamental concepts in quantum mechanics"*. Purcell,[66] however, providing an elegant explanation of the bunching phenomena, pointed out that *"the Hanbury Brown Twiss effect, far from requiring a revision of quantum mechanics, is an instructive illustration of its elementary principles"*.

An optical table-top version[73,74] of the HBT-interferometer is shown in Fig. 7. A beam of light is emitted from each one of the sources 2 and 3, completely uncorrelated with each other. The beams are split in two partial beams at the semitransparent beam splitters C and D respectively. The partial beams acquire phases ϕ_1 to ϕ_4 before scattering at the second pair of beam splitters A and B. The resulting beams are collected in detectors at ports 5 to 8.

Importantly, there is no interference pattern in the intensities at the detectors 5 to 8, instead the interference occurs only in the cross correlations between intensities at $5, 6$ and $7, 8$. The intensity cross correlations are sensitive to the two-particle amplitudes: the interference is thus between two different two-particle scattering events, e.g. (i) one particle from 2 scatters to 5 and one particle from 3 scatters to 8, with an amplitude $A_1 \exp(i[\phi_1 + \phi_2])$ and (ii) one particle from 2 scatters to 8 and one particle from 3 scatters to 5, with an amplitude $A_2 \exp(i[\phi_3 + \phi_4])$. The amplitude to detect one particle in 5 and one in 8 is then the sum of the two two-particle amplitudes. This is the case since both scattering processes have the same initial and final states and can not be distinguished. The (reducible) cross correlation between intensities in 5 and 8 is directly related to the corresponding two-particle probability $|A_1 \exp(i[\phi_1 + \phi_2]) + A_2 \exp(i[\phi_3 + \phi_4])|^2 = |A_1|^2 + |A_2|^2 + 2\mathrm{Re}\{A_1 A_2^* \exp(i[\phi_1 + \phi_2 - \phi_3 - \phi_4])\}$. The interference term $2\mathrm{Re}\{A_1 A_2^* \exp(i[\phi_1 + \phi_2 - \phi_3 - \phi_4])\}$ contains the four geometrical phases ϕ_1 to ϕ_4. The HBT-interferometer is thus, in contrast to the MZ-interferometer, a two-particle interferometer.
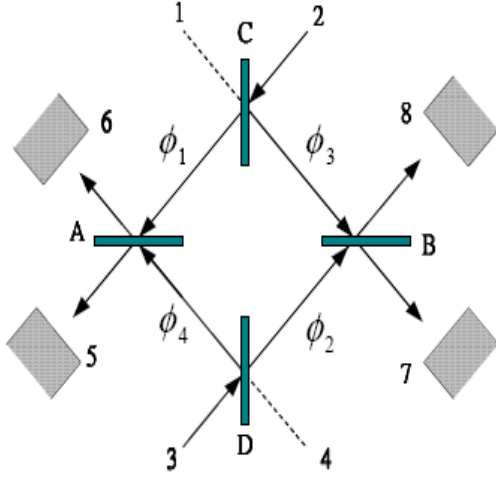
FIG. 7: Two-source, four-detector optical Hanbury Brown Twiss geometry proposed in Ref. [27]. Two beams of light incident from 2 and 3 are split in partial beams at the semitransparent beam splitters C and D. The partial beams acquire geometrical phases ϕ_1 to ϕ_4 and are rejoined in the beam splitters A and B. The light intensity is measured in detectors 5 to 8

The electrical analog of the HBT-interferometer, presented in Ref. [27], is shown in Fig. 8. It consists of a (rectangular) conductor with a hole in the middle, a Corbino geometry. Similar to the MZ-interferometer, the electrons propagate along single edge states. Scattering between the edge states take place only at the beam splitters A to D. The beam splitters are described by scattering matrices given by Eq. (15). We first consider the fully coherent case. In contrast to the MZ-interferometer, the scattering amplitudes contain the phases ϕ_i and ψ_i only via multiplicative phase factors. As an example, the amplitude to scatter from terminal 2 to terminal 5 is given by

$$s_{52} = \sqrt{\mathcal{T}_A \mathcal{T}_C} e^{i(\phi_1 - \psi_1)}. \qquad (45)$$

As a consequence, the average currents which depend only on the modulus squared of the scattering amplitudes [see Eqs. (4) and (6)] do not contain any scattering phases. We get the currents at terminals 5 to 8 as

$$
\begin{aligned}
I_5 &= (e^2/h)V \ (\mathcal{T}_A \mathcal{T}_C + R_A R_D), \\
I_6 &= (e^2/h)V \ (\mathcal{T}_A R_D + R_A \mathcal{T}_C), \\
I_7 &= (e^2/h)V \ (\mathcal{T}_B R_C + R_B \mathcal{T}_D), \\
I_8 &= (e^2/h)V \ (\mathcal{T}_B \mathcal{T}_D + R_B R_C).
\end{aligned}
\qquad (46)
$$

Turning to the current noise, the correlation between currents in terminals 5,6 and 7,8 is given by Eq. (9). We find for the spectral density for the correlators between terminal 5 and 8

$$S_{58}(E) = \frac{-2e^2}{h} [f(E) - f_0(E)]^2 \\ \times \{c_{0,58} + c_\Theta \cos(E/E_c + \Theta)\} \qquad (47)$$
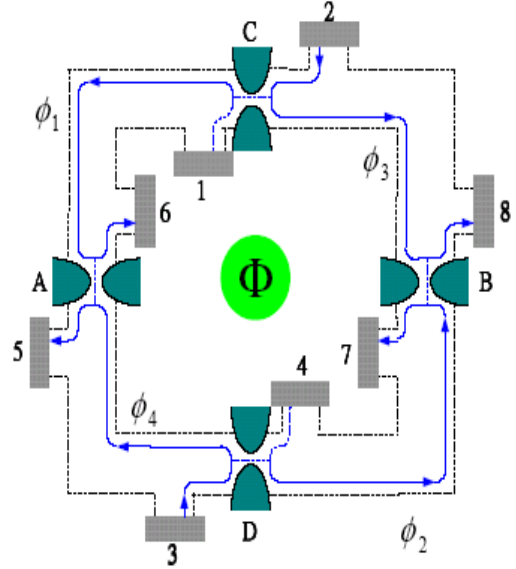

FIG. 8: Two-source, four-detector electrical Hanbury Brown Twiss geometry implemented in a conductor in the Quantum Hall regime. The electronic reservoirs 2 and 3 biased at eV and reservoirs 1 and 4 to 8 are kept at ground. The edge states (solid lines) have a direction of transport indicated by arrows. The QPC's A and B play the role of the beam splitters in Fig. 7. Geometrical phases ϕ_1 to ϕ_4 and the AB-flux Φ are shown.

with the coefficients

$$
\begin{aligned}
c_{0,58} &= \mathcal{T}_A R_B \mathcal{T}_C R_C + \mathcal{T}_B R_A \mathcal{T}_D R_D; \\
\bar{c}_\Theta &= 2 \prod_{j=A,B,C,D} \sqrt{\mathcal{T}_j R_j},
\end{aligned}
\qquad (48)
$$

and for the correlator between terminal 5 and 7

$$S_{57}(E) = \frac{-2e^2}{h} [f(E) - f_0(E)]^2 \\ \times \{c_{0,57} + \bar{c}_\Theta \cos(E/E_c + \Theta)\} \qquad (49)$$

with the coefficient

$$c_{0,57} = \mathcal{T}_A \mathcal{T}_B \mathcal{T}_C R_C + R_A R_B \mathcal{T}_D R_D. \qquad (50)$$

Performing the energy integrals in Eq. (9), we obtain the corresponding current cross correlators

$$S_{58} = \frac{-2e^2}{h} \left[c_{0,58} \bar{S}_0 + \bar{c}_\Theta \bar{S}_\Theta \cos\left(\frac{eV}{2E_c} + \Theta\right) \right] \qquad (51)$$

and

$$S_{57} = \frac{-2e^2}{h} \left[c_{0,57} \bar{S}_0 + \bar{c}_\Theta \bar{S}_\Theta \cos\left(\frac{eV}{2E_c} + \Theta\right) \right]. \qquad (52)$$

Here $\bar{S}_0$ and $\bar{S}_\Theta$ are given by Eqs. (25) and (26). The other two correlators S_{67} and S_{68} are given by the substitutions $S_{67} = S_{58}(\mathcal{T}_C \leftrightarrow \mathcal{T}_D)$ and $S_{68} = S_{57}(\mathcal{T}_C \leftrightarrow \mathcal{T}_D)$. Here, as for the MZ-interferometer we have $\Theta = \Delta\phi(E_F) + 2\pi\Phi/\Phi_0$ with $\Delta\phi = \phi_1 + \phi_2 - \phi_3 - \phi_4$ and $\sum_{i=1}^4 \psi_i = 2\pi\Phi/\Phi_0$.

Several observation can be made from the results above, put in comparison with the result for the noise correlations for the MZ-interferometer in Eq. (24). Just as for the MZ-interferometer, the noise consists of an incoherent, phase independent part, and a coherent, interference part. The phase dependent part of the noise in Eqs. (51) and (52) however contains only one term. The amplitude of the oscillating term is a product of a scattering probability term and an energy-scale dependent function, just as for the MZ-interferometer. This phase dependent term has the same dependence on the phase Θ, the same voltage dependent phase shift as well as the same energy-scale dependence as the second term in Eq. (24). This is the case since they both arise from processes which enclose the AB-flux once. Despite the fact that in the HBT interferometer the AB-effect results from two-particle processes, the periodicity is determined by the single electron flux quantum h/e. The dependence on the scattering probabilities is however different, a consequence of the MZ and HBT interferometer geometries being different. Importantly, there is no term in the noise in Eqs. (51) and (52) that corresponds to the last term in Eq. (24), describing processes which enclose the AB-flux twice. We note that the elementary scattering processes in the HBT-interferometer, in contrast to the MZ-interferometer, are two-particle processes. An important consequence of this is that the incoherent, phase independent noise term in Eqs. (51) and (52) can directly be reproduced by a model with filled streams of classical particles incident from reservoirs 2 and 3.

Since there is only one phase-dependent term, the visibility of the phase-dependent oscillations can again be directly defined, giving for $\alpha = 5, 6$ and $\beta = 7, 8$

$$\nu_{N,HBT}^{\Theta,\alpha\beta} = \frac{\left|\tilde{c}_\Theta \tilde{S}_\Theta\right|}{c_{0,\alpha\beta}\bar{S}_0}. \tag{53}$$

Since the energy-scale dependence of the visibilities is identical to $\nu_{N,MZ}^{\Theta}$ for the MZ-interferometer in Eq. (28), shown in Fig. 5, we focus here only on the scattering probability terms. We thus consider the limit of a symmetric interferometer, $E_c \gg k_B T, eV$ for which the energy-scale dependent part is unity. Several symmetries exists, e.g. all visibilities $\nu_{N,HBT}^{\Theta,\alpha\beta}$ are unchanged by the substitutions $R_C \leftrightarrow T_C$ and $R_D \leftrightarrow T_D$. The visibility $\nu_{N,HBT}^{\Theta,58}$ is unity for scattering probabilities obeying $T_A R_B R_C T_C = T_B R_A R_D T_D$ and similar relations hold for the other visibilities. All visibilities go to zero for any of the transmission probabilities approaching either zero or unity. Focusing on the case with $T_C = T_D$ (or equivalently $T_C = R_D$), the visibilities are given by

$$\nu_{N,HBT}^{\Theta,58} = \nu_{N,HBT}^{\Theta,67} = \frac{2\sqrt{T_A R_A T_B R_B}}{T_A R_B + T_B R_A} \tag{54}$$

and

$$\nu_{N,HBT}^{\Theta,57} = \nu_{N,HBT}^{\Theta,68} = \frac{2\sqrt{T_A R_A T_B R_B}}{T_A T_B + R_A R_B}. \tag{55}$$
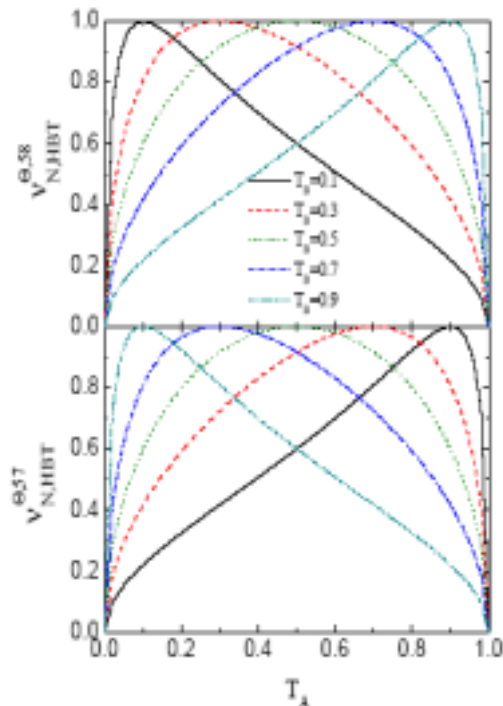

FIG. 9: Noise visibilities $\nu_{N,HBT}^{\Theta,58}$ and $\nu_{N,HBT}^{\Theta,57}$ of shot noise correlations in the HBT geometry versus transmission probability T_A for various values of T_B. A symmetric geometry, $E_c \gg kT, eV$, and identical QPC's C and D are considered.

The two different visibilities are plotted in Fig. 9 as a function of T_A for different T_B. The visibility $\nu_{N,HBT}^{\Theta,58}$ has a maximum equal to unity for $T_A = T_B$, while $\nu_{N,HBT}^{\Theta,57}$ instead has a maximum equal to unity for $T_A = R_B$.

A. The effect of dephasing

Just as in the MZ-interferometer, the dephasing in the HBT-interferometer is introduced by connecting a fictitious voltage probe to an edge between any of the two point contacts. The HBT-interferometer with the probe, denoted 9, is shown in Fig. 10. Here the probe is connected to the edge between contact C and A, we emphasize that the results discussed below do not depend on to which edge-state the probe is connected.

The presence of the probe modifies the amplitudes for scattering from terminals 2, 3 to terminals 5 to 8. As an example, the scattering amplitude in Eq. (45) is modified

$$s_{52} = \sqrt{1-\varepsilon}\sqrt{T_A T_C}e^{i(\phi_1-\psi_1)}. \tag{56}$$

In addition, we also have to consider amplitudes for scattering into and out from the probe terminal 9. The average currents in the presence of dephasing, given from Eqs. (4) to (6) and (12), turn out to be given by the same
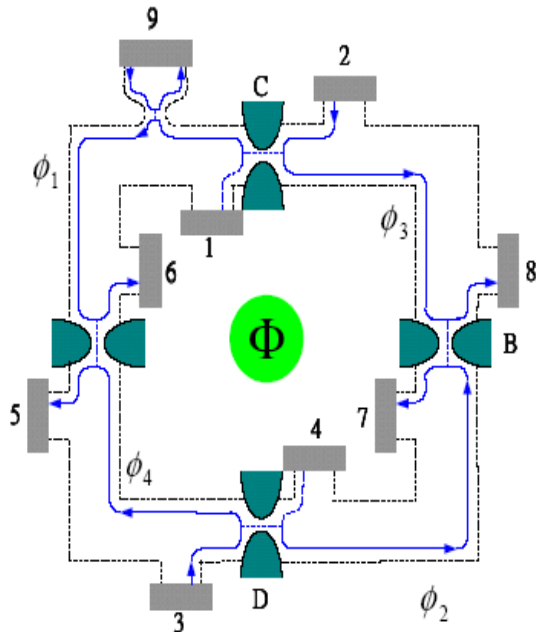
FIG. 10: The electrical HBT-interferometer, Fig. 8, with a dephasing voltage probe, 9, attached along one edge.

equations as in the absence of dephasing, i.e. Eq. (46). This is what one expects, i.e. that dephasing affects only the phase-dependent parts of the observables.

Turning to the current correlators, given from Eqs. (8), (9) and (14), we find for the correlators between terminal 5 and 8

$$S_{58}^{dp} = \frac{-2e^2}{h} \left[c_{0,58} \bar{S}_0 + \bar{c}_\Theta \bar{S}_\Theta \sqrt{1-\varepsilon} \cos\left(\frac{eV}{2E_c} + \Theta\right) \right]$$
(57)

and for the correlators between terminals 5 and 7

$$S_{57}^{dp} = \frac{-2e^2}{h} \left[c_{0,57} \bar{S}_0 + \bar{c}_\Theta \bar{S}_\Theta \sqrt{1-\varepsilon} \cos\left(\frac{eV}{2E_c} + \Theta\right) \right].$$
(58)

The two remaining correlators are again given by the substitutions $S_{67} = S_{58}(\mathcal{T}_C \leftrightarrow \mathcal{T}_D)$ and $S_{68} = S_{57}(\mathcal{T}_C \leftrightarrow \mathcal{T}_D)$. We see from Eq. (57) and (58) that just as for the MZ-interferometer, the only effect of dephasing is to suppress the phase-dependent term. The suppression factor is $\sqrt{1-\varepsilon}$, just the same as for the $\cos\Theta$ term in the noise for the MZ-interferometer in Eq. (24). We can thus directly write the visibilities in the presence of dephasing as

$$\nu_{N,HBT}^{\Theta,\alpha\beta,dp} = \sqrt{1-\varepsilon}\, \nu_{N,HBT}^{\Theta,\alpha\beta}.$$
(59)

This leads to the conclusion that the voltage probe for the HBT-interferometer, just as for the MZ-interferometer, just has the same effect as dephasing due to slow fluctuations of the phase Θ, with the distribution of the phase fluctuations obeying the relation in Eq. (43). Moreover,

the voltage probes have the same multiplicative property as for the MZ-interferometer, allowing one to describe the effect of a continuum of probes along the edges (of total length $L = L_1 + L_2 + L_3 + L_4$) with a dephasing length L_ϕ. The suppression of the visibilities of the h/e oscillations due to dephasing are then modified as $(1-\varepsilon)^{1/2} \rightarrow \exp(-L/2L_\phi)$, just as for the h/e oscillations of the MZ-interferometer.

V. CONCLUSIONS

The MZ-interferometer is an amplitude interferometer: it exhibits a visibility in the average current with period h/e and exhibits a visibility in the shot noise with periods of both h/e and $h/2e$. In contrast, the HBT interferometer is an intensity interferometer, it exhibits no AB-effect in the current and exhibits only an h/e-effect in the shot noise correlations. Interestingly, our investigation shows that the shot noise visibility of the HBT interferometer as a function of temperature, voltage and dephasing rate, is qualitatively similar to that of the h/e-component of the shot noise of the MZ-interferometer. This is contrary to the naive expectation that the visibility of the two particle processes which lead to the HBT effect should be similar to the visibility of the two particle processes in the MZ-interferometer, that is the $h/2e$ component of the shot noise. Instead it is the number of times the AB-flux is enclosed which determines the behavior of the visibility.

In this paper we have investigated and compared in detail the voltage, temperature and asymmetry dependence for the current and noise visibilities in the MZ and HBT-interferometers. The experimental realization of the HBT-interferometer is of large importance since it allows for an unambiguous demonstration of two-particle interference effects with electrons, to date not demonstrated. Moreover, a successful realization of the HBT-interferometer would also enable a first demonstration of orbital entanglement in electrical conductors, a fundamentally important result. The results presented in this work should prove useful for the experimental work aiming to detect the HBT effect in electrical conductors.

VI. ACKNOWLEDGMENTS

[1] M. Büttiker, Phys. Rev. B **46**, 12485 (1992).

[2] Ya. Blanter and M. Büttiker, Phys. Rep. **336** 1(2000).

[3] M. Born and E. Wolf, *Principles of Optics*, 7:th ed. (Cambridge University press, UK, 1999).

[4] L. Mandel, Rev. Mod. Phys. **71**, S274 (1999).

[5] See e.g. S. Pedersen, A.E. Hansen, A. Kristensen, C.B. Sorensen and P.E. Lindelof, Phys. Rev. B **61** 5457 (2000) and references therein.

[6] E. Buks, R. Schuster, M. Heilblum, D. Mahalu and V. Umansky, Nature **391** 871 (1999).

[7] A.E. Hansen, A. Kristensen, S. Pedersen, C.B. Sorensen, and P.E. Lindelof, Phys. Rev. B **64** 045327 (2001).

[8] K. Kobayashi, H. Aikawa, S. Katsumoto and Y. Iye, J. Phys. Soc. Jpn., **71** 2094 (2002).

[9] Y. Ji, Y. Chung, D. Sprinzak, M. Heilblum, D. Mahalu and H. Shtrikman, Nature **422**, 415 (2003).

[10] G. Seelig, M. Büttiker, Phys. Rev. B **64**, 245313 (2001).

[11] G. Seelig, S. Pilgram, A.N. Jordan and M. Büttiker, Phys. Rev. B **68**, R161310 (2003).

[12] K. Le Hur, Phys. Rev. B **65**, 233314 (2002).

[13] K. Le Hur, cond-mat/0503652.

[14] F. Marquardt and C. Bruder, Phys. Rev. Lett. **92**, 56805 (2004).

[15] F. Marquardt and C. Bruder, Phys. Rev. B **70**, 125305 (2004).

[16] F. Marquardt, cond-mat/0410333.

[17] H. Förster, S. Pilgram and M. Büttiker, cond-mat/0502400.

[18] R. Hanbury Brown and R.Q. Twiss, Philos. Mag. Ser. 7 **45**, 663 (1954).

[19] R. Hanbury Brown and R.Q. Twiss, Nature (London) **177**, 27 (1956).

[20] R. Hanbury Brown and R.Q. Twiss, Nature (London) **178**, 1046 (1956).

[21] M. Henny, S. Oberholzer, C. Strunk, T. Heinzel, K. Ensslin, M. Holland and C. Schönenberger, Science **284**, 296 (1999).

[22] W.D. Oliver, J. Kim, R.C. Liu, and Y. Yamamoto, Science **284**, 299 (1999).

[23] H. Kiesel, A. Renz, and F. Hasselbach, Nature (London) **418**, 392 (2002).

[24] M. Büttiker, Physica B **175**, 199 (1991).

[25] M. Büttiker, Phys. Rev. Lett. **68**, 843 (1992).

[26] D. Loss and E.V. Sukhorukov, Phys. Rev. Lett. **84**, 1035 (1992).

[27] P. Samuelsson, E.V. Sukhorukov, and M. Büttiker, Phys. Rev. Lett. **92**, 26805 (2004).

[28] K. v. Klitzing, G. Dorda, M. Pepper, Phys. Rev. Lett. **45**, 494 (1980).

[29] M. Büttiker, Phys. Rev. B **38**, 9375 (1988).

[30] B. I. Halperin, Phys. Rev. B **25**, 2185 (1982).

[31] B. J. van Wees, H. van Houten, C. W. J. Beenakker, J. G. Williamson, L. P. Kouwenhoven, D. van der Marel, and C. T. Foxon, Phys. Rev. Lett. **60**, 848 (1988).

[32] D. A. Wharam, T. J. Thornton, R. Newbury, M. Pepper, H. Ahmed, J. E. F. Frost, D. G. Hasko, D. C. Peacock, D. A. Ritchie and G. A. C. Jones, J. of Phys. C **21**, L861(1988).

[33] R.C. Liu, B. Odom, Y. Yamamoto, and S. Tarucha, Nature **391** 263 (1998).

[34] S. Oberholzer, M. Henny, C. Strunk, C. Schonenberger, T. Heinzel, K. Ensslin, M. Holland, Physica **6E**, 314 (2000).

[35] M. Büttiker, P. Samuelsson, E.V. Sukhorukov, Physica E **20**, 33 (2003).

[36] P. Samuelsson, E.V. Sukhorukov, and M. Büttiker, Phys. Rev. Lett. **91**, 157002 (2003).

[37] C.W.J. Beenakker, C. Emary, M. Kindermann, and J.L. van Velsen, Phys. Rev. Lett. **91**, 147901 (2003).

[38] C.W.J. Beenakker, and M. Kindermann, Phys. Rev. Lett. **92**, 056801 (2004).

[39] P. Samuelsson, and M. Büttiker, cond-mat/0410581 (Phys. Rev. B, in press).

[40] See also related work by C.W.J. Beenakker, M. Titov, B. Trauzettel, Phys. Rev. Lett. **94**, 186804 (2005); A. V. Lebedev, G. B. Lesovik, G. Blatter, cond-mat/0504583.

[41] T. M. Stace, C. H. W. Barnes, and G. J. Milburn Phys. Rev. Lett. **93**, 126804 (2004).

[42] L. Saminadayar, D. C. Glattli, Y. Jin and B. Etienne, Phys. Rev. Lett. **79**, 2526.2529 (1997).

[43] R. de-Picciotto, M. Reznikov, M. Heiblum, V. Umansky, G. Bunin, D. Mahalu, Nature **389** 162 (1997).

[44] I. Safi, P. Devillard, and T. Martin, Phys. Rev. Lett. **86**, 4628 (2001).

[45] S. Vishveshwara, Phys. Rev. Lett. **91**, 196803 (2003).

[46] S.A. Kivelson and V.L. Pokrovsky, Phys. Rev. B **40**, R1373 (1989).

[47] C. de C. Chamon, D.E. Freed, S.A. Kivelson, S.L. Sondhi and X.G. Wen, Phys. Rev. B **55**, 2331 (1997).

[48] M.R. Geller and D. Loss Phys. Rev. B **56**, 9692 (1997).

[49] T. Jonckheere, P. Devillard, A. Crepieux, Th. Martin, cond-mat/0503617.

[50] M. Büttiker, J. Phys. Condensed Matter **5**, 9361 (1993).

[51] M. Büttiker, Phys. Rev. Lett. **57**, 1761 (1986).

[52] M. Büttiker, Phys. Rev. Lett. **65**, 2901 (1990).

[53] M. Büttiker, Phys. Rev. B **33**, 3020 (1986).

[54] M. Büttiker, IBM J. Res. Dev. **32**, 63 (1988).

[55] C.W.J. Beenakker, and M. Büttiker, Phys. Rev. B **46**, 1889 (1992).

[56] M. J. M. de Jong, and C. W. J. Beenakker, Physica A **230**, 219 (1996).

[57] S. A. van Langen, and M. Büttiker, Phys. Rev. B **56**, R1680 (1997).

[58] C. Texier and M. Büttiker, Phys. Rev. B **62**, 7454 (2000). **46**, 1889 (1992).

[59] A.A. Clerk and A.D. Stone, Phys. Rev. B **69**, 245303 (2004).

[60] C.W.J. Beenakker and B. Michaelis, cond-mat/0503347.

[61] D. B. Chklovskii, B. I. Shklovskii and L. I. Glazman, Phys. Rev. B **46**, 4026 (1992); N. R. Cooper and J. T. Chalker, Phys. Rev. B **48**, 4530 (1993).

[62] H. A. Fertig, Phys. Rev. B **38**, 996 (1988).

[63] See e.g. the discussion in N. C. van der Vaart, M. P. de Ruyter van Steveninck, L. P. Kouwenhoven, A. T. Johnson, Y. V. Nazarov, C. J. P. M. Harmans, and C. T. Foxon, Phys. Rev. Lett. **73**, 320 (1994) and references therein.

[64] D. Sanchez and M. Büttiker, Phys. Rev. Lett. **93**, 106802 (2004); T. Christen and M. Büttiker, Phys. Rev. B **53** 2064, (1996).

[65] For an interesting historical account, see R. Hanbury Brown, *The Intensity Interferometer* (London: Taylor and Francis) 1974.

[66] E.M. Purcell, Nature **178**, 1449 (1956).

[67] R.Q. Twiss, A.G. Little, and R. Hanbury Brown, Nature (London) **180**, 324 (1957).

[68] G.A. Rebka, and R.V. Pound, Nature (London) **180**, 1035 (1957).

[69] See e.g. R. Loudon, Rep. Prog. Phys., **43**, 58 (1980).

[70] G. Baym, Acta Phys. Pol. B **29**, 1839 (1998).

[71] E. Brannen and H.I.S. Ferguson, Nature (London) **178**, 481 (1956).

[72] R. Hanbury Brown and R.Q. Twiss, Nature (London) **178**, 1447 (1956).

[73] B. Yurke and D. Stoler, Phys. Rev. Lett. **68**, 1251 (1992).

[74] B. Yurke and D. Stoler, Phys. Rev. A **46**, 2229 (1992).

[Reference]:

[1] *Semiconductor Spintronics and Quantum Computation*, edited by D. D. Awschalom, N. Samarth, and D. Loss (Springer-Verlag, Berlin, 2002).

[2] S. A.Wolf, *et. al.*, Science. **294**, 1488 (2001).

[3] I. Žutić, J. Fabian, and S. Das Sarma, Rev. Mod. Phys. **76**, 323 (2004).

[4] J. Sinova, *et. al.*, Phys. Rev. Lett. **92**, 126603 (2004); S. Murakami, N. Nagaosa and S. Zhang, Science **301**, 1348 (2003); V. M. Edelstein, Solid State Commun., **73**, 233 (1990); A. Voskoboynikov, *et. al.,* Phys. Rev. B. **59,** 12514 (1999); L. S. Levitov and E. I. Rashba, Phys. Rev. B, **67,** 115324 (2003).

[5] S. Datta and B. Das, Appl. Phys. Lett. **56**, 665 (1990); P. Sharma and P. W. Brouwer, Phys. Rev. Lett. **91**, 16 6801 (2003); M. Governale, F. Taddei, and R. Fazio, Phys. Rev. B, **68**, 155324 (2003).

[6] A. G. Malshukov, *et. al.*, Phys. Rev. B, 68, 23 3307 (2003); C. S. Tang, A. G. Malshukov, and K.A. Chao, cond-mat/0412181.

[7] J. Wunderlich, B. Kästner, J. Sinova, and T. Jungwirth, cond-mat/0410295.

[8] Y. K. Kato, *et. al.*, cond-mat/0502627.

[9] G. E. Pikus and A. N. Titkov, in *Optical Orientation*, edited by F. Meier and B. P. Zakharchenya (North- Holland, Amsterdam, 1984).

[10] M. L. Roukes, Phys. World **14**,25 (2001); H. G. Craighead, Science **290**, 1532 (2000); A. N. Cleland, *Foundations of Nanomechanics* (Springer, Berlin, 2003).

[11] P. Mohanty, G, Zolfagharhani, S. Kettemann, P. Fulde, Phys. Rev. B. **70,** 195301 (2004).

[12] R. G. Knobel, A. N. Cleland, Nature **424,** 291 (2003).

[13] M. Buttiker, Phys. Rev. B **46**, 12485 (1992).

[14] Ya. Blanter and M. Buttiker, Phys. Rep. **336**, 1(2000).

[15] M. Born and E. Wolf, Principles of Optics, 7:th ed. (Cambridge University press, UK, 1999).

[16] L. Mandel, Rev. Mod. Phys. **71**, S274 (1999).

[17] See e.g. S. Pedersen, A.E. Hansen, A. Kristensen, C.B. Sorensen and P.E. Lindelof, Phys. Rev. B **61**, 5457 (2000) and references therein.

[18] E. Buks, R. Schuster, M. Heilblum, D. Mahalu and V. Umansky, Nature **391**, 871 (1999).

[19] A.E. Hansen, A. Kristensen, S. Pedersen, C.B. Sorensen, and P.E. Lindelof, Phys. Rev. B **64**, 045327 (2001).

[20] K. Kobayashi, H. Aikawa, S. Katsumoto and Y. Iye, J. Phys. Soc. Jpn. **71**, 2094 (2002).

[21] Y. Ji, Y. Chung, D. Sprinzak, M. Heilblum, D. Mahalu and H. Shtrikman, Nature **422**, 415 (2003).

[22] G. Seelig, M. Buttiker, Phys. Rev. B **64**, 245313 (2001).

[23] G. Seelig, S. Pilgram, A.N. Jordan and M. Buttiker, Phys. Rev. B **68**, R161310 (2003).

[24] K. Le Hur, Phys. Rev. B **65,** 233314 (2002).

[25] K. Le Hur, cond-mat/0503652.

[26] F. Marquardt and C. Bruder, Phys. Rev. Lett. **92**, 56805 (2004).

[27] F. Marquardt and C. Bruder, Phys. Rev. B **70**, 125305 (2004).

[28] F. Marquardt, cond-mat/0410333.

[29] H. Forster, S. Pilgram and M. Buttiker, cond-mat/0502400.

[30] R. Hanbury Brown and R.Q. Twiss, Philos. Mag. Ser. **745**, 663 (1954).

[31] R. Hanbury Brown and R.Q. Twiss, Nature (London) **177**, 27 (1956).

[32] R. Hanbury Brown and R.Q. Twiss, Nature (London) **178**, 1046 (1956).

[33] M. Henny, S. Oberholzer, C. Strunk, T. Heinzel, K. Ensslin, M. Holland and C. Schonenberger, Science **284**, 296 (1999).

[34] M. Henny, S. Oberholzer, C. Strunk, T. Heinzel, K. Ensslin, M. Holland and C. Schonenberger, Science **284**, 296 (1999).

[35] H. Kiesel, A. Renz, and F. Hasselbach, Nature (London) **418**, 392 (2002).

[36] M. Buttiker, Physica B **175**, 199 (1991).

[37] M. Buttiker, Phys. Rev. Lett. **68**, 843 (1992).

[38] D. Loss and E.V. Sukhorukov, Phys. Rev. Lett. **84**, 1035 (1992).

[39] P. Samuelsson, E.V. Sukhorukov, and M. Buttiker, Phys. Rev. Lett. **92**, 26805 (2004).

[40] Y. Kato *et al.*, *ibid.* 299, 1201 (2003); S. Murakami *et al.*, *ibid.* 301, 1348 (2003).

[41] L. Y. Wang, C. S. Tang, and C. S. Chu, cond-mat/0409291.

[42] Alexander Högele, *et al.*, Appl. Phys. Lett. **86**, 221905 (2005)

[43] J. Seufert, *et al.*, Phys. Rev. B **69**, 035311 (2004).

[44] R. Hanson, *et al.*, Phys. Rev. B **70**, 241304 (2004).

[45] Y. A. Bychkov and E. I. Rashba, J. Phys. C 17, 6039 (1984).

[46] Qing-feng Sun, Jian Wang, and Hong Guo, Phys. Rev. B, 71, 16 5310 (2005)

[47] P. Sharma and P. W. Brouwer, Phys. Rev. Lett. **91**, 16 6801 (2003); M. Governale, F. Taddei, and R. Fazio, Phys. Rev. B, **68**, 155324 (2003).

[48] A. G. Malshukov, C. S. Tang, C. S. Chu, and K. A. Chao, Phys. Rev. B, 68, 23 3307 (2003).

[49] S.W. Chung, C.S. Tang, C.S. Chu, and C.Y. Chang, Phys. Rev. B 70, 085315(2004).

[50] C.S. Tang and C.S. Chu, Phys. Rev. B 53, 8 (1996).

[51] Philip F. Bagwell and Roger K. Lake, Phys. Rev. B 46, 23 (1992).

[52] U. Fano, Phys Rev. **124**, 1866 (1961).

[53] U. Fano and A. R. P. Rau, Atomic Collision and Spectra (Academic Press, Orlando, 1986).

[54] J. Faist, F. Capasso, C. Sirtori, K. W. West, and L. N. Pfei_er, Nature **390**, 589 (1997).

[55] F. Cerdeira, T. A, Fjeldly, and M. Cardona, Phys. Rev. B **8**, 4743 (1973).

[56] R. K. Adair, C. K. Bockelman, and R. E. Peterson, Phys. Rev. **76**, 308 (1949).

[57] V. Madhavan, W. Chen, T. Jamneala, M. F. Crommie, and N. S. Wingreen, Science **280**, 567 (1998).

[58] J. Li, W.-D. Schneider, R. Berndt, and B. Delly, Phys. Rev. Lett. **80**, 2893 (1998).

[59] C. Fuhner, U. F. Keyser, R. J. Haug, D. Reuter, and A. D. Wieck, cond-mat/0307590.

[60] J. Gores, D. Goldhaber-Gordon, S. Heemeyer, M. A. Kastner, H. Shtrikman, D. Mahalu, and Y. Meirev, Phys. Rev. B **62**, 2188 (2000).

[61] I. G. Zacharia, D. Goldhaber-Gordon, G. Granger, M. A. Kastner, Y. B. Khavin, H. Shtrikman, D. Mahalu, and U. Meirav, Phys. Rev. B. **64**, 155311 (2001).

[62] K. Kobayashi, H. Aikawa, S. Katsumoto, and Y. Iye, Phys. Rev. Lett. **88**, 256806 (2002).

[63] K. Kobayashi, H. Aikawa, A. Sano, S. Katsumoto, and Y. Iye, Phys. Rev. B **70**, 35319 (2004).

[64] M. Sato, H. Aikawa, K. Kobayashi, S. Katsumoto, and Y. Iye, cond-mat/0410062.

[65] J. Kim, J.-R. Kim, J.-O Lee, J. W. Park, H. M. So, N. Kim, K. Kang, K.-H. Yoo, and J.-J.

Kim, Phys. Rev. Lett **90**, 166403 (2003).

[66] A. A. Clerk, X. Waintal, and P. W. Brouwer, Phys. Rev. Lett. **86**, 4636 (2001).

[67] Y.-J. Xiong and S.-J. Xiong, Int. J. Mod. Phys. B **16**, 1479 (2002).

[68] J. F. Song, Y. Ochiai, and J. P. Bird, Appl. Phys. Lett. **82**, 4561 (2003).

[69] Physics reports (Review Section of Physics Letters) 234, Nos. 2&3 (1993) 73-174.

[70] Weisshaar et al., J. Appl. Phys. 70, 355 (1991).

[71] Weisshaar, Ph.D. dissertation (1991).